

**PHOTOCATALYTIC STUDIES ON SnO₂ AND
CeO₂ DOPED COMPOUNDS**

THESIS

Submitted to the

GOA UNIVERSITY

For the degree of

DOCTOR OF PHILOSOPHY

IN CHEMISTRY

By

Ms PRITAM BORKER

Department of Chemistry

Goa University

December 2004



543

BOR/Pho

T-310

DECLARATION

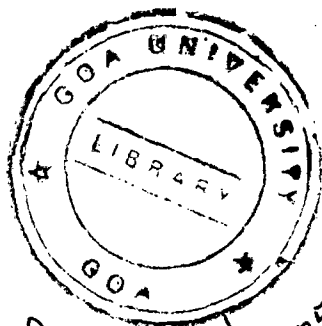
I, Ms. PRITAM BORKER, hereby declare that this thesis entitled "Photocatalytic studies on SnO₂ and CeO₂ doped compounds" for the degree of Doctor of Philosophy in Chemistry is the outcome of my own study undertaken under the guidance of Dr. A.V. Salker, Department of Chemistry, Goa University. It has not previously formed the basis for the award of any degree, diploma or certificate of this or any other University. I have duly acknowledged all the sources used by me in the preparation of this thesis.

P Borker
Pritam Borker

(Candidate)

Date: 30.12.2004

Place: Taleigao - plateau

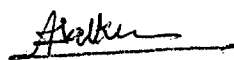


[Signature]
21/10/2005
EXAMINED
BY
(P. SELVAM)

CERTIFICATE

This is to certify that the thesis entitled "**Photocatalytic studies on SnO₂ and CeO₂ doped compounds**" submitted by the candidate Ms. Pritam Borker, for the award of the degree of Doctor of Philosophy in Chemistry is based on the literature survey / laboratory experiments carried out by her during the period of study under my guidance. I further state that the research work presented in the thesis has been carried out independently by her and due acknowledgement has been made whenever outside facilities has been availed of.

Date: 30.12.2004



Dr. A. V. Salker,
Research Guide,
Department of Chemistry,
Goa University.

ACKNOWLEDGEMENT

I express my deep sense of gratitude to Dr. Arun V. Salker for his constant encouragement and insightful guidance during the course of this work.

I am grateful to Dr. K. S. Rane, Head and Dr J. S. Budkuley, ex – head, Department of Chemistry, for extending prompt access to the necessary facilities.

I am highly obliged to Dr. Vidhydatta Verenkar, Department of Chemistry, Goa University for his kind help.

I would like to thank Dr. A. S. Dinge, Principal, PES SRSN College, Goa and his staff members for their constant encouragement.

It is my privilege to place on record my sincere thanks to Dr. P. P. Hankare, Shivaji University, Kolhapur, Dr. Hashmi and Mr. Prabhu, NIO, Dona Paula, Dr. Gundurao, IIT, Mumbai, Dr. Sundaram, ICAR, Old Goa, for providing instrumental facilities.

My sincere thanks to all the faculty members of Department of Chemistry, Goa University for their valuable help and support.

I am thankful to all the non teaching staff of Department of Chemistry and University library.

My special thanks to all the research colleagues past and present who has helped me directly or indirectly during the course of this work.

Finally my profuse thanks to my parents Mr. Prakash and Nilima Borker, my husband Mr. Sameer Patil and all the family members for their encouragement and moral support during the course of this work.

CONTENTS

CHAPTER	Page No.
1. INTRODUCTION	01
2. REVIEW OF LITERATURE	07
2.1 Crystal structure	08
2.1.1 CeO ₂ Fluorite structure	08
2.1.2 SnO ₂ structure	08
2.1.3 Molecular structure of phthalocyanine	09
2.2 Nonstoichiometry	12
2.3 Defect theories	14
2.3.1 Oxygen deficient oxides	14
2.3.2 Anion excess oxides	16
2.4 General properties	17
2.4.1 CeO ₂	17
2.4.2 SnO ₂	21
2.4.3 Phthalocyanines	23
2.5 Electrical properties	28
2.5.1 Theory	28
2.5.2 Mixed conduction in oxides	30
a) Cubic fluorite oxides	30

CONTENTS

b) Cerium Dioxide	31
i) Undoped CeO ₂	31
ii) Doped CeO ₂	32
c) Applications	33
2.5.3 Electrical Properties	34
i) CeO ₂	34
ii) SnO ₂	35
iii) Phthalocyanines	38
2.6 ESR Study	40
2.7 Magnetic Study	41
2.8 UV-Visible spectroscopy	42
2.9 UV-Visible diffuse reflectance spectroscopy	43
2.10 Photocatalytic Studies	44
2.10.1 Conditions for maximum photocatalytic efficiency	50
2.10.2 Semiconductor energetics	51
2.10.3 Ceria as a photocatalyst	52
2.10.4 SnO ₂ as a photocatalyst	54
2.10.5 Photocatalytic activity of phthalocyanines	55
2.10.6 Mechanism	57
i) Singlet Oxygen Photochemistry	61
ii) Fenton reaction	62

CONTENTS

3 EXPERIMENTAL TECHNIQUES	63
3.1A. Preparation of Cerium and Tin oxide doped compounds	63
3.1B. Phthalocyanine preparation	65
3.2 Characterization	66
3.2.1 The X-ray powder diffraction technique	66
3.2.2 Vibrational Spectroscopy (IR)	67
3.2.3 Atomic absorption spectroscopy	67
3.2.4 BET Method (Surface area measurement)	67
3.3 Electrical resistivity measurements	69
3.4 Magnetic Suscetibility Measurements	69
3.5 Saturation Magnetization Study	71
3.6 Thermal Study	72
3.7 Electron Spin Resornance (ESR) Studies	73
3.8 UV-Visible Spectroscopy	74
3.9 UV-Visible diffuse reflectance study	74
3.10 Photocatalytic Studies	75
4 SOLID STATE STUDIES	77
4.1 X-Ray diffraction Analysis	77
4.2 IR Spectroscopy	84
4.3 Thermal Analysis	91
4.4 Electrical Resistivity Measurements	98

CONTENTS

4.5	Magnetic Susceptibility	104
4.6	Saturation Magnetization Study	110
4.7	Electron Spin Resonance Study	110
5	PHOTOCATALYTIC STUDIES	116
5.1	UV-Visible Spectroscopy	116
5.3	Surface Area Measurements	123
5.2	UV-Visible diffuse reflectance Spectroscopy	117
5.4	Photolysis Study of NBB Dye	123
5.4.1	Optimisation of catalyst Loading	128
5.4.2	Effect of Oxygen	131
5.4.3	Effect of pH	131
5.5	Photodegradation of NBB Dye	133
5.5.1	Series I; $Ce_{1-x}Sn_xO_2$	133
5.5.2	Series II; $Ce_{1-x}Fe_xO_2$	136
5.5.3	Series III; $Ce_{1-x}Mn_xO_2$	139
5.5.4	Series IV; $Sn_{1-x}Mn_xO_2$	143
5.5.5	Series V; MPC	143
5.6	Comparative Study of all the compositions	145
5.7	Analysis by HPCL Method	149
5.8	Mechanism	151
5.9	Photocatalytic Study of Auramine O dye	152
5.9.1	Series I; $Ce_{1-x}Sn_xO_2$	155

CONTENTS

5.9.2 Series V ; MPc	155
6 CONCLUSION	159
REFERENCES	165
APPENDIX- I	178

CHAPTER 1

INTRODUCTION

INTRODUCTION

Waste water from various industries are nowadays a serious problem to environment. Most of the industries use dyes and pigments to colour their products. The largest consumers of these dyes are textile, tannery, paper, pulp, pharmaceuticals, cosmetics, food processing units etc. The discharged wastes of these dyes are toxic to microorganisms, aquatic life and human beings. These extensively used commercial dyes are toxic on inhalation and ingestion that may cause liver and thyroid damage and other harmful effects. Besides their toxic effects, they are the major source of coloured effluents and many times non bio- degradable posing threat to the environment¹⁻³. Dyes are insufficiently removed by conventional sewage plant treatment because of their high biochemical stability, relatively high molecular weight and high water solubility due to their excellent all round fastness⁴.

Extensive research is underway to develop advanced analytical, biochemical, and physicochemical methods for the characterization and elimination of hazardous chemical compounds from air, soil, and water. Advanced physicochemical processes such as semiconductor photocatalysis are intended to be both supplementary and complementary to some of the more conventional approaches to the destruction or transformation of hazardous chemical wastes such as high temperature incineration, anaerobic digestion, amended activated sludge digestion, and conventional physico-chemical treatment⁵⁻⁶.

Several work have been done on heterogeneous semiconductor photocatalysis using various semiconductors such as TiO_2 , ZnS , CdS , Fe_2O_3 , ZnO etc. for the degradation of organic and inorganic dye pollutants⁷⁻¹⁵. Photocatalysis have received a special attention in the decomposition of hazardous organic compounds because of their complete mineralization ability and possible application to pollution control using solar energy which is a renewable energy form, cost effective, completely free and which can be used directly to oxidize or degrade the dye chemicals^{4,7}.

Transition metal oxide materials are of interest when designing catalysts since they are less expensive in comparison to the precious group metal (PGM) catalysts such as Platinum and Palladium.

Oxide catalysts are thermally stable, which increases the lifespan of the catalyst. In supported metal catalysts, the metal particles are sometimes detached and transported out, leading to reduced conversion values¹⁶. Insertion of transition metal ions on the photocatalyst structure can significantly enhance the photonic efficiency either by widening the light absorption range or by modifying the redox potential of the photo-produced radicals. Transition metal doping improves trapping of electrons thus inhibiting electron-hole recombination during illumination^{17,18}.

Much effort has been spent in the preparation, characterization and application of ceria and ceria based mixed metal oxide materials for automotive exhaust catalysis, electrochemical cells and oxidation of environmental pollutants. CeO_2 has interesting economical and physicochemical properties. Cerium dioxide is abundant, nontoxic and inexpensive that presents several characteristics that could be potentially advantageous for photocatalytic applications. Ceria is an n-type semiconductor with a band gap of 2.94 eV that absorbs light in the near UV and slightly in the visible region. Its catalytic applications relies primarily on the high efficiency of the reduction / oxidation cycles by shifting between Ce^{4+} under oxidizing

conditions and Ce^{3+} under reducing conditions, respectively. The formation of oxygen vacancies in redox processes occurring on the surface of ceria containing samples is considered to play a crucial role on the oxidative reactions. The capabilities of the redox couple Ce^{4+} - Ce^{3+} are strongly enhanced if other elements are introduced into the CeO_2 lattice by forming solid solutions^{17,19-22}.

SnO_2 has been proved to be good photocatalyst for the degradation of various dyes and organic contaminants²³⁻²⁴. It is also used in gas sensing materials for the detection of various gases because of its good sensitivity²⁵. SnO_2 has wide range of applications in sciences, technologies, and in industries, such as catalysis, conductivity, ceramics, plastics, bio -medicine and as an active component of sensor device²⁶.

Phthalocyanines are particularly attractive as oxidation catalysts because of their relatively cheap and simple preparation in a large scale and their chemical and thermal stability. Besides acting as a photosensitizer and sensor material they can be used as photocatalyst for the degradation of dyes²⁷⁻²⁹.

The mixed oxide photocatalysts containing transition and rare earth element which are discussed in this investigations are prepared by co-precipitation method in order to achieve homogeneity and low

temperature formation with better surface areas, unlike other solid state methods which require high temperature for their formations. Various metal phthalocyanines are prepared by well - known methods as described in literature³⁰⁻³².

In the present investigations the photocatalytic degradation of textile diazo dye Naphthol Blue Black (NBB) and basic yellow Auramine O were studied on the prepared photocatalysts as model reactions. Attempts were made to correlate the photocatalytic activity and solid state properties.

The present investigation includes:

1. Preparation of series of photocatalysts such as
 - a) $Ce_{1-x}Sn_xO_2$
 - b) $Ce_{1-x}Fe_xO_2$
 - c) $Ce_{1-x}Mn_xO_2$
 - d) $Sn_{1-x}Mn_xO_2$ where $x = 0, 0.1, 0.2, 0.3$ and 1.0
 - e) Metal phthalocyanines MPc where $M = Cu, Ni, Co$ and Fe
2. Characterization of oxides and phthalocyanines by different methods such as X-ray powder diffraction (XRD), thermal study (TG/DSC), vibrational spectroscopy (IR) and BET surface area measurements.
3. Solid state properties such as magnetic susceptibility, electrical resistivity, and electron spin resonance (ESR) studies.

4. Photocatalytic degradation of Naphthol Blue Black over prepared photocatalysts.
5. Photocatalytic degradation of basic yellow Auramine O over some selected photocatalysts.
6. It was aimed at finding out which factors predominantly contribute to the observed photoactivity.
7. Proposed the probable reaction mechanism to the photocatalytic degradation of dye.

CHAPTER 2

REVIEW OF LITERATURE

REVIEW OF LITERATURE

For the past three decades, an intensive research on energetically economic methods of solar energy conversion using semiconductor photocatalysts in the form of fine powders, colloids and bulb electrodes is carried out. These methods aim at the solar energy conversion into electrical energy³³.

Transition metal oxides with cations in high formal oxidation state, such as TiO_2 are characterized by a high oxygen/metal (O/M) ratio in the structure. The oxygen sub-lattice has in this case empty interstices¹⁷. The oxides of tetravalent transition elements constitute relevant products for chemical Industry and research in relation to several applications³⁴. CeO_2 is an n-type semiconductor and can be photoactivated by irradiation with light in the UV-vis range¹⁷.

2.1 CRYSTAL STRUCTURE

2.1.1 CeO₂ Fluorite structure

In the oxides of the fluorite and MO₂ each metal atom M is surrounded by eight equivalent nearest neighbor O atoms each of which in turn is surrounded by a tetrahedron of four equivalent M atoms. A typical feature of the fluorite structure is the large ($\frac{1}{2}, \frac{1}{2}, \frac{1}{2}$) octahedral interstitial holes in which interstitial ions can easily be accommodated³⁵.

CeO₂ has cubic fluorite structure^{21,36} and each Ce atom is surrounded by eight equivalent O atoms each of which in turn is surrounded by a tetrahedron of four Ce atoms. Fig.2.1 shows the CeO₂ fluorite structure.

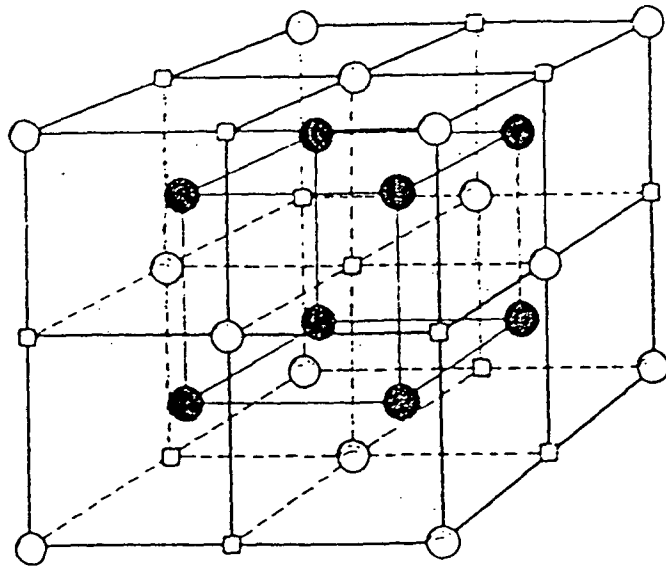
2.1.2 SnO₂ structure

The rutile crystal structure of SnO₂ is formed by a tin atom in the center, surrounded by six oxygen atoms in the vertex. The tin atom is bonded to four oxygen atoms with the same bond length in the basal plane and with another two apical oxygen atoms³⁷⁻⁴⁰. The sub lattice of Sn⁴⁺ ions is body centered tetragonal, the c dimension being much smaller than a dimension, $c/a = 0.644$. The structure can be regarded as consisting

of SnO_6 octahedra sharing edges and corners in such a way that each oxygen ion belongs to three neighbouring octahedra. The oxygen octahedra are slightly distorted. When this structure is observed parallel to the (short) c-axis, open channels become apparent, which allow fast diffusion of small interstitial ion. Fig.2.2 shows SnO_2 rutile structure.

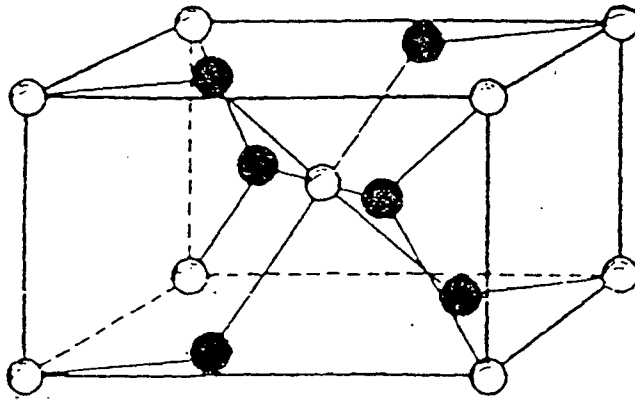
2.1.3 Molecular structure of Phthalocyanine

The single basic structural unit of phthalocyanine molecule is shown in fig.2.3. The molecule is planar consisting of four isoindole molecule linked together at the corners of the pyrrole ring by four nitrogen atoms⁴¹. The space within the four central nitrogen atoms are occupied either by hydrogen atoms in metal free phthalocyanine or by a metal atom in metal substituted phthalocyanines. Distinguishing feature of the phthalocyanines is its conjugate bonding. The most common polymorph of phthalocyanine belongs to the $Pz1/a$ space group with two planar centro-symmetric molecules in a unit cell. The intermolecular binding is weak, but the electrons within a molecule are tightly bound. The electrons associated with the conjugated bonds are not localized on a particular atom, but are associated with the entire molecule. The



○ metal ● oxygen □ interstitial positions

Fig. 2.1. The fluorite (CeO_2) structure.



○ metal ● oxygen

Fig. 2.2 SnO_2 Rutil structure

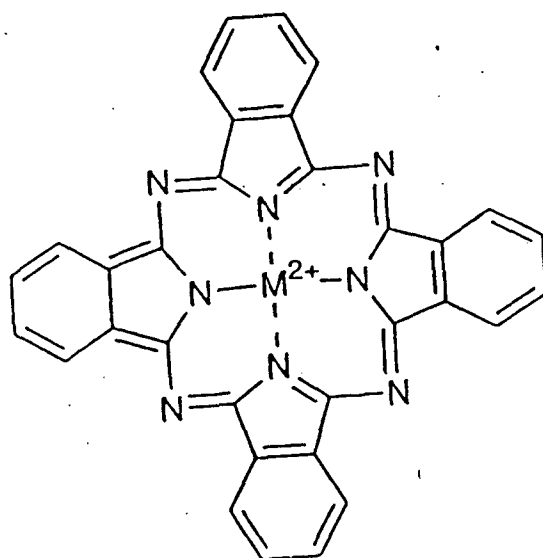


Fig. 2.3 Molecular structure of Metal phthalocyanine

replacement of the central hydrogen molecule by a metal ion does not alter the structure of the material.

Since the center of the phthalocyanine ring is anionic and essentially bivalent in character, two univalent metal atoms or one multivalent metal atom may enter it⁴². If the central atom has a valency greater than two, the valency is satisfied by the attachment of one or more anions, situated on either or both sides of the great ring. Dihydrogen phthalocyanine is referred to as phthalocyanine or as metal free phthalocyanine. Bivalent metal phthalocyanines are described simply as, for example, copper, barium, calcium, zinc, or nickel phthalocyanine. Trivalent metal phthalocyanines are referred to with the substituent anionic group or element as, for example, chlorogallium, iodoindium, hydroxyaluminium phthalocyanines. In the quadrivalent metal phthalocyanines, for eg; tin diphthalocyanine.

2.2 NON- STOICHIOMETRY

The fluorite structure adopted by several oxides (eg. UO_2 , PrO_2 , ThO_2 and CeO_2) shows exceptional adaptability, tolerating high levels of disorder which are introduced either by dopants or by redox processes⁴³. The large interstitial sites whose presence results in

interstitial disorder dominate in this lattice. And since the lower Madelung term results in the binding of the anions to their lattice sites being less strong than that of the cations. The anion Frenkel pairs are the dominant intrinsic defects in fluorite compounds. Aliovalent dopants or redox reactions thus lead to the creation of extrinsic concentration of anionic defects: vacancies are introduced by low-valence cation dopants or by reduction; interstitials are present in the anion – excess systems created on oxidation or by doping with high - valence cations.

The fluorite structure of CeO_2 is more stable than that of ZrO_2 because the ion radius of Ce^{4+} ($0.97^{\text{\AA}}$) is more acceptable than Zr^{4+} ($0.84^{\text{\AA}}$) in eight fold coordination with oxygen ion. It has been reported that the introduction of isovalent cation like Zr and Hf into the fcc cell of ceria results in nonstoichiometric fluorite structure⁴⁴. Tetravalent dopants show a strong preference for the substitutional solution in SnO_2 and mono, di and trivalent dopants form two types of solution. Lighter elements form self-charge compensation solution which leads to both substitutional and interstitial dopant ions within the lattice. The heavier elements form substitutional solutions with anion vacancy charge compensation⁴⁵.

2.3 DEFECT THEORIES

A necessary criterion for the formation of a non-stoichiometric phase is that cation can exist in several oxidation (valence) states and non-stoichiometry is thus primarily observed in transition metal oxides, rare earth oxides, and actinide oxides. Generally the direction of the change in composition corresponds to a change in the oxidation state of the cations to the next stable state, which results in formation of the following defect types³⁵.

1. Oxygen vacancies V_O'' , oxygen-deficient oxides in which the cations are easily reduced, eg. CeO_{2-x} and $LaCoO_{3-x}$ ⁴⁶.
2. Metal vacancies V_M'' , metal-deficient oxides in which the cations are easily oxidized, eg. $Fe_{1-y}O$, $Mn_{1-y}O$, $Co_{1-y}O$.
3. Oxygen in interstitial lattice positions O_i'' , excess oxygen compounds; cations are easily oxidized in these systems, eg. UO_{2+x} .
4. Metal in interstitial lattice positions M_i'' , this type of defect is found in metal-deficient oxides together with V_M'' , eg, in $Fe_{1-y}O$.

2.3.1 Oxygen – Deficient Oxides

The structure of the MO_2 FCC lattice can be represented in two ways: as oxygen cubes alternatively occupied by cations, or as cation

tetrahedral containing oxygen ions. For the oxygen – deficient oxides the second description is preferred³⁵. The defect complexes consisting of $2(\text{Me}^{3+}), \text{V}_\text{O}^{\cdot\cdot}$ are thus naturally formed within cation tetrahedral, and they are therefore termed tetrahedral defects.

When a tetrahedral defect is formed in the FCC lattice, strain is introduced in the surrounding tetrahedral, which increases the lattice energy locally. The magnitude of this strain can be assumed to be inversely proportional to the distance from the central defect, and in the nearest – neighbor tetrahedral it is so large that the formation of new defects is excluded. There are 22 nearest – neighbour tetrahedral in the fluorite structure, and an envelope of 23 tetrahedral positions can be identified as an extended defect in the FCC lattice.

Reduction of the fluorite structured oxides such as CeO_2 leads to anion – deficient phases of which CeO_{2-x} is the most widely studied example⁴³. Analogous phases may be created by doping these oxides (eg. ThO_2 and HfO_2) with trivalent or divalent cations eg. Y^{3+} and Ca^{2+} . An interesting and important example is provided by ZrO_2 which has a monoclinic lattice at low temperatures when it is pure, and it is stabilized in the cubic fluorite structure by the introduction of Ca^{2+} or Y^{3+} .

Oxygen vacancies are created by big size difference between the substantial and host ions when replaced in the lattice⁴⁷.

These defective compounds show very high anion mobility—sufficient in some cases for the materials to be classified as super ionic conductors. Such materials have electrical conductivities comparable with those observed in molten salts. For many of the reduced fluorite oxides, their defect structure is dominated by a cluster comprising two oxygen vacancies at the opposite ends of a body diagonal in one of the anion cubes of the fluorite structure. This vacancy dimer is presumably stabilized by neighbouring trivalent ions³⁵.

2.3.2 Anion- Excess Oxides

Anion – excess phases can be prepared by doping fluorite oxides with pentavalent ions like Nb^{5+} . The low symmetry defect structure is a general feature of anion – excess fluorites⁴⁸. Two types of interstitials are found in such structures one displaced along the $\langle 110 \rangle$ axis from the center of the interstitial site and the second along the $\langle 111 \rangle$ axis. The vacancies are at the lattice anion sites.

2.4. General properties

2.4.1 CeO₂

Cerium dioxide is an inexpensive and relatively harmless material that presents several characteristics that could be potentially advantageous for photocatalytic applications²⁰.

Several techniques have been employed to synthesize nanoceria. Some of the common methods are inert gas condensation, hydrothermal synthesis, sol-gel, homogenous precipitation, salt assisted aerosol decomposition, sonochemical and microwave heating, flash combustion method, thermal decomposition etc⁴⁹. N. Audebrand et al⁵⁰ studied the CeO₂ formation by means of temperature depended X-ray diffraction and TG-DSC and they found that CeO₂ is formed at 110-150°C and the difference in experimental weight loss and theoretical weight loss was related to adsorption of gaseous products on CeO₂.

Ceria can form solid solution with various metal oxides^{21,36,51}. R. Lin et al²¹ and others⁵¹ synthesized Ce_{1-x}Sn_xO₂ mixed oxides and studied their structure and redox properties by means of differential thermal analysis and temperature programmed reduction they showed that low calcination temperature favours the formation of Ce_{1-x}Sn_xO₂ solid

solution. T. Ohashi et al³⁶ has done EXAFS study of $Ce_{1-x}Gd_xO_{2-x/2}$. They suggested that oxygen vacancies are introduced by doping trivalent Gd ion to CeO_2 and are located around both Gd and Ce ions. The association of two Gd ions and one oxygen vacancy is proposed in heavily doped solid solutions. W. Huang et al⁵² prepared $(Ce_{0.83}Sm_{0.17})_{1-x}Tb_xO_{1.915+\delta}$ and $(Ce_{0.83}Sm_{0.17})_{1-x}Pr_xO_{1.915+\delta}$ ($x = 0-0.10$) solid solution having fluorite structure by hydrothermal method which require lower temperature than ceramic methods.

G. Ranga Rao et al⁵³ and others^{54,55} characterized ceria-zirconia solid solution by UV-Vis diffuse reflectance spectroscopy and studied the effect of ceria content on the vapour phase transfer hydrogenation of cyclohexane using propane-2-ol as the hydrogen donor. Incorporation of other metal in ceria leads to the formation of ceria solid solution having better redox properties and generation of both acidic as well as basic sites involving Ce^{4+} and O^{2-} ions, respectively. M. Kamruddin et al⁴⁹ observed increase in lattice parameter with decreasing particle size mainly due to valency change of Cerium and its associated oxygen vacancies. T. Zhang et al^{37,56} reported that small amount of Fe doping ($Fe/Ce \leq 1\%$) and Mn doping⁵⁷ significantly promotes the densification and grain growth of CeO_2 ceramic and also reduces the sintering temperature. Fe ions are easy

to be dispersed on to the CeO_2 grains at a lower sintering temperature. Similar results were observed for Mn doped CeO_2 samples. G. Ranga Rao et al⁵³ prepared Cu-Ce-O and Fe-Ce-O composite catalysts for heterogeneous decomposition of H_2O_2 in neutral solution. W. Huang et al⁵⁸ found lower sintering temperature for Samarium doped cerium oxide, $\text{Ce}_{1-x}\text{Sm}_x\text{O}_{2-x/2}$ ($x = 0-0.3$) prepared by sol-gel method. It is concluded that the solid solution limit of lanthana in ceria is about 60 % ($x = 0.6$) atomic fraction of lanthanum and the progressive shift of the cubic fluorite peaks toward lower 2θ values as x is increased from 0 to 0.6 is attributed to expansion of the ceria lattice caused by the dissolution of the larger ions of the lanthana solute⁵⁹. S. Dikmen et al⁶⁰ found the solubility limit of Bi_2O_3 in CeO_2 to be around 20 mole % and reported highest conductivity for $\text{Ce}_{0.80}\text{Bi}_{0.20}\text{O}_{1.90}$ composition. Mn - CeO_2 solid solution exhibit strong clustering effect since there is a vacant cubic site in CeO_2 which facilitate clustering⁶¹.

The defects on epitaxial CeO_2 (001) film was studied by G. S. Hermann⁶² with mass spectroscopy of recoiled ions (MSRI) and direct recoil spectroscopy (DRS) and Y. Kamimura⁶³ studied $\text{CeO}_2\text{-Fe}_2\text{O}_3$ catalyst for synthesis of 3-pentanone from 1-propanol.

Ceria (CeO_2) has many applications for e.g. solid electrolytes in solid oxide fuel cell, catalysis, optical additive, cosmetic material and polishers for chemical mechanical planarization (CMP)^{64,49}. Ceria stores oxygen under oxygen excess conditions in order to maintain the stoichiometry. Cerium dioxide is one of the component in car exhaust converters for the elimination of toxic gases due to its ability to store and release oxygen⁶⁵. Ceria has a positive synergetic effect on some active catalyst phases. Ceria is common promoting component of three-way catalyst used for removing hydrocarbons, CO and nitrogen oxides from automobile exhaust due to its low redox potential between Ce^{3+} and Ce^{4+} states and high mobility of oxygen defects. In addition, the fluorite structure of CeO_2 is stable from room temperature up to its melting point unlike other oxygen ion conductors such as ZrO_2 , ThO_2 and Bi_2O_3 . CeO_2 - ZrO_2 mixed oxide has improved stability as three way catalysts^{16,66-67}. The cyclization of 1,6-hexanediol⁶⁸ into cyclopentanone was investigated over CeO_2 - MnO_x solid solution at 450°C .

Cerium oxide has shown promise in enhancing dissociation of CO on Rh/ ceria ceramics. Also cerium oxide is considered as an adsorption material for gases such as CO and NO. Most recently thin films of CeO_2 have been exploited in fabricating gas sensors for NO and

acetone vapors presenting a catalytic activity. Khodadadi et al⁶⁹ and others⁷⁰ have investigated the effect of cerium oxide as an additive in SnO₂- based gas sensors. An improved detection selectivity of carbon monoxide over methane is observed for a concentration of 10% of CeO₂.

R. Lin et al⁷¹ observed higher catalytic activity for CuO/Ce_{0.7}Sn_{0.3}O₂ catalyst in CO oxidation due to the combined effect of CuO and Ce_{0.7}Sn_{0.3}O₂. Only a small amount of CuO (6%) is needed to form the active site for CO oxidation, and excess CuO forms bulk CuO particles contributing little to the activity. The films of CeO₂ and CeO₂-SnO₂ on glass substrate film are interesting opto-electronic materials, which can be used in electrochromic displays and new generation of solar cells⁵¹. CeO₂ is a good stabilizer to maintain a tetragonal form⁷² or cubic form of ZrO₂ at room temperature since ionic radius of Ce⁴⁺ is 0.13⁰Å longer than that of Zr⁴⁺.

2.4.2 SnO₂

SnO₂ is an n-type semiconductor and has many applications. Sharp XRD peaks of SnO₂ indicate increase in crystal size due to the annealing process. Average particle sizes of about 4,12,18 and 60 nm were obtained for the annealed material from 200 – 800⁰C. Samples

obtained by precipitation of SnCl_4 at low temperature are poorly crystallized rutile SnO_2 ²⁶. SnO_2 films calcined at high temperature are highly crystalline⁷⁴. It has shown that the surface of SnO_2 adsorbs greater quantity of water than oxygen⁷⁵. Water is strongly bound to a SnO_2 surface possibly as Sn-OH group. On heating only minor water is lost at 100°C , the major loss occurs over the temperature at around $240\text{-}400^\circ\text{C}$. G. Korotcenkov et al⁷⁶ found that the surface modification of SnO_2 films by Cu, Fe, Co and Mn oxide via (SILD) successive ionic layer deposition technology is an effective method for influencing the gas response of SnO_2 based gas sensors to reducing and oxidizing gases. Surface modification is due to formation of schottky barriers or p-n heterojunctions at the SnO_2 clusters interface because oxides of Mn, Cu and Co are semiconductors with p-type conductivity. The addition of Mn in the solution for preparing SnO_2 powders increases the resistance of the SnO_2 ceramic by more than 10^2 times⁷⁷.

M. M. Bagheri-Mohagheghi et al⁴⁰ prepared single phase $\text{SnO}_2 - \text{ZnO}$ thin films deposited at 480°C with Zn content upto 7.2 atomic %. At Zn content more than 7.2 atomic % part of Zn^{2+} ions move in Sn^{4+} or interstitial site and the other part of ions form new phase. Sn substitution for Ti in rutile TiO_2 or vice versa, does not give rise to extra

electrons in the conduction band or holes in the valence band of the material since Sn and Ti are isovalent.

2.4.3 PHTHALOCYANINES

In a phthalocyanine (Pc) moiety, the four coupled benzopyrrole units forming the characteristic macrocycle produce a quite stable bonding system and the properties are determined by the conjugated π electron system of the whole molecule. This arrangement becomes more stable when a metal atom is complexed by the four inner nitrogen atoms⁷⁸. Several phthalocyanines hold the metal atom in the center of the ring by a covalent bond while other phthalocyanines hold the metal atom by an electrovalent bond. Mercury phthalocyanine is said to be an electrovalent compound because it is insoluble in organic solvents and easily decomposed to phthalocyanine in acidic solution. Copper phthalocyanine is covalent. Phthalocyanine compounds were the first examples of planar symmetry for cobalt, iron, and manganese metals³⁸.

Phthalocyanine compounds exhibit stability to heat and decompose at elevated temperature⁷⁹. The stability increases sharply when the cation is capable of forming σ bonds, as a result of its greater electron affinity and the possibility of the 3d or 4d levels being filled with the

ligand electrons. Substituted phthalocyanines are less stable than unsubstituted phthalocyanines¹². Very high thermal stability of the phthalocyanine molecule is due to its extremely high aromatic character which exceeds that of a benzene ring by a factor of 15^{80} . An interesting phenomenon is observed in the coordination reactions between metal salts and phthalocyanine. H_2Pc is monoprotinated by concentrated H_2SO_4 at a peripheral rather than a central nitrogen atom. The H_2PcH^+ has an unbound coordination center. Due to which Pc readily form complexes when the Cu^{2+} salt is brought in contact with its sulphuric acid solution. All Pc complexes and the H_2Pc ligand itself are liable to dissociate in sulphuric acid solution. If the cation is not capable of forming strong σ bond because of the weak electron affinity or not being capable of dsp^2 hybridization, that is planar arrangement of the σ bonds then labile complexes are formed. Examples are Li^+ , Na^+ , Ca^{2+} , Hg^{2+} , Pb^{2+} etc whereas Cu^{2+} , Ni^{2+} , Co^{2+} , Fe^{3+} , Mn^{3+} , Zn^{2+} and Pd^{2+} form stable complexes³⁰. The considerable stabilization of complexes $CoPc$ and $CuPc$ is accompanied by a decrease in their shift of the first absorption band due to formation and strengthening of the backward dative π bonds which stabilize the complex. The formation is presented by no distortions of the ligand. $NiPc$ is much less stable than $CuPc$ due to steric factor. Cation

Ni^{2+} produces a tangible effect on the Pc ligand. By pulling together the four N atoms it reduces the size of the ligand's inner space, changing the valence angles of the C-N-C bonds and impairing the conditions for the π overlap in the macroring.

Phthalocyanines have good sensitivity to the toxic gases like NO_2 due to its properties of good chemical and thermal stability⁸¹. CuPc and H_2Pc have higher sensitivity to NO_2 compared to other MPcs²⁹. The metal with atomic radii very close to 1.35 \AA form metal-phthalocyanine complexes which make them thermally stable and a resistance towards concentrated sulphuric acid^{82,30}. Some of them are resistant to atmospheric oxidation at 100 $^\circ\text{C}$ or higher. In aqueous acid solution, strong oxidizing agents oxidize phthalocyanines to phthalic residue, whereas in non-aqueous solution an oxidation product that can be reduced readily to the original compound is usually formed. Reduction in the phthalocyanine molecule can take place at the central metal atom or at any of the 16 peripheral carbon atoms on the four phenylene rings. The extent of reduction depends on the valency state attained by metal atom and by the phthalocyanine ligand. The highest valency state that can be attained is four.

Phthalocyanine compounds are organic semiconductors and behave as a catalyst under certain conditions⁴². They participate in photochemical reactions and may luminesce or fluoresce. They play a significant role in the development of radioisotope applications such as in medical therapy. Phthalocyanine and phthalocyanine type compounds possess remarkable colour properties. Several thousand phthalocyanine dyes has been synthesized by the attachment of sulphuric acid groups, ternary and quaternary salt groups, sulphur containing groups, azo groups, vat dye groups, leuco groups, chrome groups, precursor groups, triazine compounds, and other groups to from 1 to 16 of the peripheral carbon atoms of phthalocyanine molecule. They have been used as thickeners for high temperature greases. CuPc is a good charge generating material⁸³. N. Sehlotho et al⁸⁴ studied the oxidation of cyclohexene over Co and Fe phthalocyanine complex and reported PcM species as an intermediate for PcCo^{II} and PcFe^{II} catalyst. Valence state of Iron in FePc is 2+.

Thermal stabilities, IR, UV/Vis spectra and other physical properties of Iron and CoPc are strongly influenced by the peripheral substituents. The Pc's, in the solid state behave as p-type semiconductors, characterized by energy of the band gap about 2 eV. Upon irradiation with visible light $\lambda \geq 460$ nm it is possible to excite the Pc molecule.

J. G. Guan et al⁸⁵ synthesized Co-Pc/Fe nanocomposite particles with high magnetic susceptibility.

Phthalocyanines are organic light emitting diodes (OLED'S), solar cells, organic field-effect transistors, molecular gas sensors, memories, optoelectronic device and semiconductive junctions⁸⁶. CuPc layers are employed as hole transporting materials in photovoltaic cells and thin film transistors. Metallophthalocyanines (MPcs) are particularly attractive as potential catalysts for organic reactions such as oxidation because of their rather inexpensive and simple preparation on a large scale, ability to absorb oxygen and its chemical as well as thermal stability⁴⁴. The first mention of phthalocyanine compounds as catalysts is the work of Calvin, Cockbain and Polanyi who studied the effect of the presence of crystals of Pc and CuPc on the activation of molecular hydrogen. Since then the Pcs have been used as catalyst in the conversion of para hydrogen, the reaction between hydrogen and deuterium oxide, the decomposition of H₂O₂, isomerisation of dimethyl maleate to dimethyl fumarate and the polymerization of methyl methacrylate⁴². They act as photosensitizers^{87,88} and can be used for photodynamic therapy of cancer^{89,90}.

S. Seelan et al⁹¹ has reported the activity of CoPc complexes encapsulated in zeolite -Y for phenol hydroxylation reaction. They also reported that CoPc complexes are model dioxygen carriers and may be used to separate molecular oxygen from gas mixtures. L. Jain et al⁹² used Co phthalocyaninesulfonamide for the oxidation of α - hydroxyketones to α - diketones. Carbon electrodes are modified with first row transition metal phthalocyanine for water electrolysis in basic media⁹³.

2.5 Electrical properties

The basic property of a semiconductor is electrical conductivity which depends on the mobility and concentration of the charge carriers. The electrical properties are sensitive to the impurity content and doping. Organic semiconductors are molecular crystals whose energy structure and electronic properties are determined by the molecular structures⁴¹.

2.5.1 Theory

The electrical conductivity in semiconductors is caused by thermal excitation of electrons, impurities, lattice defects and nonstoichiometry. A highly purified semiconductor exhibits intrinsic conductivity. In the temperature range at which the intrinsic conductivity is exhibited the

electrical properties of the crystal are not modified by impurities. In organic semiconductors as the temperature is increased from absolute zero, electrons are thermally excited from the valence band to the conduction band. The conductivity due to the electrons and holes ⁴³,

$$\sigma = (n_e \mu_e + p_h \mu_h) \dots\dots\dots 1$$

Where n_e and μ_e are the carrier concentration and mobility of the electrons. p_h and μ_h are the corresponding quantities for the holes. In an intrinsic semiconductor, the no of electrons is equal to the no of holes.

The expression for carrier concentration is given by

$$n_i = N_c \exp E_F / kBT$$

$$p_i = N_v \exp - (E_F + E_g) / kBT \dots\dots\dots 2$$

where N_c and N_v are the density of states in the conduction band and valence band. E_g is the forbidden energy gap, k_B and T are the Boltzmann's constant and absolute temperature respectively.

N_c and N_v are given by

$$N_c = 2 (2\pi m_e^* kBT / h^2)^{3/2}$$

$$N_v = 2 (2\pi m_h^* kBT / h^2)^{3/2} \dots\dots\dots 3$$

Where m_e^* and m_h^* are the effective masses of the electrons and holes respectively.

Since $n_i = p_i$

$$n_i = p_i = 2 \left(\frac{2\pi k_B T}{h^2} \right)^{3/2} (m_c^* m_n^*)^{3/2} \exp \left[-\frac{E_g}{2k_B T} \right]$$

$$= A \exp \left(-\frac{E_g}{2k_B T} \right) \dots\dots\dots 4$$

where A is a constant

If we assume that the variation of mobility of the electrons and holes in an electric field with temperature is small, then conductivity is proportional to the no of carriers and has a variation of the form

$$\sigma = \sigma_0 \exp \left(-\frac{E_g}{2k_B T} \right) \dots\dots\dots 5$$

where σ_0 is a constant. Such an exponential variation of electrical conductivity is known for semiconductors. Multiple donor levels exist within the forbidden energy gap and deeper levels can be frozen out as the temperature is increased. If the substance behaves like an ideal semiconductor following equation 5 the plot of $\log \sigma$ and $1/T$ should be a straight line, the slope of which will determine the energy of activation for conduction.

2.5.2 Mixed conduction in oxides

a) Cubic- fluorite oxides

A number of well known oxides CeO_2 and ZrO_2 crystallize with the cubic fluorite structure and ZrO_2 only if stabilized by the addition

of sufficient levels of di-or trivalent impurities. Each of these systems can accommodate large additions of alkaline earth and rare earth oxides in solid solutions. The di and trivalent ions enter the fluorite lattice substitutionally at cation sites, thereby stimulating the formation of uncommonly high concentrations of oxygen vacancies approaching 10-15 mole %. These high levels of ionic defects, coupled with relatively high ion mobilities, combine to give high ionic conductivities⁹⁴.

The band gap of all these systems are reported to be ~ 5 eV and so possess low intrinsic concentrations of electrons and holes even at elevated temperature. The conduction bands of these oxides appear to be of either a d or f nature⁹⁴, which favour low electron mobilities (μ_n). The valence band, on the other hand, believed to be of oxygen 2p character, which supports electron- hole mobilities (μ_p).

b) Cerium Dioxide

i) Undoped CeO₂

Cerium dioxide, CeO_{2-x} because of its multivalent cation (Ce⁴⁺, Ce³⁺)⁹⁵, deviates strongly from stoichiometry at elevated temperature and reduced PO₂ to produce an oxygen – deficient n-type semiconductor. Extensive measurements of σ (T, PO₂) coupled with thermoelectric and

thermo-gravimetric data show that doubly ionized oxygen vacancies, the dominant ionic defect at small x ($x < 10^{-3}$) is displaced by singly ionized vacancies at larger x .

For very small x in CeO_{2-x} , it becomes a mixed conductor and under such conditions the ionic conductivity is controlled by background impurities. Measurements of electronic conductivity in combination with thermoelectric power or thermo-gravimetric data have confirmed that electron transport in CeO_{2-x} proceeds via a small polaron process. All studies find μ_n to be activated with hopping energies in the range of $\sim 0.2 - 0.6$ eV as x increases from 0.01 to 0.25. The variation in E_H has been related to the onset of defect ordering at larger values of x .

ii) Doped CeO_2

Addition of di and trivalent cation impurities to CeO_2 serves to increase its ionic conductivity. For dopant levels of > 1 mole %, doped CeO_2 becomes a predominantly ionic conductor at high PO_2 values and temperatures below $\sim 1000^\circ\text{C}$. The electrolytic domain shrinks as the temperature is increased which is due to the increasing tendency for Ce^{4+} to be reduced to Ce^{3+} at elevated temperature.

Specimens doped with different impurities but at equivalent dopant levels do not result in equivalent electrolytic domains. It may be observed that doping with pentavalent impurities, ie, Ta and Nb, serves to increase the electronic conductivity in CeO_2 by orders of magnitude in air, indicating that such impurities enter the lattice substitutionally. Doped ceria system is generally known to have lower activation energy than commonly used zirconia-based solid electrolyte. CeO_2 - ZrO_2 system in ZrO_2 -rich region has potential applicability as a solid electrolyte. Size effect was considered the possible reason for conductivity enhancement concerning the strain induced oxygen vacancy generation from the size difference between host and dopant ions. Y_2O_3 -doped 10 mol % ZrO_2 - CeO_2 solid solutions showed mixed conducting property with predominant electronic conduction at lower doping conc. And gradually transform to pure conductor at higher doping concentration⁹⁶.

c) Applications

Mixed conductors play an important role in many practical applications. The majority of applications take advantage of the extended high ionic conductivity that a number of oxides exhibit over extended operating conditions. Because of their stability and reasonably high

conductivities the cubic fluorite oxides including zirconia and ceria have received the most attention. Efforts are being directed to enhance the electronic conductivity of these materials by doping with multivalent or pentavalent ions.

2.5.3 Electrical properties

i) CeO_2

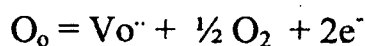
CeO_2 is reported to be a predominantly ionic conductor, exhibits n-type conductivity under certain conditions⁹⁷.

The impedance spectra of $\text{CeO}_2: 20\text{Gd}$ thin films show only one semicircle from bulk and grain boundary resistance⁹⁸. The measurements of electrical conductance as a function of oxygen partial pressure and temperature provide the information about the type of conductance and thermodynamic parameters of the defects. It is observed that the electronic conductivity increases and activation energy decreases as the grain size decreases. The activation energy for nano-crystalline specimens is between 1.0 and 1.3 eV, which is close to the value reported for the grain boundary conductivity. The transition from extrinsic to intrinsic type of conductivity was observed for 30 nm grain size CeO_2 specimen at elevated temperature, while for $\text{CeO}_2: 20\text{Gd}$ conductivity has

extrinsic character. The ionic conductivity in CeO₂: 20Gd increase as the grain size decrease which can be explained by the reduction of the activation energy due to the segregation of impurities in the grain boundary volume⁹⁸.

ii) SnO₂

Pure SnO₂ is a n-type semiconductor since oxygen vacancies or interstitial Sn⁴⁺ are donor sites⁴⁵. Doped SnO₂ samples are characterized by high electrical conductivity due to the formation of doubly ionized oxygen vacancies⁹⁹.



In Er-doped SnO₂ thin films, Er³⁺ is expected to be an acceptor in SnO₂ since when it substitutes Sn⁴⁺ in the Cassiterite structure, removes an electron from valence band, leaving a hole, which may recombine with a free electron. Very high resistivity value of Er-doped SnO₂ film and Eu-doped SnO₂ powder was observed. This is an evidence of acceptor like character of Er³⁺ in SnO₂, since the n-type conduction of undoped SnO₂ film is greatly compensated by Er³⁺ introduction⁹⁸. SnO₂ thin films close to stoichiometry, have low carrier concentration and high resistivity ($\rho \sim 10^8 \Omega \text{ cm}$), which is similar to oxides. Non- stoichiometric tin oxide

thin films have high free carrier concentration between 10^{18} and 10^{20} cm^{-3} . In SnO_2 -ZnO thin films, with increasing Zn content up to 12.5 atomic %, resistivity of films increases. However, with Zn content up to 20.7 atomic % sheet resistance decreases sharply and then in higher Zn content increases again⁴⁰.

An increase in porosity results in decreased conductivity. Sb doped SnO_2 presents metal like properties⁹⁹. However, the sol-gel route normally leads to films with a relatively high resistivity, and their high porosity (low density) is the reason for their low conductivity. Films with resistivity in the range of $10^{-3} \Omega \text{ cm}$ were obtained for [Sb]/ [Sn] ratio. J. Tan et al¹⁰⁰ found that in antimony doped tin oxide the resistivity decreases and the electrical conductivity increases with the molar ratio of $\text{Sn}^{4+}/\text{Sb}^{3+}$ decreasing and maximum for molar ratio 12.5:1. The conductivity is poor at 673K due to replacement of Sn^{4+} lattice sites by Sb^{3+} ions. The localized energy level of the defect located near the top of valence band, and the vacancy bound flabbily is excited to fall in the valence band by attaining certain energy to have electronic conductivity and thermal conductivity. Thus SnO_2 forms a p-type semiconductor which is likely to be caused by the relatively difficult replacement of slightly larger Sb^{3+} ion at low temperature. The less current carrier formed

led to a poor σ . The electrical conductivity of antimony doped oxide increases with calcining temperature because Sb^{3+} ions are oxidized to Sb^{5+} ions gradually which are of smaller radius than that of Sn^{4+} ions. The defect formed by the replacement of Sn^{4+} lattice site with the Sb^{5+} ion is equal to a monovalent cation bound flabbily by an Sb_{Sn}^+ . The defect give out electron with the formula of $\text{Sb}_{\text{Sn}}^x + E_{\text{D}} \rightarrow \text{Sb}_{\text{Sn}} + e^-$ to show as a donor defect and form an n-type semiconductor. When the energy of defect accepted is larger than or equal to E_{D} , the electrons can be excited into conduction band to form a conductive current carrier. Because the mobility rate of the e^- is larger than that of the cavity, the conductivity increases. With calcination temperature increasing above 1073K, the resistivity of antimony doped tin increases and the electrical conductance decreases because of the reduction of Sb^{5+} ions partly, leading to a decrease of Sb^{5+} ions to replace Sn^{4+} lattice sites and a decrease of electron current carrier, but an increase of cavity current carrier. J. M. Hermann et al¹⁰¹ studied the electrical conductivity of Mo-Sn-O system.

iii) PHTHALOCYANINES

Phthalocyanines are a class of organic semiconductors, whose electrical properties have considerable importance owing to their potential application in electronic devices and sensor systems.

Shihub and Gould¹⁰² have calculated the activation energy of CoPc films as 0.54 eV and concluded that conductivity is mainly of the free band type in the high temperature low frequency region, whereas it is of the hopping type in the low temperature high frequency region. In evaporated CuPc thin films, Gould and Hassan¹⁰³ have also studied the a. c. electrical properties in the frequency range 100 Hz – 20 KHz and temperature range 173-360K. A. Vidadi et al¹⁰⁴ investigated the a. c. conductivity of preheated samples of CuPc and MgPc in vacuum. Their observations are in agreement with the results of Shihub and Gould¹⁰².

CoPc single crystal is a p-type material and exhibits ohmic conductivity at low applied voltages. It has similarity in conductivity with β -NiPc single crystal due to similarities in band structure¹⁰⁵. Semiconducting behaviour of Pc films is p-type at all temperature and has three linear regions on graph of $\ln R$ Vs $1000/T$. E_1 arises from holes as the charge carriers, E_2 and E_3 from impurity scattering^{79,85}.

Annealing decreases the activation energy due to redistribution of traps⁴¹. The reduction values of both capacitance and conductance observed after heat treatment may be attributed to the desorption of oxygen from the CoPc molecules which are bonded by weak coupling forces. It was suggested that freshly prepared samples may contain different kinds of defects such as vacancies, grain boundaries and dislocations which may be partially annealed out by heat treatment resulting in a decrease in the density of defects and in local structural rearrangements. The desorption of oxygen which is a major source of intrinsic conductivity leads to an increase in the resistance of the material, thus proving the sensitivity of the electronic conduction of phthalocyanine to the presence of oxygen. The annealing temperature of 450K is sufficient to desorb oxygen without causing structural changes in the material¹⁰².

Semiconducting property of the CuPc polymorphs can be accounted for the differences in the interaction of the highly conjugated π -electrons between the molecules, inter-molecular spacing and the nature of the molecular stacking along the 'b' axis. β -form is the most stable which can be crystallized¹⁰⁶.

2.6 ESR STUDY

The shifting of a g value from 2.0023 in a transition metal complex is due to the mixing, via spin-orbit coupling of the metal orbitals involved in molecular orbitals containing the unpaired electrons, with the empty or filled ligand orbitals¹⁰⁷. When the mixing is with the empty ligand orbitals, the result is a negative g shift, whereas the mixing with the filled ligand orbitals leads to a positive g shift. This depends on the amount of the unpaired electron density at the donor sites of the ligands i.e. on the degree of covalency of the complex.

In a coordination complex, the unpaired electron of the metal ion is delocalized to the donor sites of the ligands or to the chelate ring or even to the atoms outside the chelate ring. In CuPc, the unpaired electron of copper (II) spends 35-36% of its time in the nitrogen donor sites of the ligand phthalocyanine. The ESR singlet at $g = 2$ is specific for the presence of a crystalline phase and it is associated with the presence of defects in the crystal lattice¹⁷. The EPR spectra of α and β -CoPc complexes exhibit an axial symmetry with 2 principal g values¹⁰⁸. The ESR investigations showed the formation of microcrystals of the Pc complexes. In the case of Pc diamagnetic complex, anchored on supports narrow ESR singlet at $g = 2$ is the evidence for the formation of

microcrystals. The ESR spectra of paramagnetic CoPc is more difficult because of the short spin- lattice relaxation times and the high sensitivity to exchange interactions²⁷.

2.7 MAGNETIC STUDY:

According to Y. Hinatsu et al¹⁰⁹ oxygen deficient CeO_{2-x} is paramagnetic and the average state of the cerium ion is between +4 and +3¹¹⁰. The transition temperature (the Neel temperature) for $Ce_yU_{1-y}O_2$ solid solutions with $y \leq 0.35$ decreases with increasing cerium concentration (y). An antiferromagnetic transition has been observed for the solid solutions with $y \leq 0.3$, but the Neel temperature are lower than those of the oxygen stoichiometric solid solutions due to formation of oxygen vacancies which transfers magnetic interactions between uranium ions.

The magnetic susceptibility and magnetic moments of square planar metal octabromophthalocyanine pigments (MPOBr) have been studied by K. R. Venugopala Reddy et al¹¹¹ in the solid state and revealed that CuPOBr and CoPOBr are paramagnetic and that NiPOBr and ZnPOBr are diamagnetic. The observed magnetic moments for CuPOBr and CoPOBr are higher than one unpaired electron (1.73BM) which is

related to the orbital contributions due to the mixing of ground state orbitals $(b_{2g})^2$, $(e_g)^4$ and $(a_{1g})^1$, and higher orbitally degenerate states $(b_{2g})^2$, $(e_g)^3$ and $(a_{1g})^2$. The observed higher values of μ_{eff} at lower field strength for Cu and Co is attributed to intermolecular magnetic interaction coupled with the magnetic anisotropy of the strong phthalocyanine π -electron current⁸². The effective magnetic moment from magnetic susceptibility for FePc was found to be intermediate between theoretical spin only value $s = 1$ and $s = 2$ state¹⁰⁸.

2.8. UV-VISIBLE SPECTROSCOPY

Several theoretical calculations for the D_{4h} symmetry of the metallophthalocyanine molecules predicted five distinct bands (Q, B, N, L and C) in the spectral region between 200 and 800 nm. The Q band corresponds to the excitation between HOMO (a_{1u}) to LUMO (e_g), while B band is mostly an $a_{2u} \rightarrow e_g$ transition. Both (Q and B) bands are characteristics for the phthalocyaninato ligand. The N, L and C bands resulting from a contributions of $a_{2u} \rightarrow e_g$, $a_{2u} \rightarrow e_g$ and $a_{1u} \rightarrow e_g$ transitions^{108,112}.

2.9 UV- VISIBLE DIFFUSE REFLECTANCE SPECTROSCOPY

The DRS technique provides information about the electronic transition (d-d transition) and band gap of doped and undoped semiconductor³³. The diffuse reflectance (DRS) and its application to study metal oxides have been reviewed recently¹¹³.

In a diffuse reflectance spectrum, the ratio of the light scattered from a thick layer of sample and that from an ideal non-absorbing reference sample is measured as a function of the wavelength⁴. Very small particles have a large bandgap due to quantum size effects⁷³. The incorporation of ceria to TiO₂ induces small red shift of the electronic absorption with respect to pure TiO₂ anatase and larger contribution of Ce⁴⁺ - O²⁻ charge transfer transitions which yield relatively broad band with a maximum at 380 nm¹⁷.

N. Sergent et al¹¹⁴ reported that SnO₂ calcined at 100⁰C in O₂ show distinct absorption bands at 210, 230 and 280 nm. The absorption bands at 210-230 nm corresponds to Sn (IV) species while the band at 280 nm would be assigned to either intervalence Sn⁴⁺/Sn²⁺ transitions or S-P transitions characteristic of Sn²⁺ ions. Sample heated at 200-300⁰C in O₂ show additional bands at 250-320 nm attributed to Sn⁴⁺/Sn²⁺ intervalence transfer or Sn²⁺ S- P transitions. After heating at 400- 600⁰C in show a

marked absorption in the visible range adjacent to the valence/conduction transition. Simultaneously the solid colour changes irreversibly from white to yellow that can be related to the loss of oxygen atoms leading to a non- stoichiometric SnO_{2-x} . The side band observed between 350 and 550 nm in the R.T. uv spectra is mainly related to mono ionized oxygen vacancies¹¹³.

2.10 PHOTOCATALYTIC STUDIES

For the removal of recalcitrant pollutants, traditional physical techniques like adsorption on activated carbon, ultra-filtration, reverse osmosis etc can generally be used efficiently. They are non-destructive since they just transfer organic matter from water to sludge. Consequently, the regeneration of the adsorbent materials and post treatment of solid wastes are expensive operations⁹.

In recent years advanced oxidation processes (AOPs) have been developed to meet the increasing need of an effective wastewater treatment. AOP generates powerful oxidizing agent hydroxyl radical which completely destroys the pollutants in waste water. Heterogeneous photocatalysis through illumination of UV (or) solar light on a semiconductor surface (SC) is an attractive advanced oxidation process.

Photodegradation of pollutants using SC with solar light can make it an economically viable process since solar energy is an abundant and inexpensive natural energy source¹¹⁵. This solar energy can be used instead of artificial light sources. These sources need high electrical power which are costly and hazardous. Solar energy has been successfully used for photocatalytic degradation of pollutants¹¹⁶. The main advantage of the photocatalytic process is its mild operation conditions.

In general, solids with bandgap energies less than 3 eV are considered to be semiconductors¹¹⁷. In a semiconductor the highest occupied and the lowest empty energy bands are particularly important. The highest occupied energy band is called the valence band and the lowest empty energy band is the conduction band. Semiconductors can be made conductive either by adding extra electrons into the conduction band or by removing electrons from the valence band. Removal of an electron from the valence band creates a positively charged vacancy called a hole that can be regarded as the mobile entity. So electric current can be carried either by electrons in the conduction band or holes in the valence band, or by both type of charge carriers. Mobile charge carriers can be generated by three different mechanisms.

1. Thermal excitation
2. Photoexcitation
3. Doping

If the bandgap energy is sufficiently small (less than half an electron volt) thermal excitation can promote an electron from the valence band to the conduction band. In a similar manner, an electron can be promoted from the valence band to the conduction band on absorption of a photon of light ie photoexcitation, provided that $h\nu > E_{bg}$. The third mechanism of generating mobile charge carriers is doping. Fig.2.4 shows the mechanisms of charge generation.

Doping is the process of introducing new energy levels into the bandgap. There are two types of doping, n-type and p-type. For n-type doping, occupied donor levels are created very near to the conduction band edge and current is mainly carried by negative charge carriers. Likewise, in p-type doping empty acceptor levels are formed near the valence band, creating positive charge carriers. The current is carried by these positive charge carriers.

The various semiconductor particles acting as photocatalysts have been used. Most attention has been given to TiO_2 because of its high photocatalytic activity, resistance to photocorrosion, biological

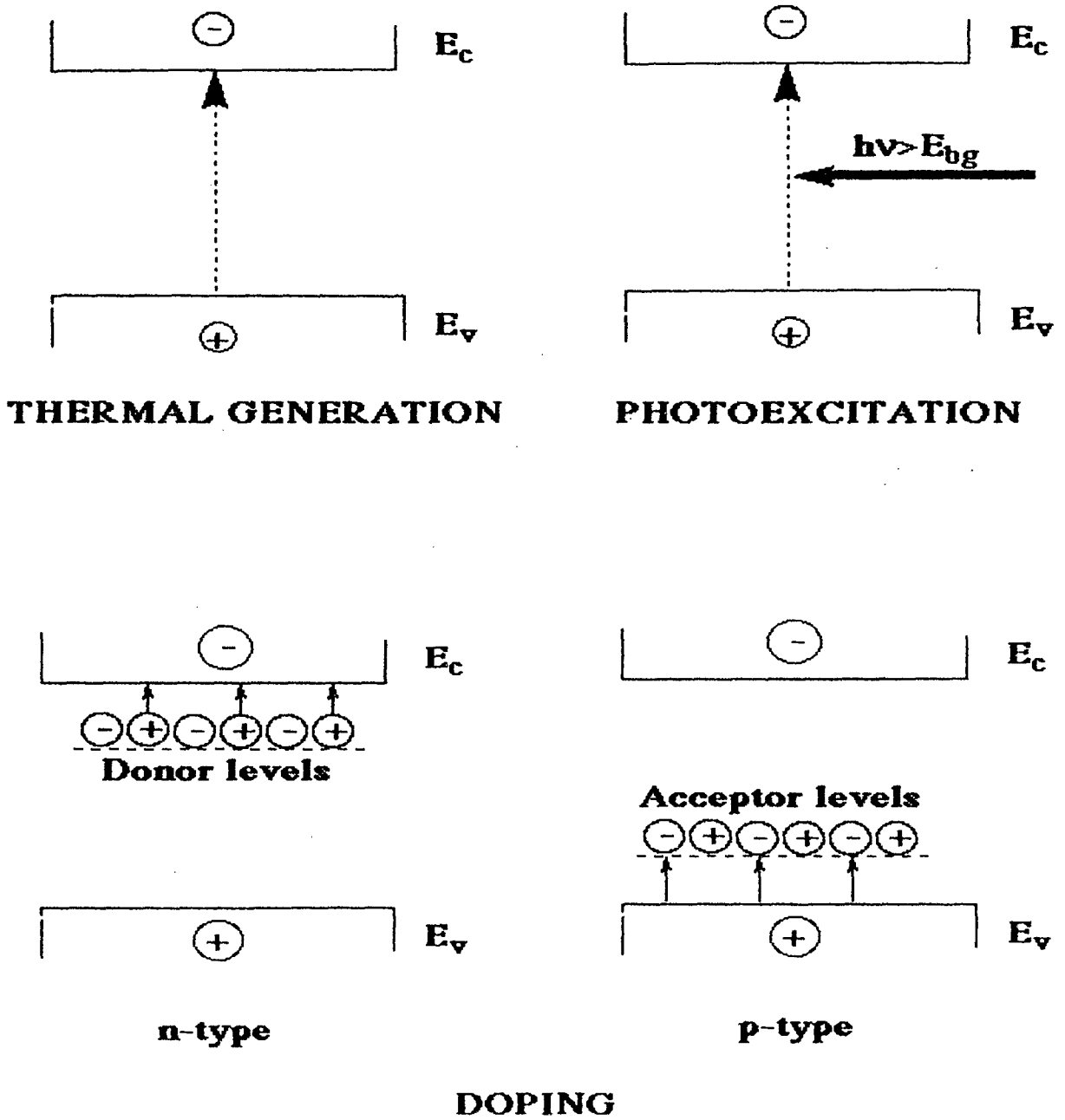


Fig.2. 4 Different mechanisms of generating mobile charge carriers

harmlessness and low cost. Hence the photocatalytic decomposition of frequently used dyes over TiO_2 has been investigated¹¹⁸. The photooxidation of organic substances catalyzed with TiO_2 semiconductor was first published by Carry in 1976 who dealt with the photodecomposition of chlorobiphenyl compound in heterogeneous TiO_2 particle dispersions¹¹⁸. T. Zhang et al¹¹⁵ investigated the photocatalyzed N-demethylation of Methylene Blue with decomposition of MB using solar irradiation source and Degussa P-25 TiO_2 as the photocatalyst in aqueous dispersions. Photocatalytic destruction of MB follows pseudo-first order kinetics. The photocatalytic degradation of azo dye Reactive Orange 4 (RO4) in aqueous solution with TiO_2 -P25 as photocatalyst in slurry form has been investigated using solar light. Degradation was strongly enhanced by electron acceptors such as H_2O_2 , $(\text{NH}_4)_2\text{S}_2\text{O}_8$ and KBrO_3 ¹⁴. M. V. Shanker et al¹¹⁹ degraded Reactive dyes using TiO_2 slurry in a batch reactor using UV irradiation. Addition of H_2O_2 enhances the degradation efficiency. S. Sakthivel et al¹²⁰ investigated the photodegradation of leather dye Acid Brown 14 over TiO_2 catalyst supported on Alumina and glass beads. They suggested a new approach for prevention of recombination by incorporating more effective adsorption sites.

Hariprasad J. S. et al⁹ studied the photodecolourisation of reactive textile dyes using ZnO catalyst and sunlight. Complete decolourization (100 %) was obtained when ZnO was used in presence of sunlight as compared to UV light. The degradation kinetics involved Langmuir-Hinshelwood model and addition of H₂O₂ enhanced the rate of decolourization. Photobleaching of Rose Bengal (RB) on ZnO powder was carried out in presence of light by A. Sharma et al¹²¹ and the effect of variation of different parameters, like concentration of RB, pH, amount and particle size of the SC and light intensity on the rate of bleaching were observed. Similar observation was made for degradation of sulphur containing heterocyclic compounds 2-methylthiophene⁸ and G. R. Rajarajeshwari et al¹²² carried out photocatalytic oxidation of an organic dye Violet 5BN using immobilized ZnO and UV light. L. S. Roselin et al¹²³ investigated the photocatalytic degradation of three reactive dyes Reactive Red 22, Reactive Yellow 15 and Reactive Blue 28 using ZnO and sunlight. Complete decolourisation and mineralization can be achieved using solar light.

V. Pareek et al¹²⁴ has studied the thermodynamic efficiency of photocatalytic processes. S. N. Paleocrassas¹²⁵ reviewed photolysis of water using sunlight. It is often suggested that surface hydroxyl groups

play an important role in determining the photocatalytic activity, since these species act as traps for photogenerated holes to form hydroxyl radicals and reduce electron - hole recombination³⁴. H. Chun et al¹²⁶ showed that in the photodegradation of reactive dyes, the azo group was attacked by OH \cdot at two positions. One at single bond of C-N from azo group connecting with benzene ring and other at double bonds of azo group. The N of azo group was converted to N₂ and NH₄⁺ ions. The photocatalytic activity is influenced by the crystal structure, surface area, size distribution, porosity, band gap and surface hydroxyl group density¹³.

2.10.1 Conditions for maximum photocatalytic efficiency

The materials that can be used as photocatalysts must satisfy certain conditions. They are¹¹⁶:

1. The particulate system must absorb maximum amount of incident light.
2. There should be rapid charge separation succeeding the light absorption act, ie h⁺ - e⁻ separation, electrons (e⁻) are excited from the valence band to the conduction band; this increases electron density in the conduction band and leaves positive hole (h⁺) behind. They should not recombine before they have assisted the chemical reaction.

3. The substrate should undergo a redox reaction. Hence the redox potential of the substrate and the redox potential of the excited catalysts must be compatible.
4. There must be a facile removal of the photoproduct otherwise the reverse reactions and secondary reactions will suppress the overall yield.
5. The catalyst should have long-term stability for continuous use.

2.10.2 Semiconductor energetics

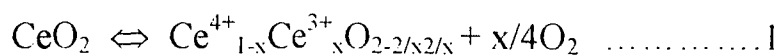
When light of energy $h\nu > E_g$ (band gap) falls on the semiconductor, $e^- - h^+$ pairs are generated. The electron excited into the conduction band drifts towards the bulk and the hole in the valence band drifts towards the surface. The Fermi level is the redox potential of the semiconductor. When the semiconductor is in contact with a solution containing a reactant, equilibrium can be achieved by changes in charge

densities and consequent leveling of Fermi level of the semiconductor and the redox potential of the reactant redox system. When a semiconductor powder is under consideration we recognize four regions, viz. i) bulk ii) space charge layer iii) surface of the particle and iv) solution phase.

Bending of the energy levels near the space charge layer is a very important event^{116,127}. With n-type semiconductor such a bending is upward; with p-type it is downwards. With n-type the surface is concentrated with respect to hole and the reverse is true of p-type semiconductor.

2.10.3 Ceria as a photocatalyst

The catalytic activity of ceria may be related to the oxygen evolution¹²⁸ and absorption equilibrium reaction (1) as shown in the equation below:



Oxygen defect, $0 < x < 1$

The ideal $r(\text{M}^{n+})/r(\text{O}^{2-})$ ionic size ratio of a MO_8 eight coordination oxide is 0.732. In the case of the fluorite structure of ceria,

$r(\text{Ce}^{4+})/r(\text{O}^{2-})$ is 0.703, which is smaller than that of the ideal value, indicating that Ce^{4+} is not large enough to stabilize the fluorite structure. To take on a more stable eight coordination of the fluorite structure, some Ce^{4+} have a tendency to be reduced to Ce^{3+} , which has a larger ionic radius than Ce^{4+} as shown in equation 1. Accompanying this reaction, oxygen molecules are released to form oxygen vacancies. By doping Ca^{2+} , which possesses a lower valence and larger ionic size than Ce^{4+} , with CeO_2 , stabilizes the fluorite structure of ceria and consequently reduces the oxidation catalytic activity.

The low photocatalytic activity of ceria is due to the existence of an oxygen defect that plays an important role to enhance the recombination reaction of photoinduced electrons and holes¹⁷. Even undoped CeO_2 itself has a tendency to form an oxygen defect. By doping CaO with CeO_2 , there is formation of a greater oxygen defect and decrease in photocatalytic activity of CeO_2 . Also, the catalytic activities of pure and doped ceria have been variously associated with, interstitial oxides, lattice oxygen atoms, oxyanion vacancies, basicity of the surface and redox activity⁵⁸.

Among photocatalytic applications, several studies have investigated the photocatalytic production of oxygen from water over

CeO₂ using Ce⁴⁺ as electron acceptor³⁴. The photoactivity of the CeO₂ nanoparticles for the oxidation of toluene shows the complete mineralization without significant catalyst deactivation²⁰. Yabe S et al¹²⁸ synthesized ultrafine particles of M²⁺ doped ceria (M²⁺ = Mg²⁺, Ca²⁺, Sr²⁺, Ba²⁺ and Zn²⁺) for using as a UV filter via soft solution route at 40⁰C. They reported that doping with 20mole % Ca²⁺ and Zn²⁺ resulted in a considerable decrease in the particle size and catalytic activity of ceria for oxidation of castor oil. CaO doped CeO₂ show excellent UV absorption and transparency in the visible ray region compared with undoped CeO₂³⁴.

Nevertheless, there is some disagreement between the different reports since CeO₂ thin films are found to be inactive for the photocatalytic degradation of methylene blue¹²⁹.

2.10.4 SnO₂ as a photocatalyst

SnO₂ is a n-type semiconductor which has been widely used for the degradation of various dye pollutants. The use of Sn_xTi_{1-x}O₂ solid solution in environmental catalysis has been examined because of its photocatalytic activity as it exhibits high quantum yield¹³⁰. It has been shown that small Sn substitution for Ti in rutile TiO₂ increases the

photoactivity of the rutile by 15 times for the oxidation of acetone. Also it endows the catalyst with major photoactivity to decompose methyl orange which is an organic compound model that exhibits good resistance to light degradation. Pt/Sn_xTi_{1-x}O₂ (at higher TiO₂ contents) appears to be a good catalyst for CO oxidation. SnO₂/TiO₂ coupled semiconductor system on an OTE under an anodic potential show faster degradation of azo dyes²³.

2.10.5 Phthalocyanine as a photocatalyst

Phthalocyanines and porphyrins have been used as photocatalyst for a large variety of oxidation reactions of phenol derivatives and some mechanistic aspects have also been investigated⁷. The phthalocyanines in the solid state behave as p-type semiconductor, characterized by band gap energy of about 2 eV. It is possible to excite Pc particles on irradiating with visible light¹⁴. The H₂Pc, CoPc and CuPc anchored on TiO₂ or WO₃ are much more effective catalysts for the oxidation of Na₂S and Na₂S₂O₃ upon irradiation with visible light²⁷. The use of metallophthalocyanine complexes such as iron tetrasulfophthalocyanine as a catalyst has recently been shown effective in the oxidative degradation of persistent pollutants with H₂O₂²⁸.

The band gap energies of materials are related to the photocatalytic activity for the degradation of pollutants. The larger the band gap energy of a material is, the greater the redox potential of the photogenerated electron – hole pairs. Thus, these exhibit more redox capacity. The major challenge in heterogeneous photocatalysis is the need to increase the charge separation efficiency of the photocatalyst. Coupled semiconductor photocatalysts exhibit a very high photocatalytic activity for both gas and liquid phase reactions by increasing the charge separation and extending the energy range of photoexcitation^{27,6}. The photoelectrochemical degradation of organic pollutants is an extension of the heterogeneous photocatalytic process, in which the catalyst is placed on an electrode that is controlled potentiostatically. The photogenerated electron- hole pairs are separated by means of the externally applied electric field¹³¹.

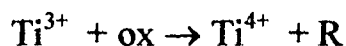
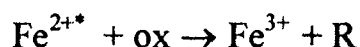
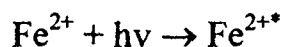
Naphthol Blue Black is a complex textile diazo dye which has a high photo and thermal stability. Conventional methods of oxidative degradation do not effectively degrade these dyes. Investigation of the visible light induced degradation of NBB dye has been carried out using colloidal suspensions of TiO₂ semiconductor nanoparticles¹³². It was assumed that most likely the chromotop 2B and chromotrope 2R were

the reaction intermediates and a quinone was the final product. Mechanism for NBB dye degradation was given by K. Vinodgopal et al¹³³ and others^{134,135}. J. Luo et al¹³⁶ investigated the photoelectrochemical degradation of NBB dye on WO₃ film electrode. Colourless degradation products indicate complete mineralization of the dye. The intermediates of the NBB dye degradation were detected using HPLC analysis and possible mechanism for dye degradation was proposed¹³⁷. By irradiating the composite slurry in the near UV area using Zr supported Ti-substituted Keggin type polyoxometalates indicated the degraded product as CO₂, NH₄⁺, NO₃⁻ and SO₄²⁻ ions¹³⁸.

2.10.6 Mechanism

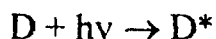
In a semiconductor when a photon with energy of UV matches or exceeds its bandgap energy, E_g , an electron is promoted from the valence band into the conduction band leaving a hole behind. Excited state conduction band electron and valence band hole can recombine and dissipate the input energy as heat. Thus, if suitable electron and hole scavengers are available to trap the electron or hole, recombination is suppressed and the photoactivity of the semiconductor catalyst is enhanced⁴³. According to Cordischi et al²⁸ the main steps of a

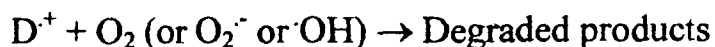
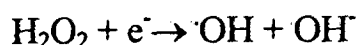
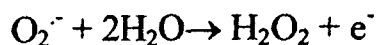
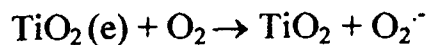
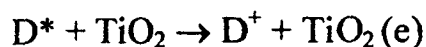
photocatalytic reaction are: (a) photogeneration of hole and electron pairs which must be trapped to avoid recombination (b) reduction and oxidation reactions by the separated electrons and holes with suitable adsorbed species. (c) evolution of intermediates, desorption of products and reconstruction of the surface. According to them Fe^{3+} ions in Fe_2O_3 - TiO_2 system act as electron traps and also play a role in the charge transfer mechanism via a cooperative effect with the $\text{Ti}^{4+}/\text{Ti}^{3+}$ couple.



In a slurry based photoreactor system, the rate determining step in the degradation process is considered to be the reduction of Oxygen by the trapped electron on the semiconductor surface to produce reduced oxygen species such as superoxide radical ion O_2^- or H_2O_2 ¹³.

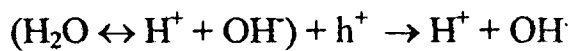
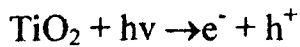
According to Hasnat M. A. et al¹⁴⁰ organic pollutants like dyestuffs have the ability to absorb visible light. The visible light mechanism suggests that the light excite the dyestuff¹⁴



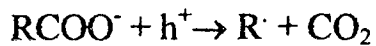


The excited dye (D^*) injects an electron to the conduction band of TiO_2 where it is scavenged by O_2 to form active oxygen radicals. These active radicals drive the photodegradation or mineralization of organic compounds. TiO_2 absorbs light ($\lambda < 400 \text{ nm}$) to generate e^-/h^+ pair. The injected photosensitized e^- generate radicals ($\text{O}_2^{\cdot -}$, $\cdot\text{OH}$) followed by degradation of dyestuff in the system. In this process degradation is faster than that of visible light. TiO_2 assisted photodegradation of malachite green (MG) under both UV and visible light is faster in UV light ($\lambda 320 \text{ nm}$) and follow Langmuir-Hinshelwood model.

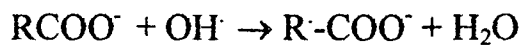
The photocatalytic degradation of malic acid under UV light using TiO_2 was studied by Herrmann J. M. et al¹⁰¹ which show first order kinetic and follow Langmuir- Hinshelwood mechanism. They indicated that the oxidation or photodegradation may involve two oxidizing agents photoproduced holes h^+ and OH^- radicals.



Holes can directly oxidize MA



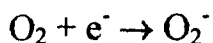
And OH[·] radicals are prone to abstract a H atom



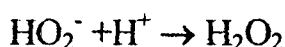
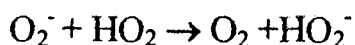
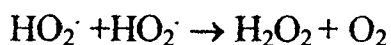
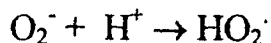
The radicals thus formed will add O₂ and finally give rise to the products.

The photocatalytic degradation of Reactive Yellow 17 (RY17) dye has been investigated by B. Neppolian et al¹⁴² in aqueous heterogeneous solution containing TiO₂ as photocatalyst. The formation of CO₂, SO₄²⁻, NO₃⁻ and NH₄⁺ was identified which was analyzed by HPLC analysis at various irradiation time. The CO₂ generated during the photocatalytic degradation is the evidence for the total destruction of organic compounds in water. As irradiation time increases, the dye degrades to components of lower molecular weights and the intermediates gradually disappear during the remaining time of irradiation. Complete mineralization of the dye is accomplished during an irradiation time of 4 hours.

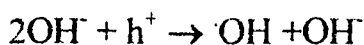
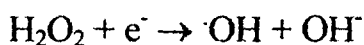
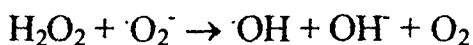
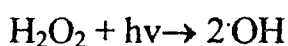
Oxygen adsorbed on the surface of TiO₂ prevents the recombination process by trapping electrons according to the reaction,



The enhancement of photocatalytic degradation of the dye is due to the formation of H_2O_2 according to the following reactions

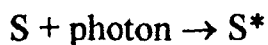


The reactive species (OH radicals) responsible for photocatalytic oxidation can be formed from H_2O_2 according to following reactions

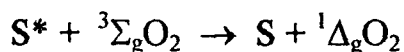


I) Singlet oxygen photochemistry

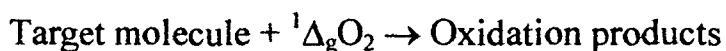
The overall reaction is an oxidation of the organic compound with dissolved O_2 as the oxidizing agent. The first step is absorption of a photon by the photosensitizer (dye) to reach an excited state¹⁴³⁻¹⁴⁵.



The excited sensitizer molecule is able to transfer its energy to a dissolved oxygen molecule to change it from the ground state ($^3\Sigma_g O_2$) to the first excited state ($^1\Delta_g$) which has a higher energy by 22.5 Kcal mole⁻¹ and a lifetime of 1 to 10 m sec in water.



The singlet O_2 ; ($^1\Delta_g$) then is the oxidizing agent,



II) Fenton reaction

This system is based on the capture of a photon by a ferric-hydroxyl with its conversion to a ferrous ion plus a hydroxyl radical¹⁴³. This reaction can be energized by photons from the ultra-violet into the violet and blue. The ferrous ion can be oxidized by molecular O_2 to restore the original ferric complex.



Two $OH\cdot$ radicals are generated for each H_2O_2 and for each photon absorbed. Two H_2O_2 are needed to oxidize one C atom to CO_2 .

CHAPTER 3

EXPERIMENTAL TECHNIQUES

EXPERIMENTAL TECHNIQUES

Ceria based materials are found to have catalytic activity, structural and electronic promoters of heterogeneous catalytic reactions and oxide ion conducting solid electrolytes in electrochemical cells^{52, 60}.

By using co-precipitation procedure, it is possible to achieve a high degree of homogenization together with a small particle size and thereby speed up the reaction rate.

Reactants are dissolved in water, the solutions then being mixed, co-precipitated and the resulting fine powder is a solid solution. The precipitated solids are filtered off and calcined in the usual way, but because of the high degree of homogenization, much lower reaction temperatures are sufficient for reaction to occur.

3.1.A Preparation of Cerium and Tin Oxide doped compounds:

The mixed oxide compositions (a) $Ce_{1-x}Sn_xO_2$ (b) $Ce_{1-x}Fe_xO_2$ (c) $Ce_{1-x}Mn_xO_2$ and (d) $Sn_{1-x}Mn_xO_2$ (where $x = 0, 0.1, 0.2, 0.3, \text{ and } 1$) were prepared by co-precipitation method, a stepwise process is shown in the flow diagram fig. 3.1. The required amount of metal salt of AR grade was

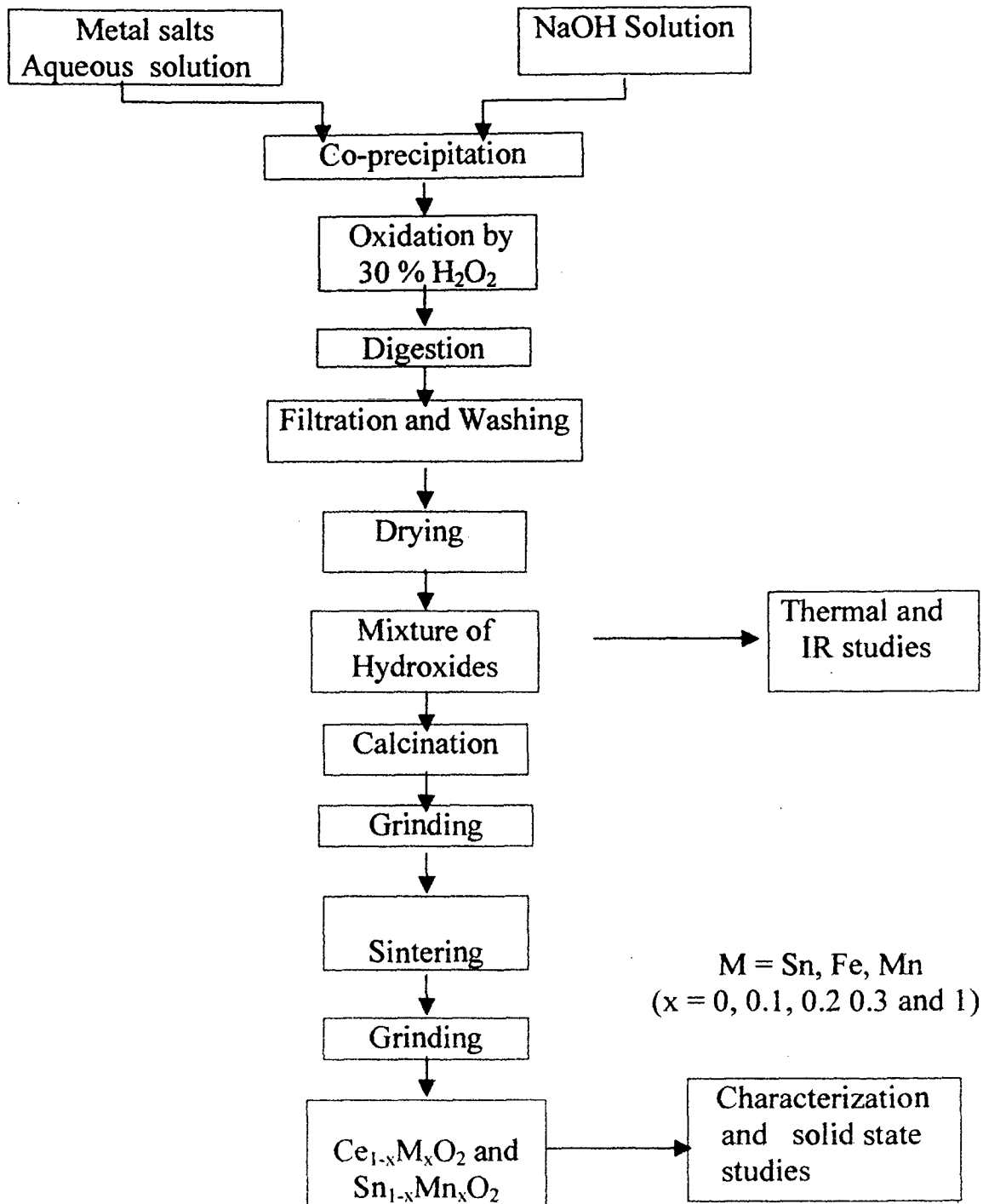


Fig.3.1 Flow diagram of Co-precipitation method

dissolved in distilled water and ceric ammonium sulphate was taken in stoichiometric ratio and dissolved in dilute sulphuric acid solution to obtain a clear homogenous solution. Both the solutions were mixed with continuous stirring. 10% sodium hydroxide solution was prepared by dissolving NaOH (AR grade) in distilled water to obtain an approximately equi-molar concentration solution. This was slowly added to the metal solution with constant stirring till the precipitation is complete. The pH of the solution was maintained between 9-10. The resultant precipitate was digested on a water bath for 3 hours. It was then cooled to room temperature and subjected to oxidation by dropwise addition of 30% H₂O₂ with continuous stirring. The precipitate was then filtered, washed and dried at 100⁰C. The solid was then heated at 400⁰C for 4 hours. The calcined material was homogenized well in a mortar and then fired in a furnace at 600-800⁰C for 10-12 hours. The fired material was homogenized well in a mortar and after characterization used as photocatalyst for further study.

3.1.B Phthalocyanine preparation:

Metal phthalocyanines (MPc) (where M = Cu, Ni, Co and Fe) were prepared by method described elsewhere²⁹. Required amount of phthalic anhydride, urea, metal salt and ammonium molybdate were

suspended in nitrobenzene and heated, at 190°C. After 4-5 hours the mixture was filtered hot and then washed with nitrobenzene, followed by methanol. The crude product was boiled 2 hours, first with 1N HCl and then with 1N NaOH, filtered and washed with water each time until the filtrate was neutral. The solid material was then stirred in methanol, suction filtered, and dried at 60°C.

3.2 Characterization

The mixed oxides prepared by co-precipitation method and the phthalocyanines prepared by literature method were characterized by X-ray diffraction technique, vibrational spectroscopy, B.E.T. liquid nitrogen adsorption method and thermal studies.

3.2.1 The X-ray powder diffraction technique

The prepared samples were characterized by recording X-ray powder diffractograms. The diffraction patterns were recorded on ITAL X-ray diffractometer using Cu K α radiation, filtered through Ni absorber, at a scanning rate of 0.1°/min. The samples were identified by comparing the observed inter planar d-spacings and relative peak intensities, with those reported in the literature (ICDD-PDF data files). The intermediate compositions, which are not reported, were confirmed by comparing with the end compositions.

3.2.2 Vibrational spectroscopy (IR spectroscopy)

The infra red absorption spectra were recorded for all the compositions in the range $4000-400\text{ cm}^{-1}$, on a Shimadzu FTIR instrument, model 8101 A, using KBr as a carrier. The mixture of sample and KBr was pressed into a pellet with thickness of about 1 mm. The spectra were compared with the literature and interpreted.

3.2.3 Atomic absorption spectroscopy

The sodium contamination in the oxides prepared by co-precipitation technique using NaOH, was found out using an atomic absorption spectrometer. Approximately 250 mg of powdered sample was dissolved using 25 ml of pure HCl it was then further diluted to the required concentration. The total amount of sodium was determined by comparing with the standard.

3.2.4 B. E. T. method (Surface area measurement)

Surface areas of the prepared samples under study were measured using BET nitrogen adsorption method on SMARTSORB 91. Specific surface areas of the catalyst were calculated with the help of well -known Brunauer, Emmet and Teller (BET) expression.

$$P/V (P_0 - P) = 1/V_m C + (C - 1)/V_m C \times P/P_0 \dots\dots\dots (1)$$

Where 'P' is the equilibrium pressure. 'P₀' is the saturated vapour pressure of the gas at the temperature of the adsorption. 'V' is the volume of the adsorbed gas at S.T.P., 'C' is the constant related to the heat of adsorption and 'V_m' is the volume of the gas at S.T.P. required to form a monolayer. Various quantities from the above equation like P, P₀ and V could be determined experimentally. V_m and C can be obtained by plotting P/V (P₀-P) versus P/P₀. Plot should give a straight line with slope (S) = C-1/V_mC and intercept (I) = 1/V_mC which proves the validity of the equation (1).

It can be shown from equation (1) that $V_m = 1/S+I$ and $C = S/I+1$. Since V_m is the volume of the gas at 0°C and 1 atmospheric pressure necessary to cover the surface with one layer of the gas, it is easy to convert it to the no of molecules involved. Assuming 16.2⁰A as the value of the cross sectional area of single nitrogen molecule at liquid temperature Brunauer, Emmet and Teller have shown that,

$$\text{Surface area} = 4.38 V_m (\text{C.C., S.T.P.}) \text{ m}^2/\text{g} \text{ - - - - - (2)}$$

Surface area for various oxide samples were observed in the range of 2.6 to 46 m²/g.

3.3 Electrical resistivity measurements

The electrical resistivity measurements were carried out to study the conductivity behaviour of the samples and possible relationship with catalysis.

Electrical resistivity measurements were carried out using a two-probe conductivity cell in the temperature range from room temperature to 250°C. For the resistivity measurement, sample was pelletized using an approximately 1-2 g of the sample, under a pressure of 7,500 Kg/cm³. The prepared pellets were subjected to the heat treatment in an electrical furnace at 600-800°C for 10 –12 hours. Metal phthalocyanines were pelletized and heated at 200°C for 24 hours. Silver paint was applied on both the surfaces of the pellet. The pellet was tightly held between two polished and cleaned silver electrodes by adjustable type assembly and the resistivity measurements were carried out from room temperature to 250°C, point- by -point measurement. Measurements were recorded while cooling the pellet.

3.4 Magnetic Susceptibility Measurements:

The magnetic susceptibility ' χ_g ' in air of the samples was determined by Gouy's method at room temperature. A field of the order of 8,000 Gauss was employed. A sensitive analytical balance of DONA was used to measure the difference in weights. Mercury tetra thiocyanatocobaltate {Hg[Co(SCN)₄]}

was used as the standard material. The sample tube was washed, dried and filled with the standard material up to a certain mark and hanged between the electromagnets of the Gouy balance.

The weight was recorded before and after applying the appropriate magnetic field. The procedure was repeated for the sample whose χ_g is to be determined. The magnetic susceptibility of the sample was calculated by using the following calculations.

In the first part, tube constant or β – constant is calculated, as χ_g value of the standard material is known. Using the relation,

$$\beta\text{- Constant} = \chi_g \times W/\Delta W \quad (\chi_g = 16.44 \times 10^{-6} \text{ cgs units for } \{ \text{Hg}[\text{Co}(\text{SCN})_4] \})$$

$$W = (W_3 - W_1) = \text{Wt. of standard material taken}$$

$$\Delta W = \Delta W' + \Delta W'' \quad (+ \text{ ve for paramagnetic and } -\text{ve for diamagnetic})$$

$$\Delta W' = (W_4 - W_3) \text{ and } \Delta W'' = (W_1 - W_2) \text{ where}$$

$$W_1 = \text{Weight of the empty tube,}$$

$$W_2 = \text{Weight of the empty tube with field}$$

$$W_3 = \text{Weight of the tube with standard material and}$$

$$W_4 = \text{Weight of the tube and standard material with field}$$

Hence β - constant was calculated. In the second part, to calculate χ_g of the sample, substitute β - constant in the above relation, gives the magnetic

susceptibility. Further this data is utilized to calculate unpaired electrons present in the sample as follows.

$$\chi_m = \chi_g \times \text{molecular weight of the sample}$$

Where χ_m = molar susceptibility and

$$\chi_g = \text{gram susceptibility}$$

The magnetic moment μ effective (μ_{eff}) of the sample was calculated by using the equation given below.

$$\mu_{\text{eff}} = 2.84 \sqrt{\chi_m \times T} \text{ B. M. where } T = \text{absolute temperature and}$$

μ_{eff} is the magnetic moment

3.5 Saturation magnetization study

The saturation magnetization is studied with the help of hysteresis loop tracer. These measurements were done on selected magnetic samples, using a high field hysteresis loop tracer and the three major components are electromagnet, pick-up coil and integrating circuits.

The loop tracer consists of an electromagnet working at 50 Hz mains frequency. The alternating magnetic field of about 3600 Oersted is produced in an air gap of about 1 cm, in the instrument and a special balancing coil is used to measure the saturation magnetization of the sample in the air gap. Depending upon the magnetic induction in the sample, pick-up coil produce a

field proportional to the magnetic induction of the sample. A supporting coil produces a signal that is equivalent to the strength of the magnetic field. The signal is displayed as a hysteresis loop on the screen of an oscilloscope. A digital AC Voltmeter, which is connected to the output, displays the peak or RMS value of the signal proportional to the saturation magnetization, in millivolts. The calibration of the vertical scale corresponding to the magnetization value is done using Nickel as a standard substance having magnetization of 56 emu/g. The saturation magnetization values, σ_s in emu /g of some selected samples was found out.

3.6 Thermal studies

The thermal technique of Thermogravimetric analysis (TG) and Differential scanning calorimetry (DSC) was carried out using NETZSCH-Geratebau GmbH Thermal Analyzer. TG was used to study the heat effects, associated with the physical and chemical changes of the substances in the temperature range from room temperature to 800⁰C. Thermal effects, exothermic or endothermic preceding physical and chemical changes were studied by differential method in which the sample temperature is continuously compared against the temperature of thermally inert reference material. TG was recorded to study the behaviour of weight loss of the precursor sample.

The samples, in a powdered form and weighing between 5 to 10 mg, were placed in alumina crucible covered with lid. Sample was continuously weighed as it is heated at a constant linear rate of $10^{\circ}\text{C}/\text{min}$.

3.7 Electron Spin Resonance (ESR) study

Electron Spin resonance occur when a spinning electron in an externally applied magnetic field absorbs sufficient electromagnetic radiation to cause the inversion of spin state of the electron, which is also known as electron paramagnetic resonance and as electron magnetic resonance.

ESR study was carried out for the sample containing paramagnetic species. In ESR spectroscopy, a magnetic field strength of 3220 gauss (commonly used field strength = 3300 gauss) was employed. The energy level difference due to electron spin was 6.1×10^{-17} ergs (or about 1.5×10^{-24} calories) and frequency 'V' is 9.2 GC (Giga cycles or 10^9 cycles per sec.), this frequency lies in the microwave region of the electromagnetic radiation spectrum. The ESR spectra were taken at the X- band on a varian E- 112 spectrometer at room temperature. The sample was mounted in a quartz tube and TCNE was used as a field calibrant taking its g-value as 2.00277. Spectroscopic spitting factor (g) or gyro magnetic ratio was obtained from the following relation,

$$\mu = -g \beta s$$

Where ' μ ' is the magnetic moment, and ' β ' is the Bohr magneton (ergs/gauss), ' g ' is the gyro magnetic ratio and ' s ' is the spin of electron $+1/2$ or $-1/2$

3.8 UV- Visible Spectroscopy

The UV-visible absorption spectra were recorded for phthalocyanines in the range 400-700 nm, on a UV- visible spectrophotometer (spectrol19) using pyridine as a solvent. The phthalocyanines were dissolved in pyridine and the solution was scanned from 400 to 700 nm using glass cuvettes, each phthalocyanine showed maximum absorbance at particular wavelength which was compared with the literature.

3.9 UV-Visible diffuse reflectance study

The UV-VIS-DRS spectra were recorded on UV-visible spectrophotometer with BaSO_4 as a reference material. The samples were taken in the form of 2mm thick self supported pellets to measure the reflectance. Samples were scanned from 200 to 700 nm. Band gap energy was calculated at absorption edge shown by each sample in the spectra.

3.10 Photocatalytic Studies

Prepared samples were tested for two model reactions such as photodegradation of textile diazo dye Naphthol Blue Black and basic Yellow Auramine O.

10^{-3} M dye solution was prepared by dissolving the Naphthol Blue Black dye in distilled water and was used as stock solution. From this, 10^{-5} M solution was prepared in a standard volumetric flask and used as test solution. 200 mg of the prepared sample was used for the degradation of the dye that was found to be optimum amount for the degradation. The degradation rate was monitored using UV-visible spectrophotometer (spectro 119) by measuring absorbance of the reaction mixture after every hour. Naphthol Blue Black absorbs at 618 nm.

100 ml of the 10^{-5} M dye solution was aerated with oxygen for 2-5 minutes and to this 200 mg of prepared photocatalyst was added and stirred well. This reaction mixture was kept in sunlight for irradiation. Small amount of reaction mixture was taken out after every hour, filtered with Whatmann no 41 and absorbance was measured at λ_{\max} 618 nm.

The reaction was carried out at various experimental conditions like change in pH, with different amount of photocatalyst and with and without oxygen. The pH of the solution was adjusted by using previously standardized

1N HCl and 1N NaOH. The pH was measured with pH paper. The degradation product was analyzed by HPLC method and qualitative analysis. The dye Naphthol Blue Black degrades to a colourless solution.

Photocatalytic degradation of another textile dye basic Yellow Auoramine O was studied on selected samples. Test solution was prepared with distilled water and used for degradation. 100 mg of the photocatalyst was used and the absorbance of the reaction mixture was measured at wavelength 432 nm by taking out small amount of the solution after every hour. Absorbance versus time was plotted for every sample. The degradation rate was found to increase with time.

CHAPTER 4

SOLID STATE STUDIES

SOLID STATE STUDIES

The various solid state studies such as X-ray powder diffraction, IR spectroscopy, thermal analysis, electrical resistivity, magnetic susceptibility, saturation magnetization and electron spin resonance were under taken. The comparison of different results were made and discussed on the basis of experimental data.

4.1 X-ray diffraction analysis

The formation of monophasic oxides were checked by recording X-ray powder diffractogram of all the samples such as $Ce_{1-x}Sn_xO_2$, $Ce_{1-x}Fe_xO_2$, $Ce_{1-x}Mn_xO_2$ and $Sn_{1-x}Mn_xO_2$ ($x = 0, 0.1, 0.2, 0.3$ and 1.0). The d spacing and intensities corresponding to 2θ value obtained from the diffractograms were compared with the values reported in the literature (ICDD-PDF files) and found to be in good agreement. Since the d spacing of the intermediate compositions was not reported in the literature, the values were compared with the end members of the series. Figures 4.1- 4.4 shows X-ray diffraction pattern of representative samples.

Fig.4.1 shows the XRD pattern of $Ce_{1-x}Sn_xO_2$ ($x = 0, 0.1, 0.2$ and 0.3) oxides calcined at $600^\circ C$. Pure CeO_2 is in cubic phase and SnO_2 is in tetragonal

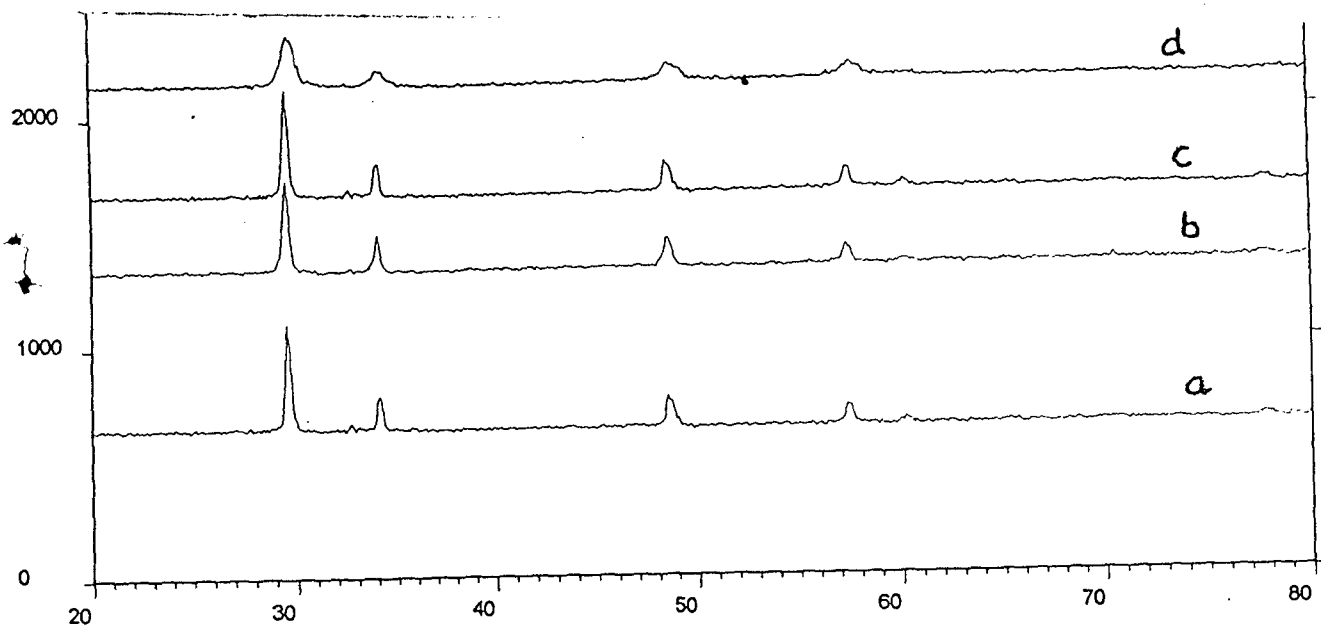


Figure 4.1 XRD pattern of $Ce_{1-x}Sn_xO_2$ a) CeO_2 b) $Ce_{0.9}Sn_{0.1}O_2$ c) $Ce_{0.8}Sn_{0.2}O_2$ d) $Ce_{0.7}Sn_{0.3}O_2$

phase. $\text{Ce}_{0.9}\text{Sn}_{0.1}\text{O}_2$, $\text{Ce}_{0.8}\text{Sn}_{0.2}\text{O}_2$ and $\text{Ce}_{0.7}\text{Sn}_{0.3}\text{O}_2$ are in cubic phases and the crystal lattice parameter (5.3857°A) is smaller than that of calculated pure CeO_2 (5.4189°A). It may be due to the insertion of Sn atom into the CeO_2 crystal lattice and since the radius of Sn^{4+} (0.81°A) ion is smaller than that of the Ce^{4+} (0.97°A), it reduces CeO_2 crystal lattice parameter. On increasing x above 0.3, the XRD diffraction peaks due to CeO_2 become weak and SnO_2 phases are observed. Therefore only small amounts of SnO_2 can be introduced into the CeO_2 lattice to form solid solution and excess SnO_2 remains in a tetragonal phase. The results are in agreement with the literature values^{21,56,72}. All the X-ray diffraction peaks have been shifted gradually to higher 2θ values with the increase in Sn content in the solid solution which is attributed to the insertion of Sn ions of smaller size into the cubic lattice of CeO_2 resulting in the contraction of its cell parameter. The XRD pattern of $\text{Ce}_{0.9}\text{Fe}_{0.1}\text{O}_2$ oxide sintered at 800°C show similar results. Fe_2O_3 has α -hexagonal structure and $\text{Ce}_{0.9}\text{Fe}_{0.1}\text{O}_2$ is in cubic phase with lattice parameter smaller than that of pure CeO_2 . The radius of Fe^{3+} (0.64°A) ion is smaller than the Ce^{4+} (0.97°A) ion.

The XRD pattern of $\text{Ce}_{1-x}\text{Mn}_x\text{O}_2$ ($x = 0, 0.1, 0.2$ and 0.3) is shown in Fig.4.2. The XRD lines of solid solution $\text{Ce}_{0.9}\text{Mn}_{0.1}\text{O}_2$, $\text{Ce}_{0.8}\text{Mn}_{0.2}\text{O}_2$ and $\text{Ce}_{0.7}\text{Mn}_{0.3}\text{O}_2$ are similar to those of CeO_2 indicating the stabilization of the fluorite structure with Mn substitution. On increasing x , diffraction peaks of

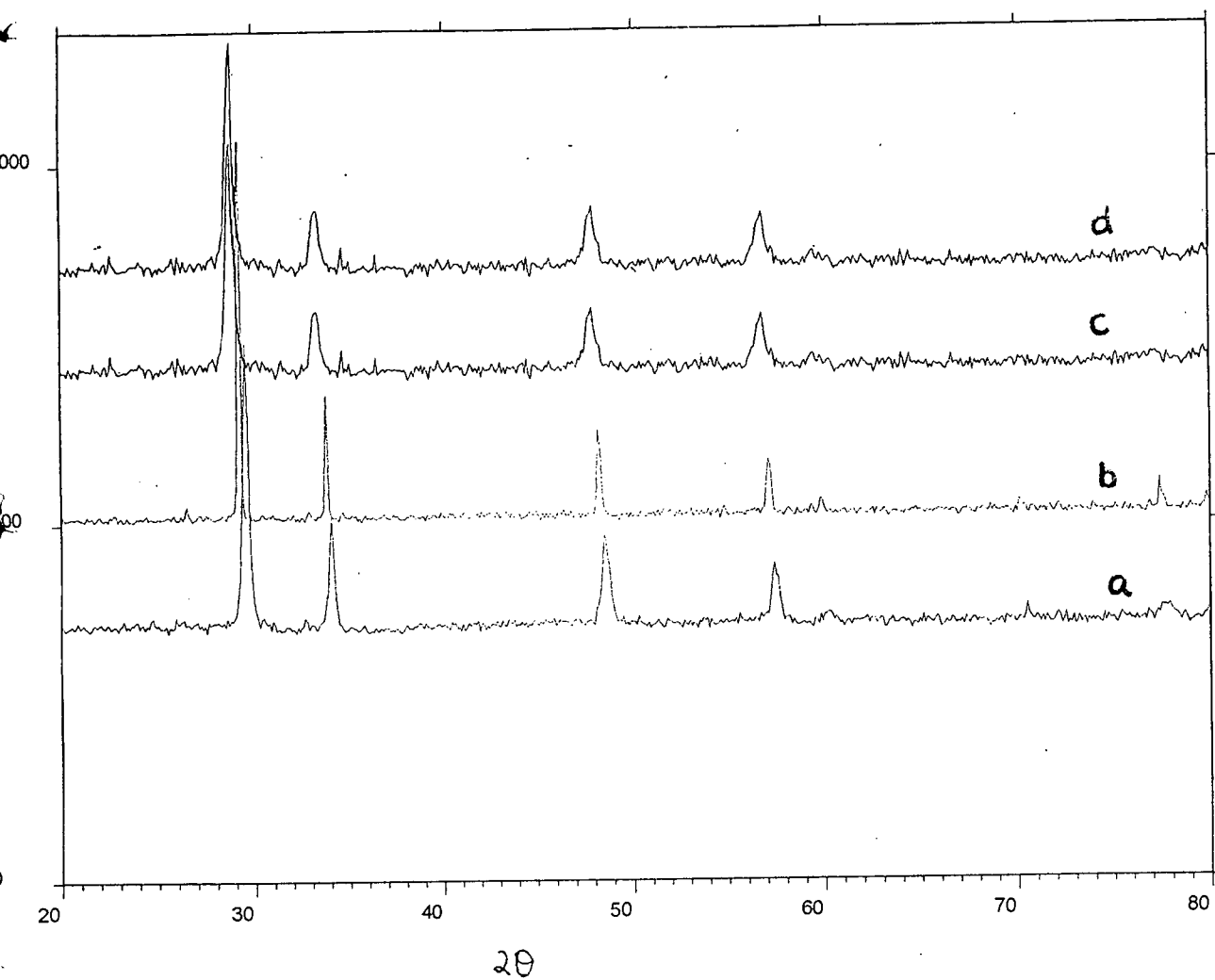


Fig. 4.2 XRD pattern of $\text{Ce}_{1-x}\text{Mn}_x\text{O}_2$ a) CeO_2 b) $\text{Ce}_{0.9}\text{Mn}_{0.1}\text{O}_2$
c) $\text{Ce}_{0.8}\text{Mn}_{0.2}\text{O}_2$ d) $\text{Ce}_{0.7}\text{Mn}_{0.3}\text{O}_2$

MnO₂ along with CeO₂ peaks can be seen. All the X-ray diffraction peaks have been shifted gradually to lower 2θ values with the increase in Mn content in the solid solution which is ascribed to the insertion of Mn ions of slightly bigger size into the cubic lattice of CeO₂ resulting in the expansion of its cell parameter. Accordingly the lattice parameter increases linearly from 5.41°Å to 5.57°Å with increase in Mn content.

Fig.4.3 indicates the XRD pattern of Sn_{0.9}Mn_{0.1}O₂. Pure SnO₂ is in tetragonal phase⁷⁴. The solid solution of Sn_{0.9}Mn_{0.1}O₂, Sn_{0.8}Mn_{0.2}O₂ and Sn_{0.7}Mn_{0.3}O₂ show XRD peaks similar to those of SnO₂ indicating the tetragonal structure. The crystal lattice parameter increases as the Mn content increases due to expansion of the cell parameter. Shift of the CeO₂ pattern towards the lower 2θ values indicates the possible formation of a solid solution¹⁴⁶.

Fig.4.4 gives X-ray pattern of Copper phthalocyanine. The phthalocyanine compounds exist in different polymorphic forms, the common are α, β and γ- phases and the β form is thermodynamically more stable. The phthalocyanine molecule is a square planar molecule consisting of a divalent metal ion surrounded by four benzopyrrole units. The structure of CuPc is adjudged to be tetragonal with six molecules per unit cell which is in agreement with Robinson and Klein¹⁴⁷. Well defined diffraction peak in the

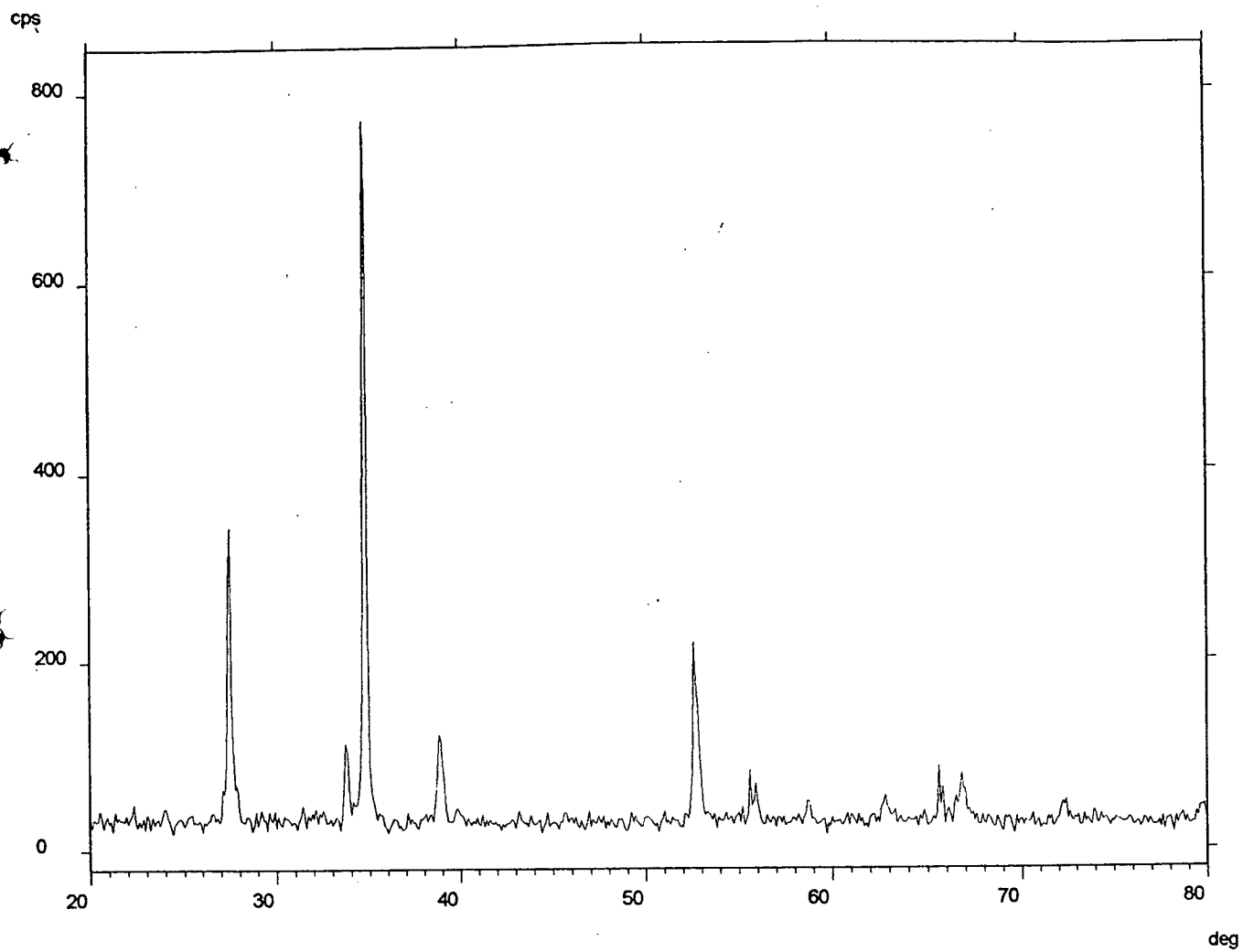


Fig. 4.3 XRD pattern of $\text{Sn}_{0.9}\text{Mn}_{0.1}\text{O}_2$

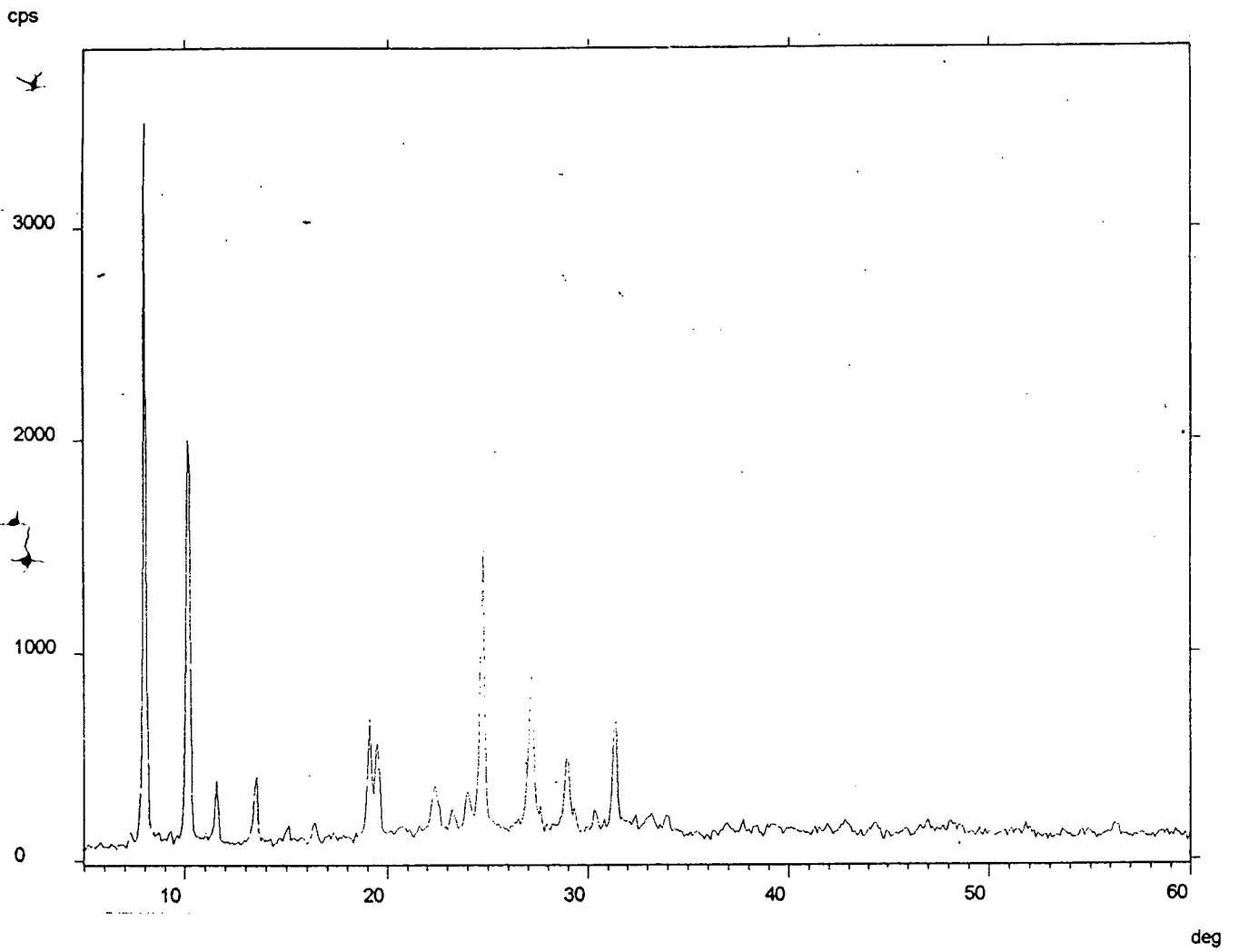


Fig. 4.4 XRD pattern of Copper phthalocyanine

(001) direction gives the direction of the preferential orientation. The lattice parameter are obtained as $a = b = 16.68^{\circ}\text{A}$ and $c = 11.8^{\circ}\text{A}$. Indexing is carried out by comparing the International Centre for Diffraction Data- Powder Diffraction File(ICDD-PDF). The differences in the d values are attributed to higher X-ray absorption, sample purity, particle size, preferred orientation and crystal texture¹⁴⁷. Similar observations were made regarding CoPc, FePc and NiPc. They are having stable β - phase.

4.2 Infra-red spectroscopy

The oxides are characterized by metal-oxygen bonding present in the region from $1000\text{cm}^{-1} - 400\text{cm}^{-1}$. In the IR spectra of doped compounds, the evolution of new bands can be observed with metal substitution as shown in fig. 4.5- 4.9. The frequency of these bands has been related to the strength of metal – oxygen covalency.

In fig. 4.5 in the IR spectra of $\text{Ce}_{1-x}\text{Sn}_x\text{O}_2$ ($x = 0, 0.1, 0.3$ and 1.0) samples it is observed that as the substitution of Sn^{4+} in CeO_2 increases, the absorption peak observed at 852 cm^{-1} gets reduced and there is appearance of peaks at 620 and 670 cm^{-1} which are due to Sn-O vibrational modes. These bands are prominent in SnO_2 and at slightly lower wave number value at 680 and 610 cm^{-1} which is in agreement with the literature³⁹. This suggests the

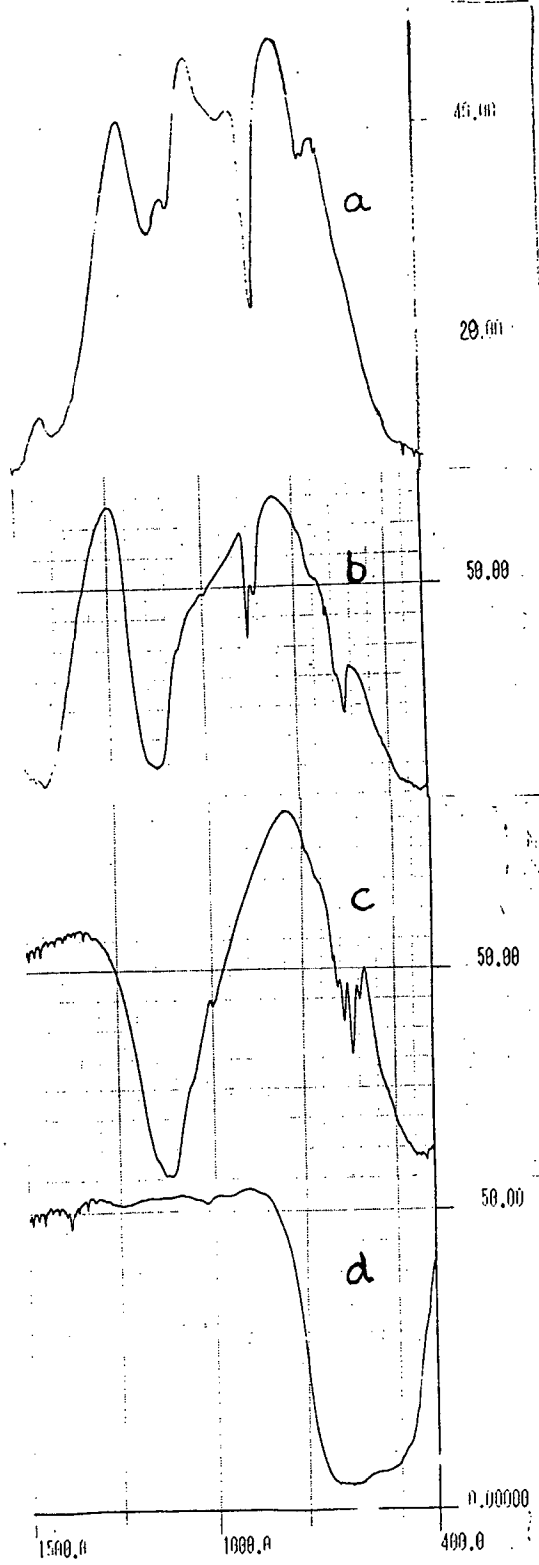


Fig. 4.5 IR spectra of $Ce_{1-x}Sn_xO_2$ a) CeO_2 b) $Ce_{0.9}Sn_{0.1}O_2$
 c) $Ce_{0.7}Sn_{0.3}O_2$ d) SnO_2

substitution of Ce^{4+} by Sn^{4+} ions in all the samples. Also there are two small peaks observed at 420 and 450 cm^{-1} of CeO_2 stretching vibration in agreement with literature⁶⁴.

In fig. 4.6 in $\text{Ce}_{1-x}\text{Fe}_x\text{O}_2$ samples, for $x = 0.3$ two sharp absorption peaks at 600 and 652 cm^{-1} are seen. Also peak at 852 cm^{-1} is reduced which is of Ce-O stretching vibrational mode. The two bands are shifted at 546 and 450 cm^{-1} and they are sharp and of strong intensity in $\alpha\text{-Fe}_2\text{O}_3$ ¹⁴⁹.

Fig. 4.7 shows the IR spectra of $\text{Ce}_{1-x}\text{Mn}_x\text{O}_2$ series. It is observed that as the x increases the Ce-O band at 852 cm^{-1} gets reduced and there are appearance of bands at 510 and 580 cm^{-1} due to Mn-O vibrations. These bands are of strong intensity in $\text{Ce}_{0.7}\text{Mn}_{0.3}\text{O}_2$ than MnO_2 . Fig. 4.8 shows the IR spectra of $\text{Sn}_{1-x}\text{Mn}_x\text{O}_2$ samples. Evolution of Mn-O band at 510 cm^{-1} can be seen with the increase of x in $\text{Sn}_{1-x}\text{Mn}_x\text{O}_2$ composition. The absorption peak at 680 cm^{-1} disappears gradually, showing substitution of Sn^{4+} by Mn^{4+} ions.

Phthalocyanines are characterized by IR Spectroscopy^{82,108,111-112}. IR spectra of metal phthalocyanines are shown in fig. 4.9. IR spectra show following absorption peaks. The peaks around 1121-1123, 1090 -1092, 1067-1070, 947- 949, 872- 885 and 754 cm^{-1} are due to phthalocyanine skeletal vibrations. The peaks observed at 1420 – 1423 and 1335 cm^{-1} is due to aromatic phenyl ring. The peaks around 1286, 1226 and 1202 -1210 cm^{-1} are

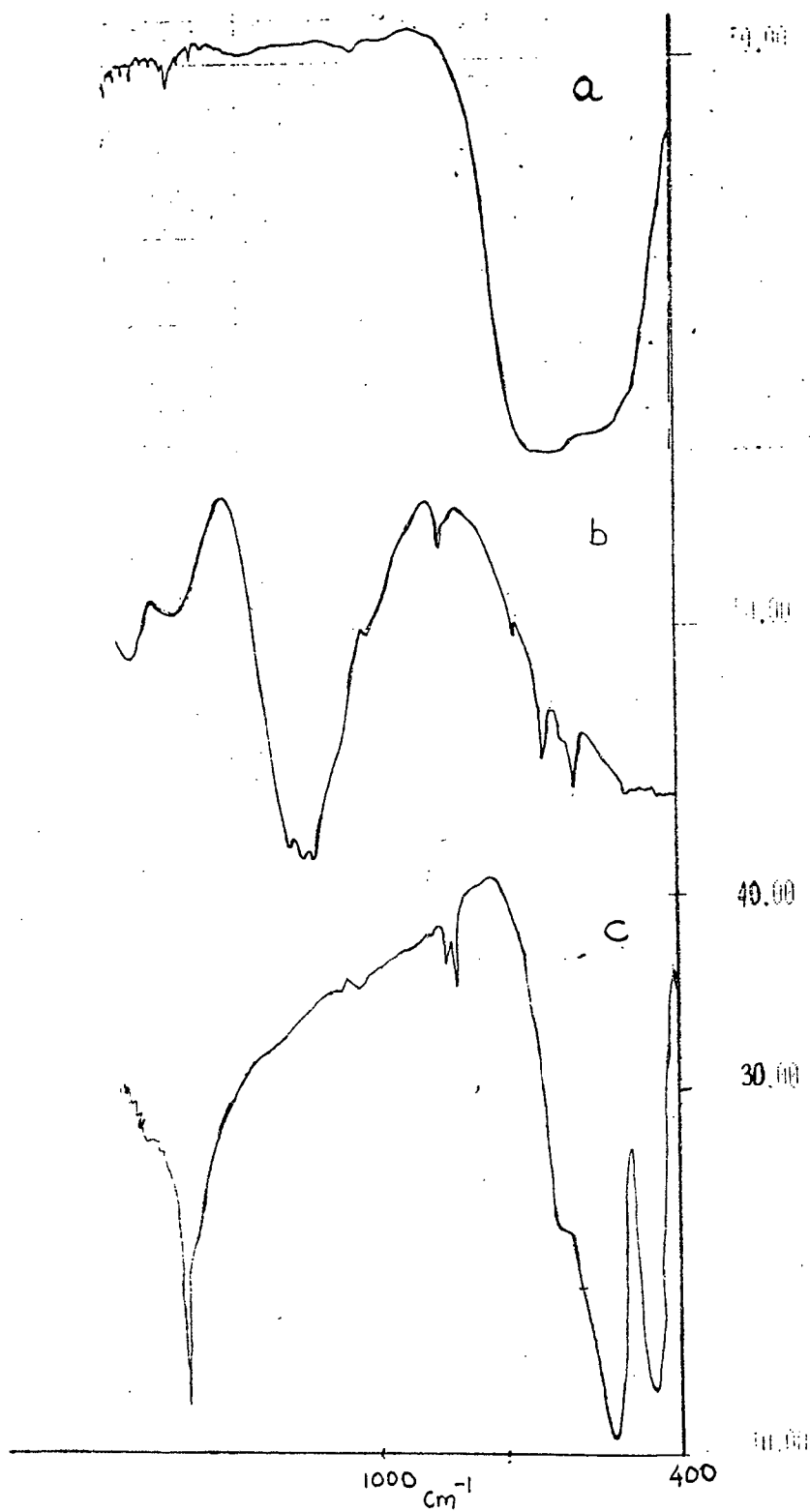


Fig. 4.6 IR spectra of $Ce_{1-x}Fe_xO_2$ a) SnO_2 SnO_2
 b) $Ce_{0.7}Fe_{0.3}O_2$ c) $\alpha-Fe_2O_3$

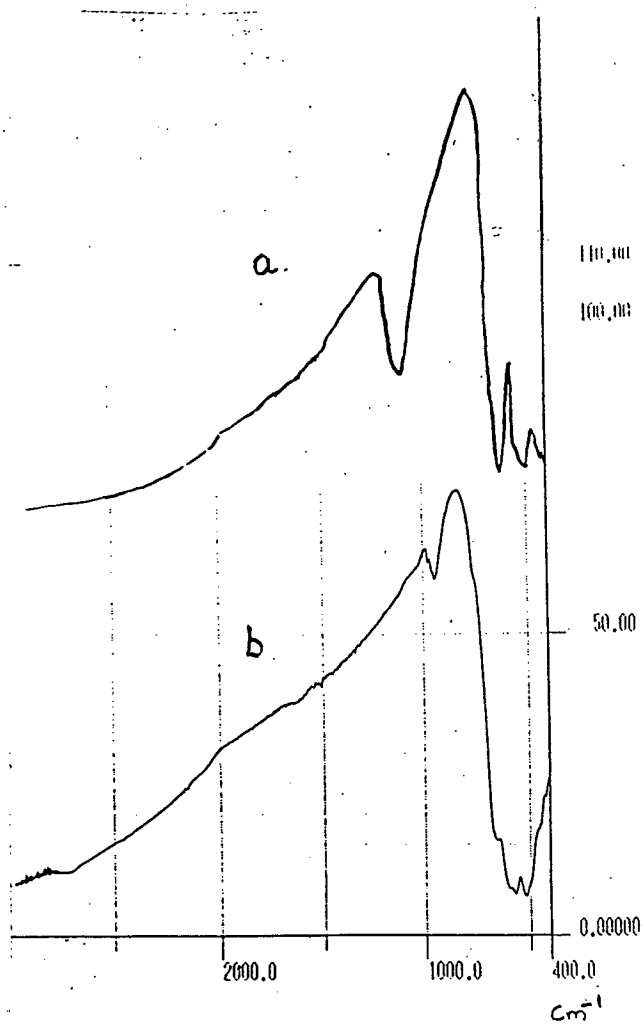


Fig. 4.7 IR spectra of $\text{Ce}_{1-x}\text{Mn}_x\text{O}_2$ a) $\text{Ce}_{0.7}\text{Mn}_{0.3}\text{O}_2$ b) MnO_2

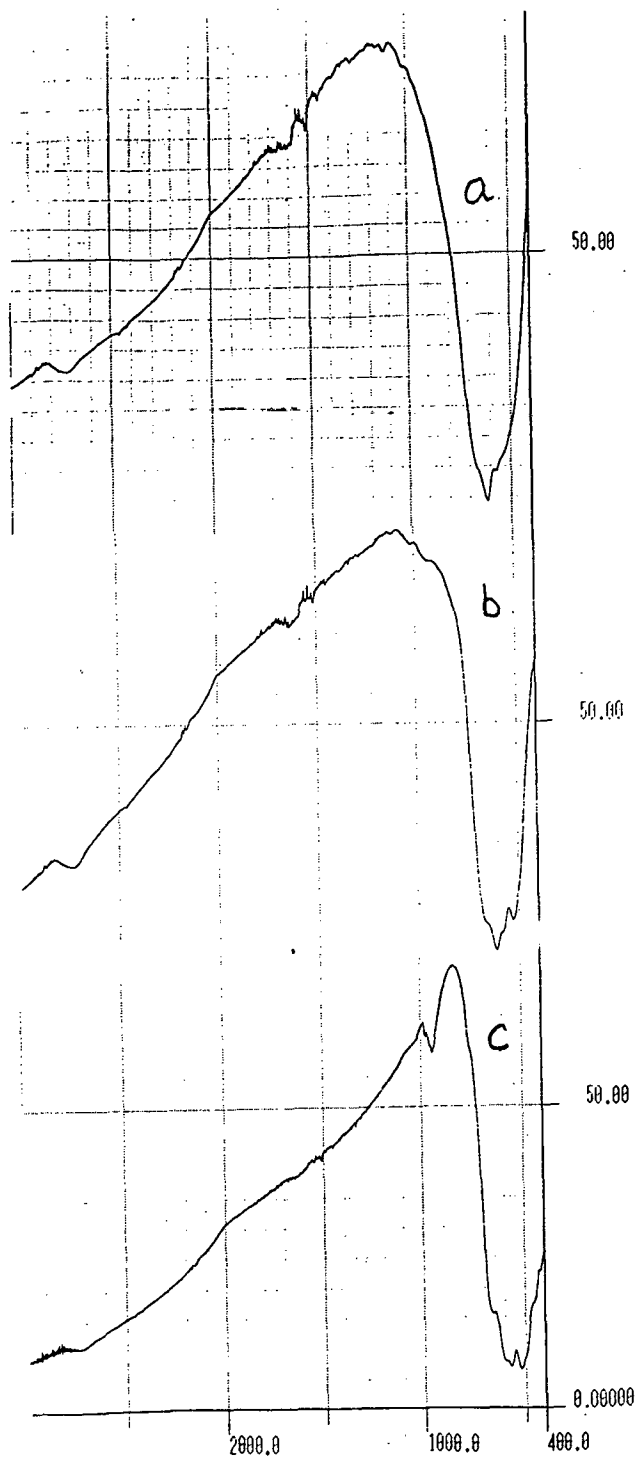


Fig. 4.8 IR spectra of $\text{Sn}_{1-x}\text{Mn}_x\text{O}_2$ a) $\text{Sn}_{0.8}\text{Mn}_{0.2}\text{O}_2$
 b) $\text{Sn}_{0.7}\text{Mn}_{0.3}\text{O}_2$ c) MnO_2

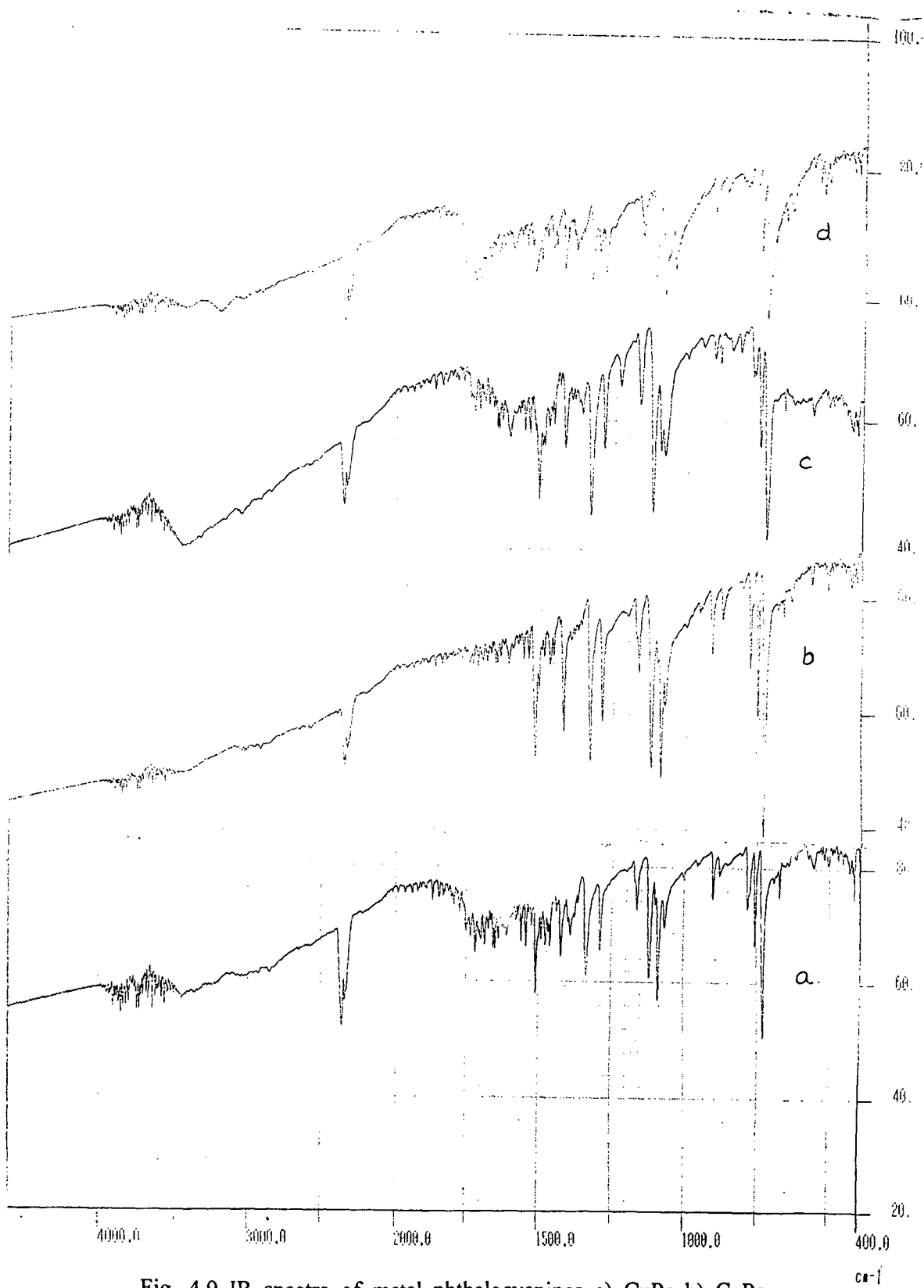


Fig. 4.9 IR spectra of metal phthalocyanines a) CuPc b) CoPc
c) FePc d) NiPc

due to C-N stretch. The peaks assigned to C-H in plane bending around 1165-67, 1001-1005 cm^{-1} and peaks due to C-N bending at 901 cm^{-1} and 799 - 802 cm^{-1} respectively. The peaks at 770 - 773 cm^{-1} are due to C-H out of plane bending. Broad peak at 3400 -3415 cm^{-1} is attributed to the hydrogen bonding formed between the nitrogen atom of the Pc macromolecule and H atom of the moisture absorbed on the KBr pellets¹⁰⁸. The sharp peaks observed at 1610 - 1616 cm^{-1} are attributed to C = C, C = N and ring stretching (skeletal band).

4.3 Thermal Analysis

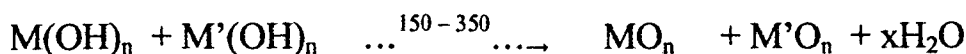
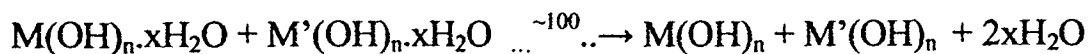
Co-precipitated hydroxide precursors before decomposition were subjected to thermal analysis studies, to find out the decomposition temperature of hydroxides and then the initiation of solid- state diffusion reaction. Metal phthalocyanines were subjected to thermal treatment to check the thermal stability of the phthalocyanines. TG/DSC pattern of representative samples are shown in figures 4.10 – 4.13.

Thermo-gravimetric studies show three major steps in the decomposition process and the probable reactions are

1. Dehydration
2. Decomposition of hydroxides to corresponding oxides and followed by

3. Solid-state diffusion reaction leading to solid solution formation in mixed oxides.

The reactions taking place during heating in the case of mixed oxides may be represented by following steps:



Where M and M' are metal ions and n indicate the number depending on oxidation state of the metal.

Figure 4.10 show TG/DSC pattern of cerium tin co-precipitated hydroxide decomposition. First weight loss is around 100°C for the elimination of water. Further weight loss is around 150-350°C due to decomposition of hydroxide and on further heating leads to the solid solution. There are two endothermic DSC peaks at 92 and 308°C respectively corresponding to two weight losses. These results are in accordance with literature¹⁵⁰. Since solid - state diffusion being slow process and takes place over a range of temperatures, no sharp change in thermal event is observed.

Fig. 4.11 shows a weight loss for $Ce_{0.9}Fe_{0.1}(OH)_4$ precursor decomposition between 90-120°C due to the loss of moisture and further weight loss between 250-300°C due to decomposition of hydroxides and

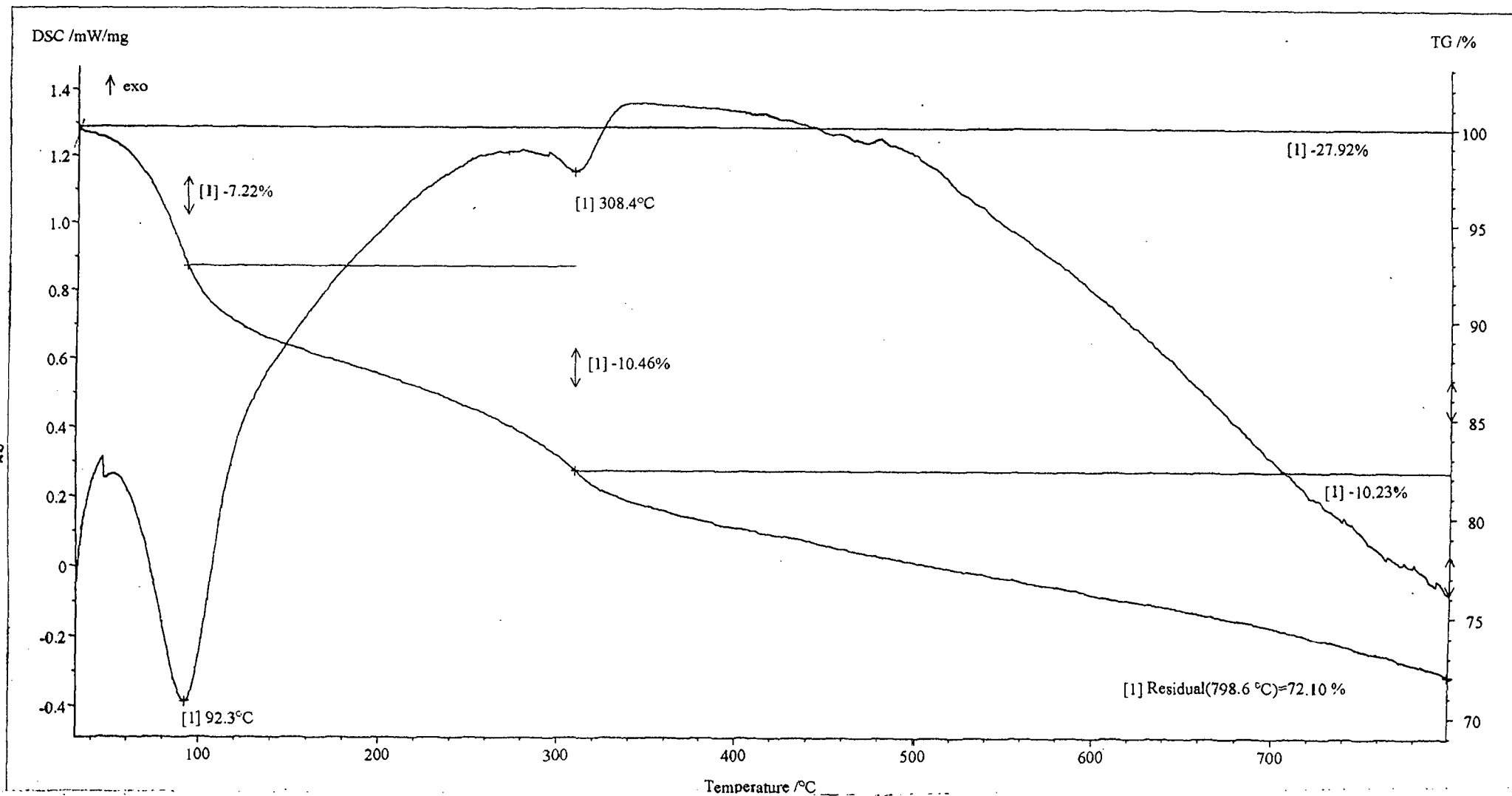


Fig. 4.10 TG/DSC pattern of $Ce_{0.8}Sn_{0.2}(OH)_n \cdot xH_2O$ precursor decomposition

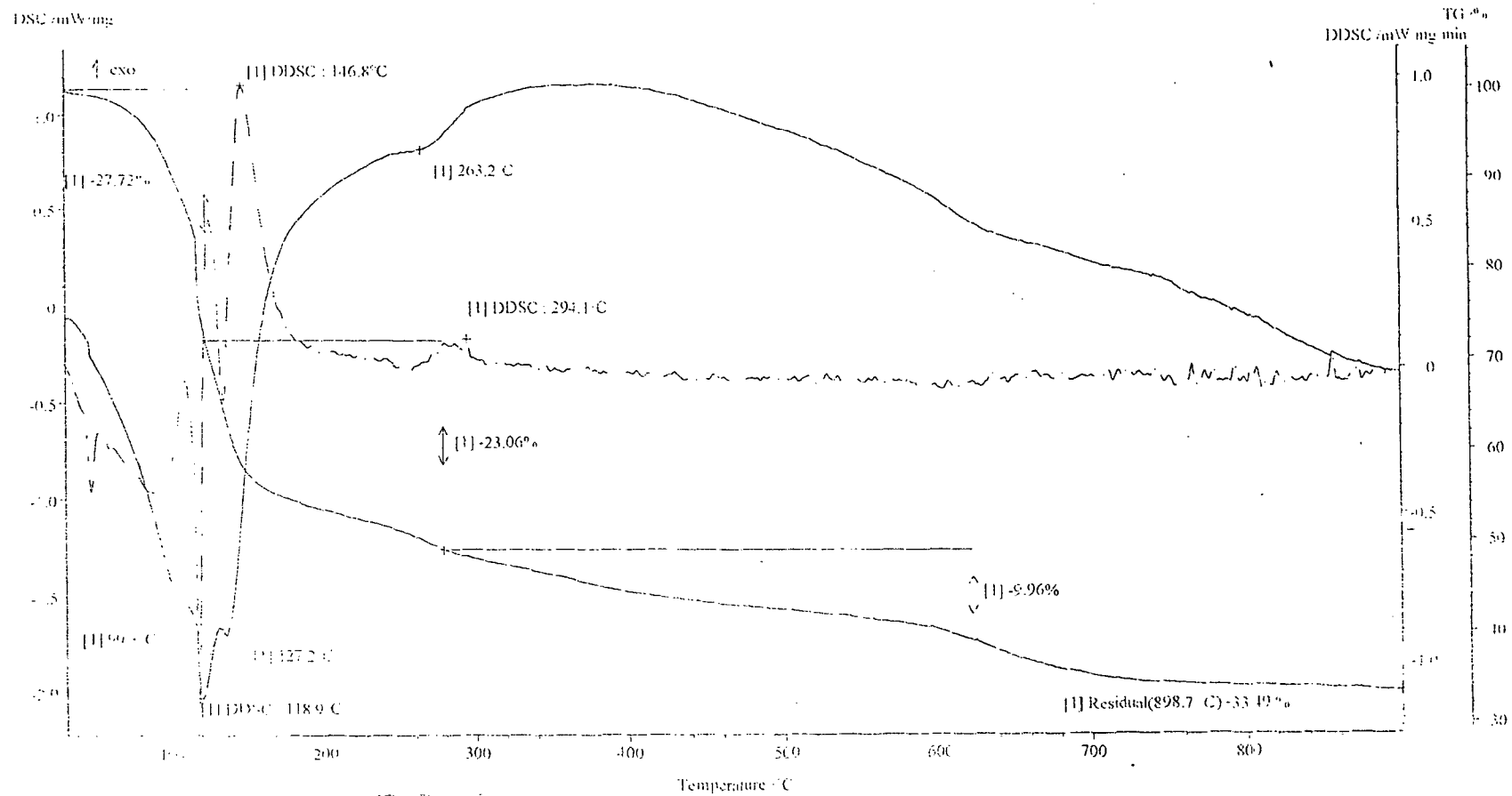


Fig. 4.11 TG/DSC pattern of $Ce_{0.9}Fe_{0.1}(OH)_n \cdot xH_2O$ precursor decomposition

94

initiation of solid state diffusion leading to oxide formation. Two endothermic DSC peaks are observed at 118°C and 263°C corresponding to elimination of water and hydroxide decomposition.

In the fig. 4.12 TG/DSC pattern of $\text{SnMn(OH)}_4 \cdot x\text{H}_2\text{O}$ precursor decomposition, weight loss is observed between 90-120°C due to the loss of water and further weight loss around 250- 300°C due to decomposition of hydroxides and after that initiation of a solid state diffusion up to 800°C leading to solid solution formation. The Ce-Mn hydroxide decomposition shows similar TG/DSC pattern.

Fig.4.13 depicts the TG/DSC pattern of CoPc decomposition. It starts decomposing at 425°C and shows weight loss till 700°C. An exothermic peak is seen at 484°C. The decomposition products suspected to be formed are phthalic residue, ammonia and cobalt oxide. At 745°C there is sharp endothermic rise due to the formation of metal oxide as indicated by DSC peak¹⁵¹. Copper phthalocyanine does not have sharp melting point⁴². It starts decomposing at 450°C and shows weight loss till 800°C. An exothermic peak around 459°C corresponds to CuPc decomposition. At 830°C there is sharp endothermic rise may be due to the formation of CuO as indicated by DSC peak.

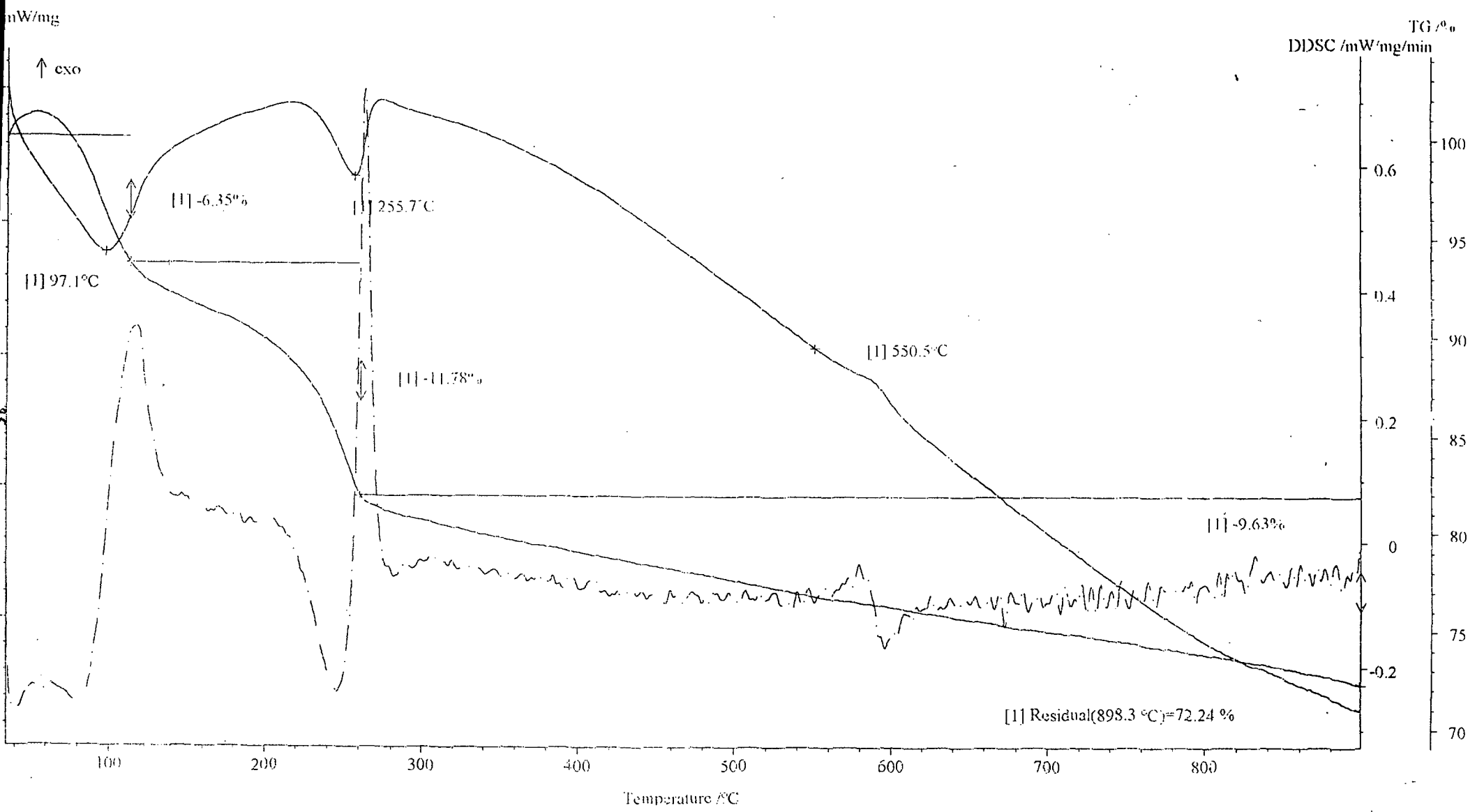


Fig. 4.12 TG/DSC pattern of $\text{Sn}_{0.9}\text{Mn}_{0.1}(\text{OH})_n \cdot x\text{H}_2\text{O}$ precursor decomposition

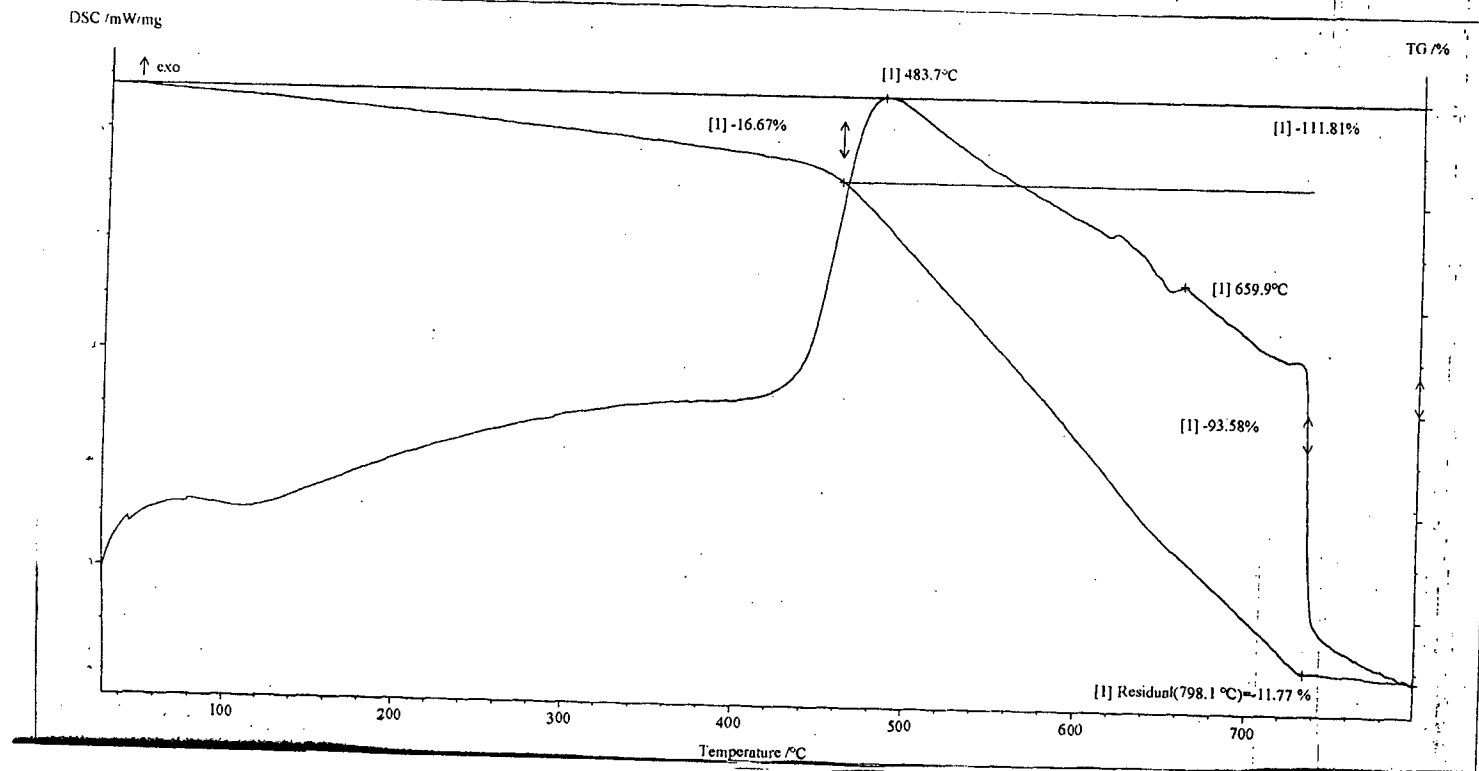


Fig 4.13 TG/DSC pattern of CoPc decomposition

The TG/DSC patterns of NiPc and FePc are slightly different than that of CoPc and CuPc. They start decomposing around 200-300°C.

The thermal stability of the phthalocyanine molecule is due to its extremely high aromatic character which exceeds that of a benzene ring by a factor of 15^{80} . The thermal stabilities of the substituted phthalocyanines are lower than those the unsubstituted, FePc or CoPc compounds

4.4 Electrical resistivity

Electrical resistivity of the prepared samples were measured using two probe method at various temperature range from room temperature to 250°C. The resistivity of these oxides was found in the semiconducting range. Plot of resistivity $\log(\rho)$ versus inverse temperature are shown in figures 4.14 - 4.18. The resistivity of the phthalocyanines was measured from room temperature to 150°C. Resistivity was found to decrease with increase in the temperature for all the compositions under investigation.

Fig 4.14 shows the resistivity behaviour of $Ce_{1-x}Fe_xO_2$ series during cooling cycles. Pure Cerium oxide is basically a poor oxide ion conductor. When trivalent dopant cations (M^{3+}) substitute for Ce^{4+} , one oxygen- ion is introduced for every second M^{3+} cation. The conductivities are significantly enhanced in $Ce_{1-x}Fe_xO_2$ solids by increasing the oxygen vacancies ($V_O^{\cdot\cdot}$)³⁶. The

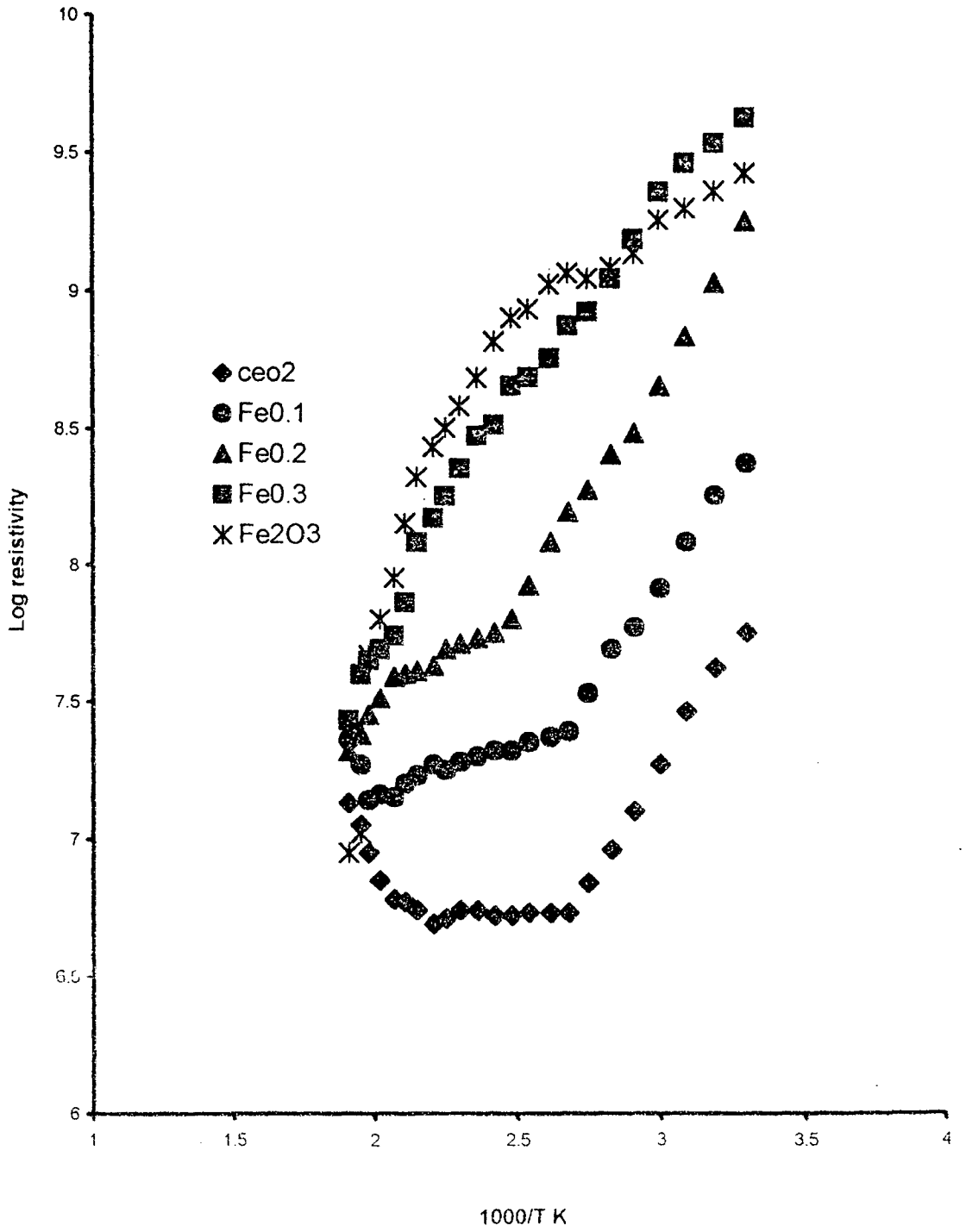


Fig. 4.14 Variation of electrical resistivity of $Ce_{1-x}Fe_xO_2$ with temperature

electrical resistivity decreases systematically with increasing Fe substitution and reaches a maximum for the composition $\text{Ce}_{0.7}\text{Fe}_{0.3}\text{O}_2$.

For $\text{Ce}_{1-x}\text{Sn}_x\text{O}_2$ series as shown in Fig. 4.15 all the samples show linear decrease in resistivity showing semiconducting behaviour. Resistivity value is highest for $\text{Ce}_{0.8}\text{Sn}_{0.2}\text{O}_2$. SnO_2 is an n-type semiconductor since oxygen vacancies or interstitial Sn^{4+} are donor sites^{48,98}. According to literature³⁹ for CeO_2 - SnO_2 samples the variation of $\log \rho$ Vs $1000/T$ show two different slopes, which may be assigned to two different conduction mechanisms, due to the migration of charge carriers in presence of pores. The sample lose water on dry argon flushing, indicating contribution of protonic conduction on wet samples. The progressing dehydration is accompanied by the decrease of conductivity. The conductivity of SnO_2 increases with increasing reduction or non-stoichiometry of the oxide. Doped SnO_2 are characterized by high electrical conductivity. A plot of $\log \rho$ Vs $1000/T$ for $\text{Sn}_{1-x}\text{Mn}_x\text{O}_2$ series is shown in fig.4.16.

Similar observation can be made for $\text{Ce}_{1-x}\text{Mn}_x\text{O}_2$ series as shown in fig.4.17. The resistivity decreases with increase in temperature i.e. conductivity increases with temperature showing semiconducting behaviour.

Phthalocyanines are a class of organic semiconductors, whose electrical properties have considerable importance owing to their potential application in

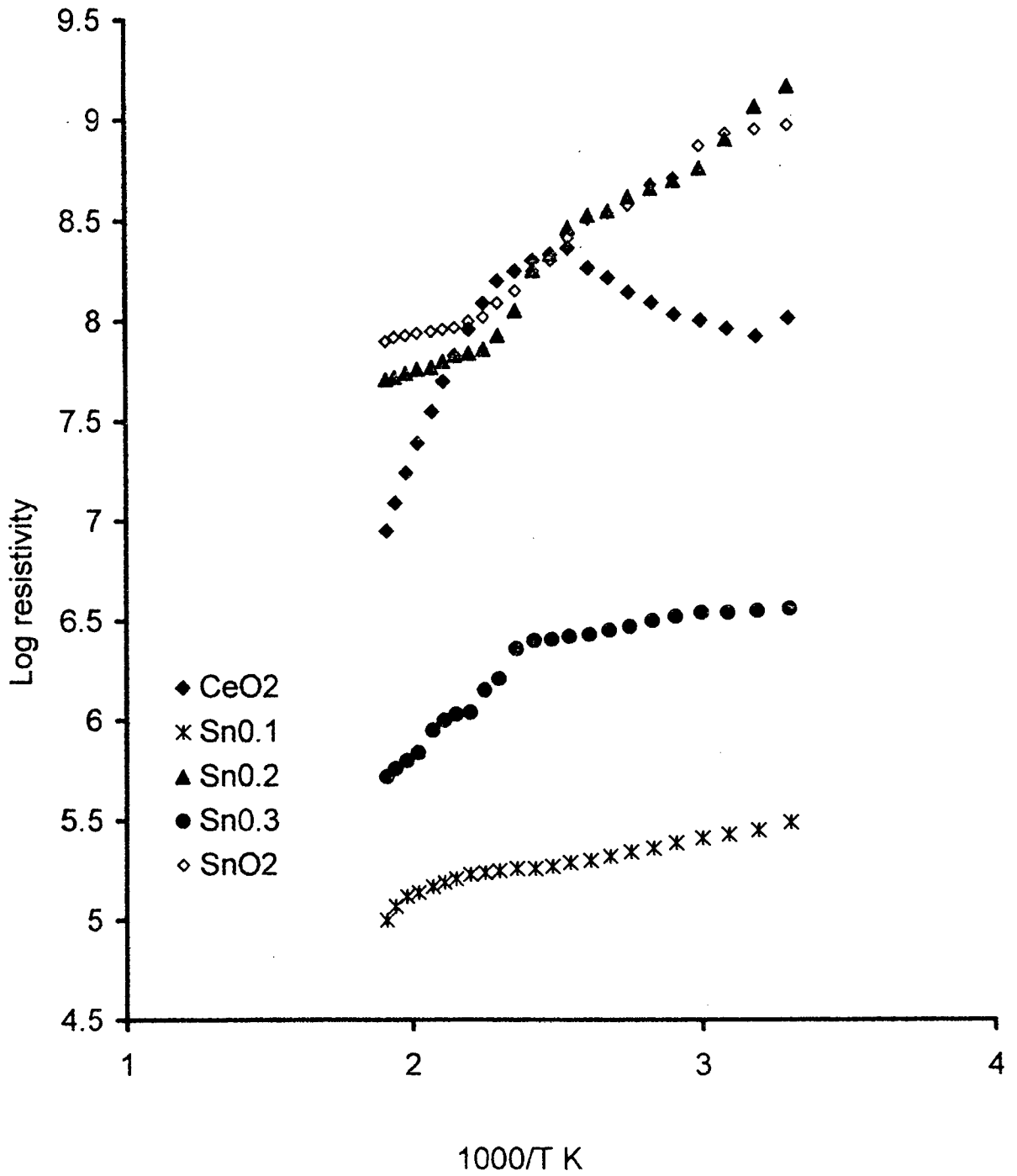


Fig.4.15 Variation of electrical resistivity of $Ce_{1-x}Sn_xO_2$ with temperature

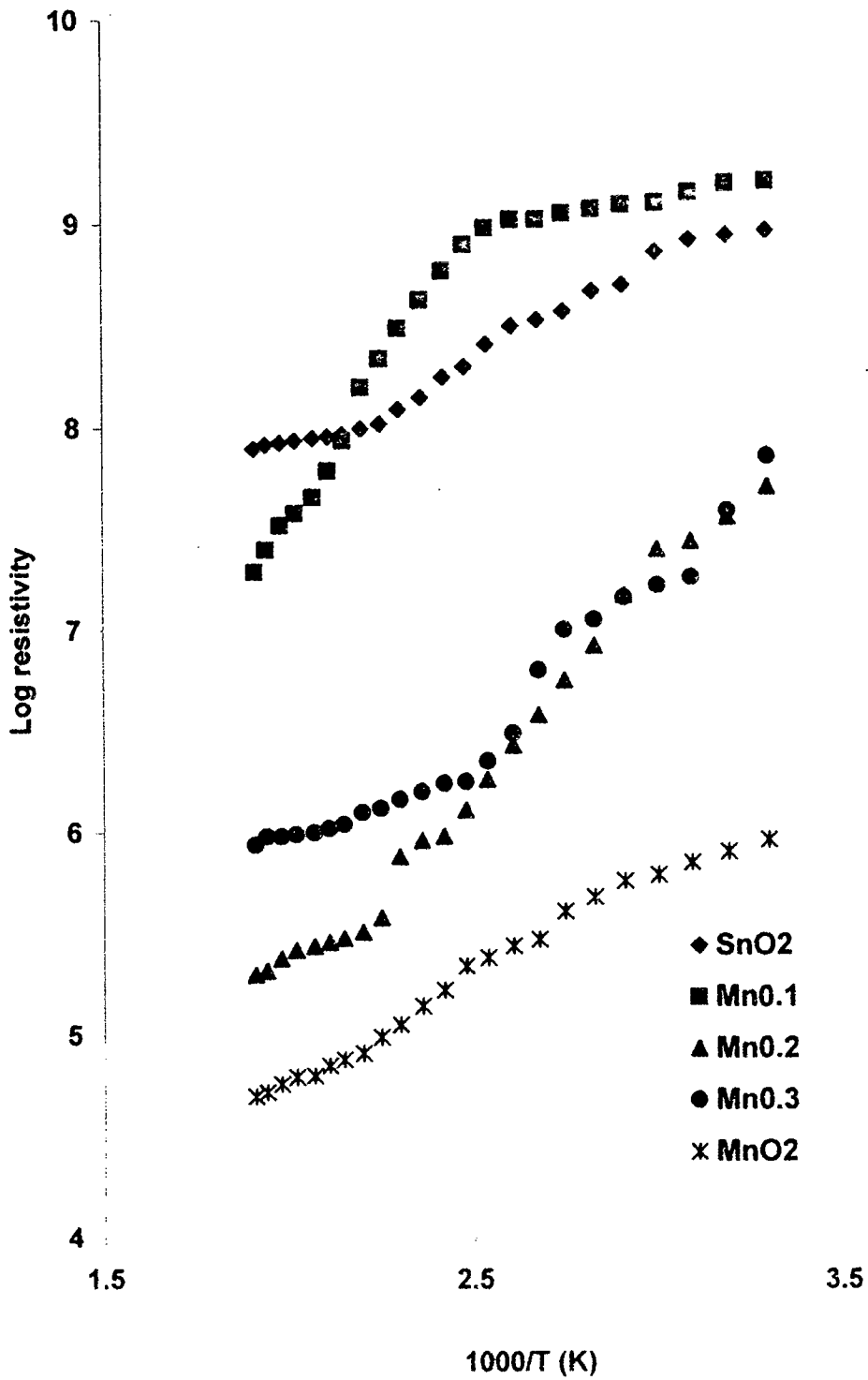


Fig. 4.16 Variation of electrical resistivity of $\text{Sn}_{1-x}\text{Mn}_x\text{O}_2$ with temperature

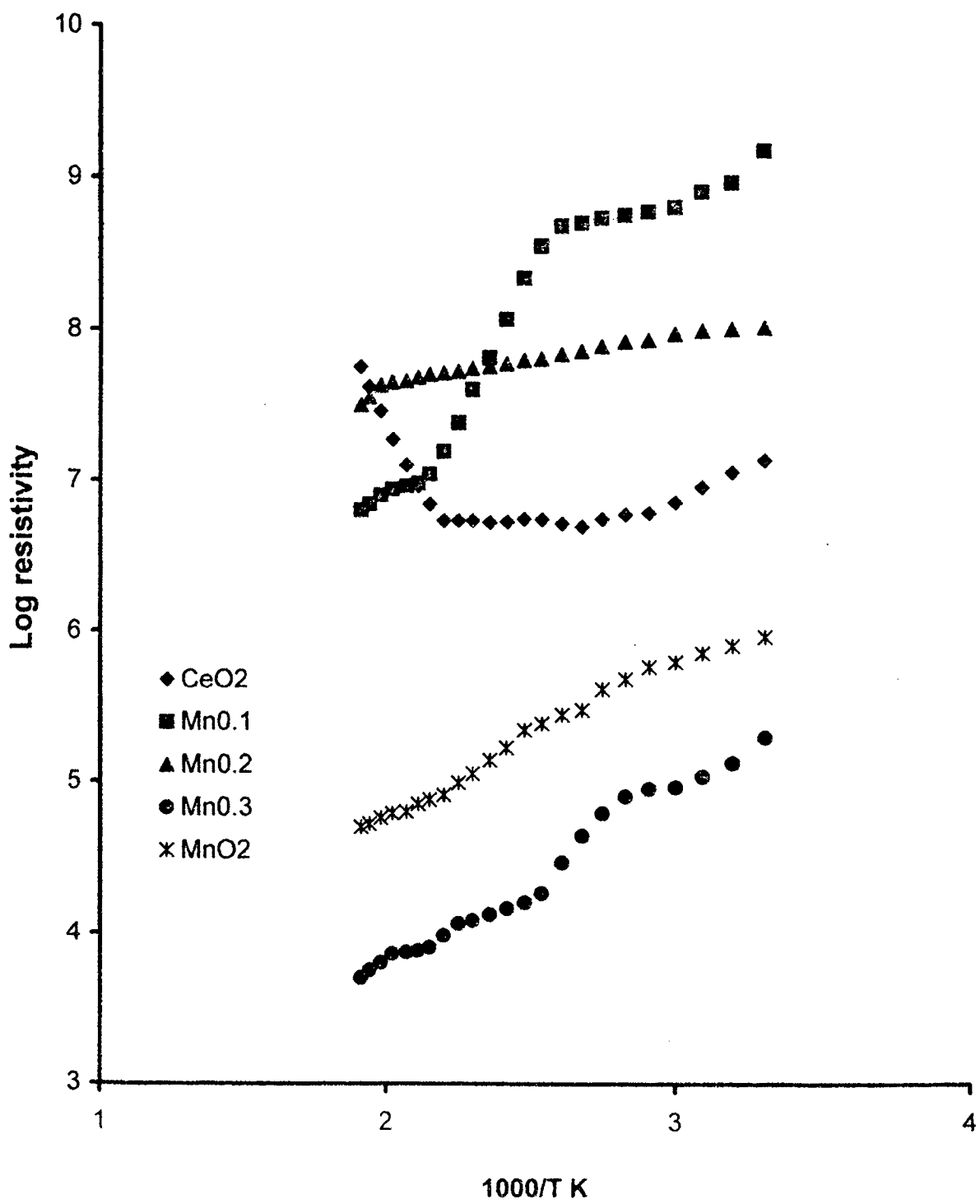


Fig.4.17 Variation of electrical resistivity of $Ce_{1-x}Mn_xO_2$ with temperature

electronic devices and sensor systems. Achar and Lokesh¹⁰⁶ studied the electrical conductivity measurement for freshly prepared four polymorphs of CuPc in the temperature range 25-200⁰C in the air atmosphere and found a marked difference in variation of electrical properties with temperature for different phases before and after the heat treatment. A phthalocyanine molecule is a good electron donor. The ring of N- atoms around the central metal atoms forms a potential well which is responsible for the semiconducting properties. Transfer of charge between molecules in films or single crystal is only possible by crossing the potential well⁸.

Electrical resistivities of the phthalocyanines were studied from room temperature to 150⁰C. They showed decrease in resistivity with temperature. Resistivity pattern of the phthalocyanines is shown in fig.4.18.

4.5 Magnetic susceptibility

The magnetic susceptibility of different paramagnetic samples was determined by Gouy method at room temperature using field strength of 8000 gauss. The magnetic moments in Bohr Magneton were calculated using an expression

$$\mu_{\text{eff}} = 2.84 \sqrt{\chi_m \times T},$$

Where, χ_m is the molar susceptibility at room temperature, T is the temperature.

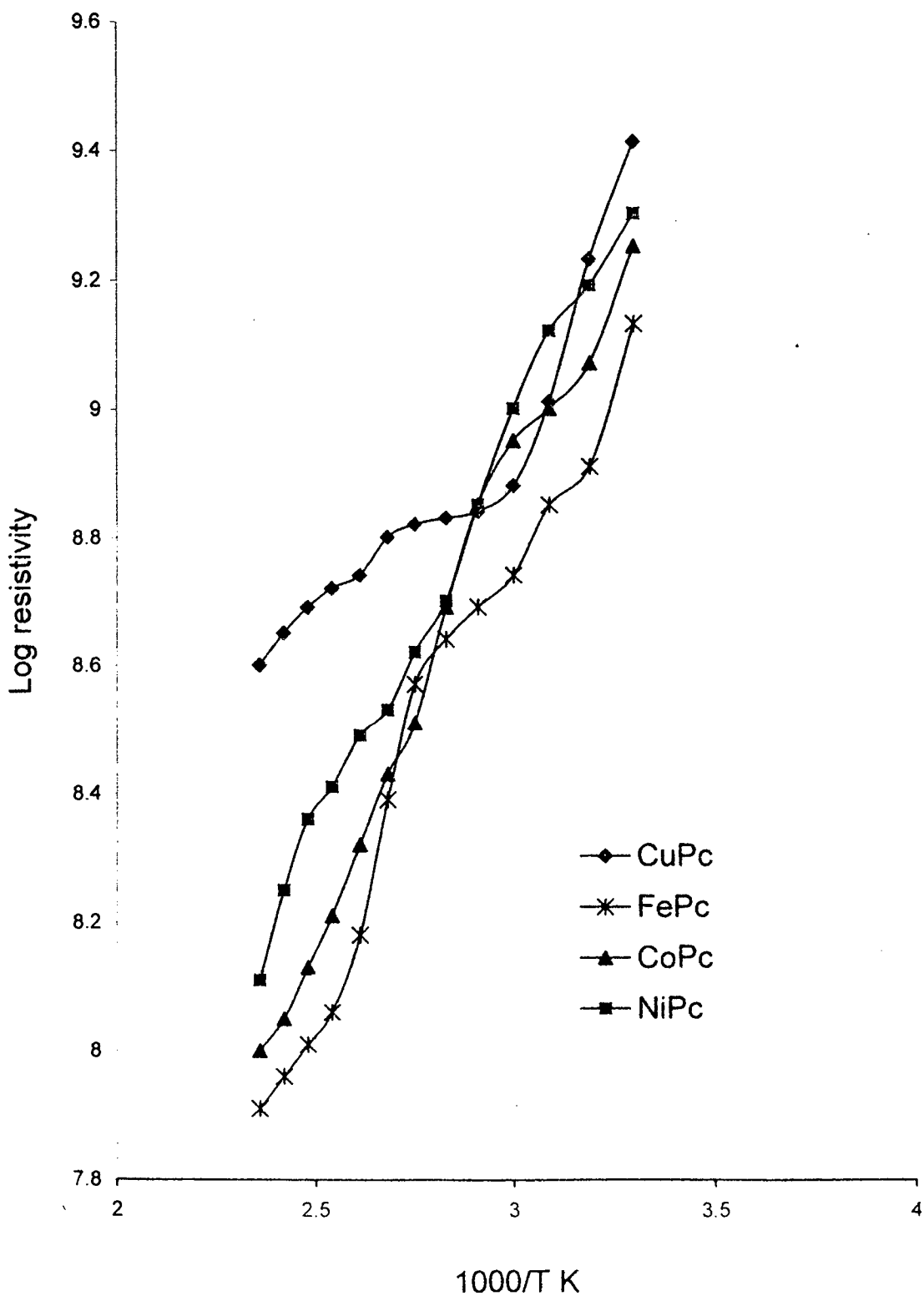


Fig.4.18 Variation of electrical resistivity of metal phthalocyanines with temperature

The observed gram susceptibility of oxides is shown in table 4.1-4.3. Most of the samples are paramagnetic. The magnetic susceptibility values of $Ce_{1-x}Fe_xO_2$ were in the range of 2.984×10^{-6} to 14.37×10^{-6} cgs units. For $Ce_{1-x}Sn_xO_2$ series, the values were 7.64×10^{-6} to 2.68×10^{-6} cgs units decreasing with Sn substitution and for $Ce_{1-x}Mn_xO_2$ series, the values were in the range of 4.06×10^{-6} to 6.84×10^{-6} cgs units increasing with the Mn substitution. The magnetic moment also increases which comes from both Mn^{4+} and Ce^{3+} ions. For $Sn_{1-x}Mn_xO_2$ series, the values were 5.16×10^{-6} to 18.60×10^{-6} cgs units increasing with Mn substitution. The diamagnetic nature gradually changes to paramagnetic nature with Mn substitution in SnO_2 doped samples.

Among phthalocyanines, Cobalt phthalocyanine and Copper phthalocyanine are paramagnetic in nature. Achar and Lokesh¹⁰⁶ studied the magnetic susceptibility of α , β , γ and δ Copper phthalocyanine polymorphs at ambient temperature and varying the magnetic field strengths. They found that higher or lower values of μ_{eff} indicate the contribution of direct or super exchange intermolecular interaction spacing and inclination of the molecules in the crystal lattice. During the process of stacking, each Pc molecule is stacked to the neighboring molecule along the b-axis in such a way that each molecule is contributing either a nitrogen atom at inter-planar distance of 3.38 \AA above or below the central metal. This inter-planar distance provide a suitable

Table 4.1 The Magnetic susceptibility values of $Ce_{1-x}Fe_xO_2$ and $Ce_{1-x}Sn_xO_2$ samples

Sample	Magnetic susceptibility (χ_g cgs units)	μ_{eff} (B.M)
CeO_2	2.984×10^{-6}	1.06
$Ce_{0.9}Fe_{0.1}O_2$	8.987×10^{-6}	1.80
$Ce_{0.8}Fe_{0.2}O_2$	11.2×10^{-6}	1.95
$Ce_{0.7}Fe_{0.3}O_2$	14.37×10^{-6}	2.14
$Ce_{0.9}Sn_{0.1}O_2$	7.39×10^{-6}	1.66
$Ce_{0.8}Sn_{0.2}O_2$	7.20×10^{-6}	1.63
$Ce_{0.7}Sn_{0.3}O_2$	2.68×10^{-6}	0.99

Table 4.2 The Magnetic susceptibility values of $Ce_{1-x}Mn_xO_2$ and

$Sn_{1-x}Mn_xO_2$ series

Sample	Magnetic susceptibility (χ_g cgs units)	μ_{eff} (BM)
$Ce_{0.9}Mn_{0.1}O_2$	4.06×10^{-6}	1.21
$Ce_{0.8}Mn_{0.2}O_2$	4.98×10^{-6}	1.30
$Ce_{0.7}Mn_{0.3}O_2$	6.84×10^{-6}	1.48
MnO_2	84.98×10^{-6}	3.84
$Sn_{0.9}Mn_{0.1}O_2$	5.165×10^{-6}	1.27
$Sn_{0.8}Mn_{0.2}O_2$	9.2×10^{-6}	1.66
$Sn_{0.7}Mn_{0.3}O_2$	18.6×10^{-6}	2.17

Table 4.3 The Magnetic susceptibility values of
Metal phthalocyanines

Sample	Magnetic susceptibility χ_g cgs units	μ_{eff} (B.M.)
Copper phthalocyanine	27.9×10^{-6}	2.61
Cobalt phthalocyanine	1.8×10^{-6}	1.58

pathway for spin- spin coupling interaction between adjacent metal atoms either directly or super exchange through the N atoms of the molecule.

4.6 Saturation magnetization

The saturation magnetization was measured for the magnetic samples such as α -Fe₂O₃ and FePc using hysteresis loop tracer. The results are shown in table 4.4. Since the magnetic susceptibility values are higher, magnetic moments were calculated for these samples using Nickel as a standard material.

4.7. ESR Study

ESR studies were carried out for various samples to get an insight about the photo-catalytically active and paramagnetic species. The technique was used as qualitative tool to ascertain the changes occurring with doping in CeO₂ structure. ESR data of representative samples recorded at room temperature is presented in table 4.5. ESR spectra of some representative samples are shown in figures 4.19 **a-c**. The line width depends on the relaxation time of the spin state through either or both of the processes. (1) spin-lattice relaxation and (2) spin-spin relaxation. The interaction of the paramagnetic ions with the thermal vibrations of the lattice leads to a short spin-lattice relaxation time.

Table 4.4 The observed Saturation magnetization values at
room temperature

No	Sample	Saturation magnetization emu/g
1	Ni (standard)	56
2	α -Fe ₂ O ₃	3.18
3	Iron phthalocyanine	2.1

Table 4.5 ESR data of representative samples at room temperature

Sample	g value ($g_{1,2}$)	Line width (gauss)
CeO ₂	3.8598	384
	4.4974	192
Ce _{0.8} Fe _{0.2} O ₂	2.0080	672
	4.302	640
Ce _{0.9} Mn _{0.1} O ₂	2.0041	400
Sn _{0.9} Mn _{0.1} O ₂	1.962	1680
Ce _{0.8} Sn _{0.2} O ₂	4.5033	192
	2.0673	112
CuPc	2.00277	500
CoPc	2.5962	1912

ESR signal in CeO_2 is due to paramagnetic Ce^{3+} anion vacancy^{17,35}. The ESR spectrum of CeO_2 shows peaks at $g = 3.85$ and $g = 4.49$ due to Ce^{3+} type defects present in CeO_2 crystalline structure¹⁹. There is no ESR signal due to Ce-Mn because Mn^{3+} and Mn^{4+} are ESR inactive.

ESR spectra of copper phthalocyanine and cobalt phthalocyanine are presented in fig.4.19. The data are in agreement with the magnetic susceptibility measurement regarding the paramagnetic nature of the compounds. The ESR signal observed is due to $-1/2 g\beta H$ to $+1/2 g\beta H$ transition, where g is the Lande, or spectroscopies splitting factor, β is the electron Bohr magneton and H is the applied magnetic field. This single energy transition signal is modified with the axially symmetric copper phthalocyanine which has D_{4h} symmetry¹⁰⁶.

In an ideal case for CuPc, the unpaired copper $d_{x^2-y^2}$ electron residing in D_{4h} symmetry interacts with its own nucleus of spin $3/2$ and each of its four ligands nitrogen nuclei of spin 1 . So, 36 discrete transition signals with the intensity ratio $1:4:10:16:19:16:10:4:1$ for each of 4 subsets are expected. But all the ESR signals of copper phthalocyanine showed with partial resolution and overlapping of the hyperfine structure due to copper atom and superfine structures due to the 4 nitrogen atoms¹⁰⁶.

Fig.4.19 b) shows ESR spectra of $\text{Ce}_{0.8}\text{Fe}_{0.2}\text{O}_2$ sample recorded at room temperature. The spectrum shows a broad line with two low intensity peaks at g values of about 2.0 and 4.3. Fe^{3+} has five unpaired electrons in the low field, high spin state (${}^6\text{S}_{5/2}$) and only one in high field. In the former case, since the symmetry is spherical, $g = 2.0080$. Only one signal at the same g value would be observed in perfect tetrahedral or octahedral symmetries. In⁸ distorted tetrahedral or distorted octahedral symmetries the powder spectrum can display signals with g from 2 to 6 when the symmetry is lower than D_{4h} (orthorhombic) one can observe an isotropic signal in the range $g = 4.29$.

In the present study, the $g = 2.0080$ in $\text{Ce}_{0.8}\text{Fe}_{0.2}\text{O}_2$ sample is assigned to Fe^{3+} ions incorporated in the ceria lattice³⁵.

RSIC, IIT, BOMBAY

Scan Range $\times 4,000$ G Time Constant sec Modulation Amplitude $\times 2.0$ G Receiver Gain 6.3×10^2 10 Microwave Power 5.0 mW Operator _____
 Field Set 2,400 G Scan Time hrs min Modulation Frequency Hz Temperature $^{\circ}$ C Microwave Frequency GHz Date _____ Remarks Gen. l.u.

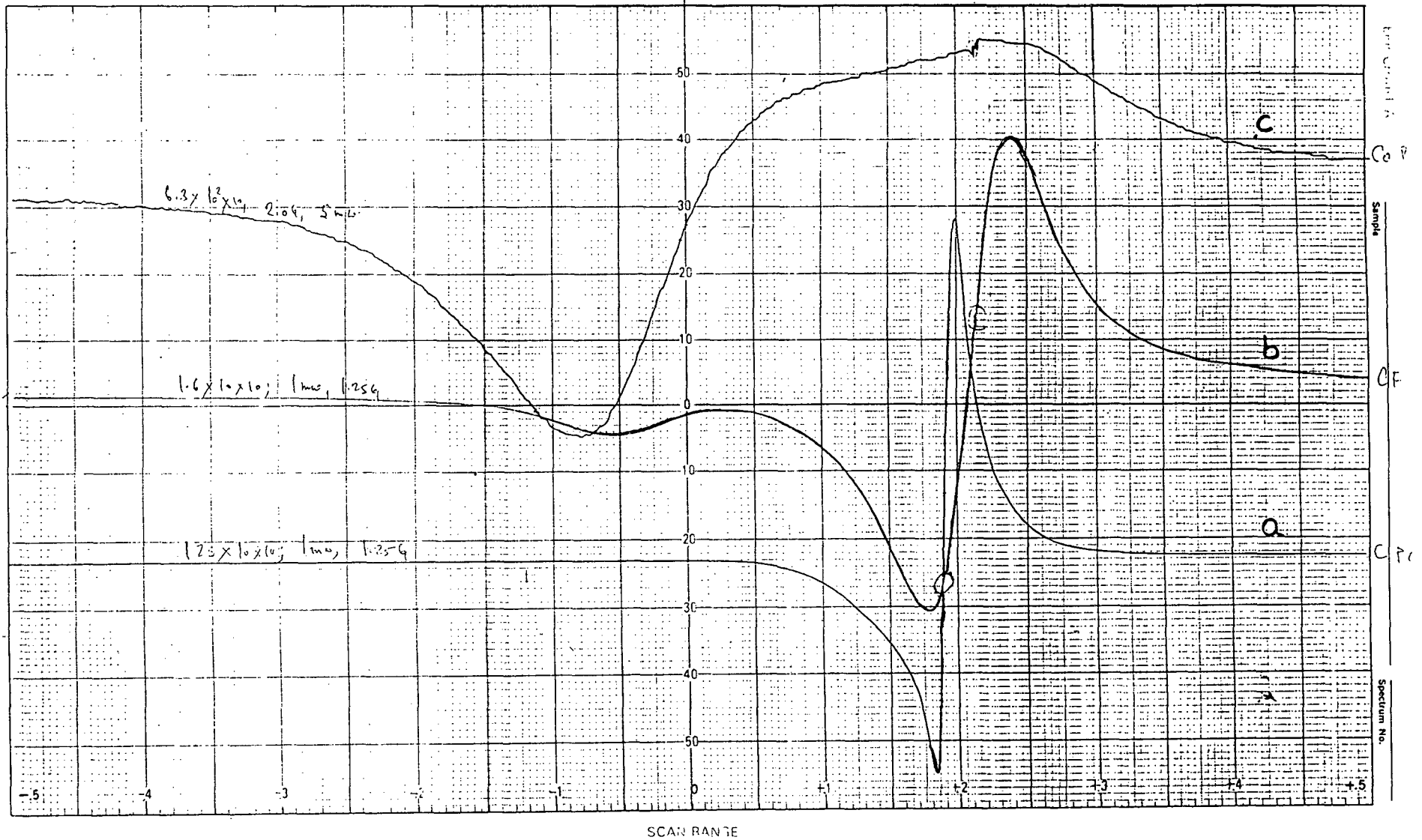


Fig. 4.19 ESR spectra of a) CuPc b) Ce_{0.8}Fe_{0.2}O₂ c) CoPc

CHAPTER 5

PHOTOCATALYTIC STUDIES

PHOTOCATALYTIC STUDIES

Semiconductor photocatalysis is an efficient way for the destruction of various pollutants. In this chapter the photocatalytic activity of CeO_2 and SnO_2 with effect of dopants is being discussed with respect to Naphthol Blue Black dye degradation separately for series- I ($\text{Ce}_{1-x}\text{Sn}_x\text{O}_2$), series-II ($\text{Ce}_{1-x}\text{Fe}_x\text{O}_2$), series -III ($\text{Ce}_{1-x}\text{Mn}_x\text{O}_2$), series- IV ($\text{Sn}_{1-x}\text{Mn}_x\text{O}_2$) and series- V (MPC) and Auramine dye degradation on selected series- I and series- V. These reactions are significant from the point of environmental pollution control.

The surface area and band gap energy of the samples were correlated with the photocatalytic activity for the degradation of textile dyes.

5.1 UV-visible spectroscopy

The UV-visible spectrum observed for phthalocyanines originates from molecular orbitals within the aromatic 18 π electron system and from overlapping orbitals on the central metal. The conjugated double bonds within the crystal structure create electron orbitals which overlap with molecular π orbitals. These electrons are able to transfer energy throughout the structure and are responsible for the absorption peaks^{41,79}.

The UV-visible spectra of the phthalocyanine core is dominated by two intense bands, the Q band around 680 nm and the B band in the near UV region at around 330 nm, both correlate to $\pi - \pi^*$ transitions⁸⁶. Copper phthalocyanine in pyridine showed absorbance at 673 nm. Electron withdrawing substituents cause a blue shift compared to the electroneutral CuPc, whereas electron-donating substituents cause a red shift³². The observed λ_{\max} of the phthalocyanines are shown in table 5.1. The values obtained are in agreement with the literature^{31,83,108}.

5.2 UV- Vis diffuse reflectance spectroscopy

The band gap energy of all the samples were calculated by recording UV-Visible diffuse reflectance spectra using BaSO₄ as a reference material. The band gap energy of the representative samples is shown in table 5.2-5.3. Fig 5.1 illustrates the reflectance spectra of CeO₂ sample. The spectra show that CeO₂ has an intense absorption in the UV that trails into the visible region of the spectrum. The onset of absorption of CeO₂ was at ~430 nm which corresponds to the band gap energy of calculated 2.8 eV. This value is consistent with the characteristics values given in the literature ie $E = 2.8-3.2$ eV²².

Fig 5.2 depicts the reflection spectra of Ce_{0.7}Fe_{0.3}O₂. The sample show a reflection band similar to that recorded for the bare CeO₂. The intensity of this

Table 5.1 UV- visible data of metal phthalocyanines

Sr No	Sample	Wavelength (nm)
1	Copper phthalocyanine	673
2	Cobalt phthalocyanine	658
3	Iron phthalocyanine	655
4	Nickel phthalocyanine	667

Table 5.2 Band gap energy of $Ce_{1-x}Sn_xO_2$ and $Ce_{1-x}Fe_xO_2$ samples

Sr No	Sample	Band gap energy (eV)
1	CeO_2	2.8
2	$Ce_{0.9}Sn_{0.1}O_2$	2.36
3	$Ce_{0.8}Sn_{0.2}O_2$	4.26
4	$Ce_{0.7}Sn_{0.3}O_2$	3.38
5	SnO_2	3.67
6	$Ce_{0.9}Fe_{0.1}O_2$	2.09
7	$Ce_{0.8}Fe_{0.2}O_2$	2.68
8	$Ce_{0.7}Fe_{0.3}O_2$	2.21
9	$\alpha-Fe_2O_3$	2.17

Table 5.3 Band gap energy of $\text{Sn}_{1-x}\text{Mn}_x\text{O}_2$ samples and metal phthalocyanines

Sr No	Sample	Band gap energy eV
1	SnO_2	3.67
2	$\text{Sn}_{0.9}\text{Mn}_{0.1}\text{O}_2$	4.09
3	$\text{Sn}_{0.8}\text{Mn}_{0.2}\text{O}_2$	4.1
4	$\text{Sn}_{0.7}\text{Mn}_{0.3}\text{O}_2$	4.29
5	MnO_2	3.64
6	Copper phthalocyanine	2.87
7	Nickel phthalocyanine	3.81
8	Cobalt phthalocyanine	4.71
9	Iron phthalocyanine	5.67

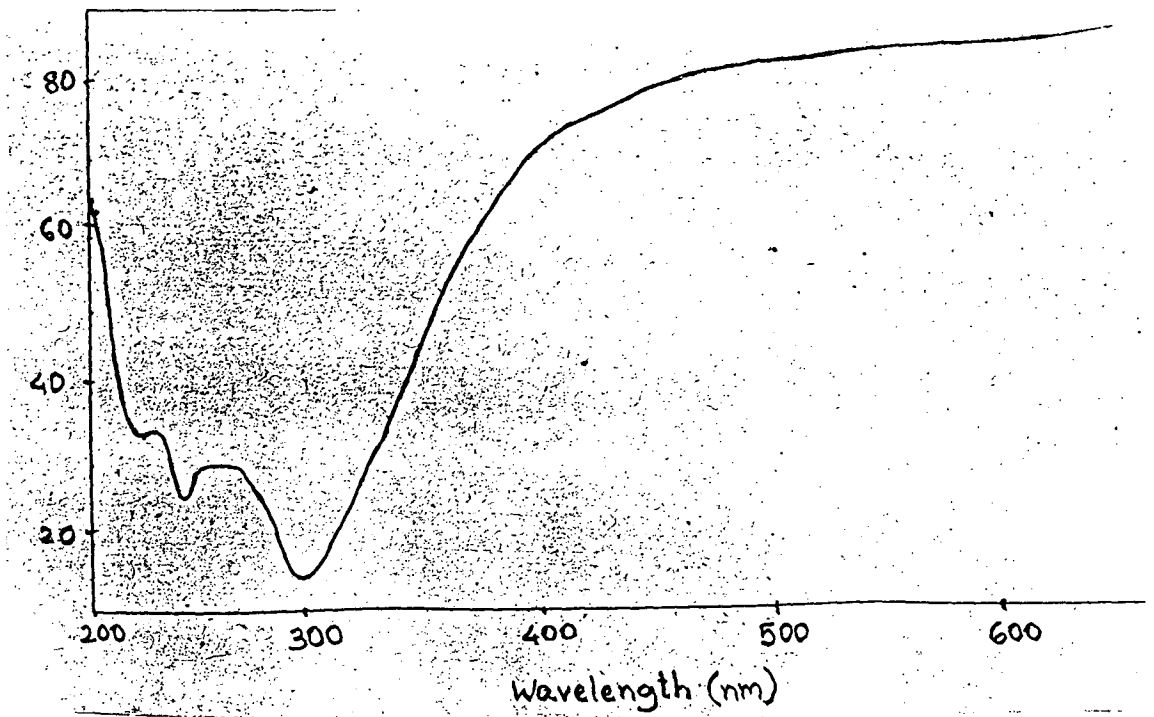


Fig. 5.1 UV-Visible diffuse reflectance spectra of CeO₂ sample

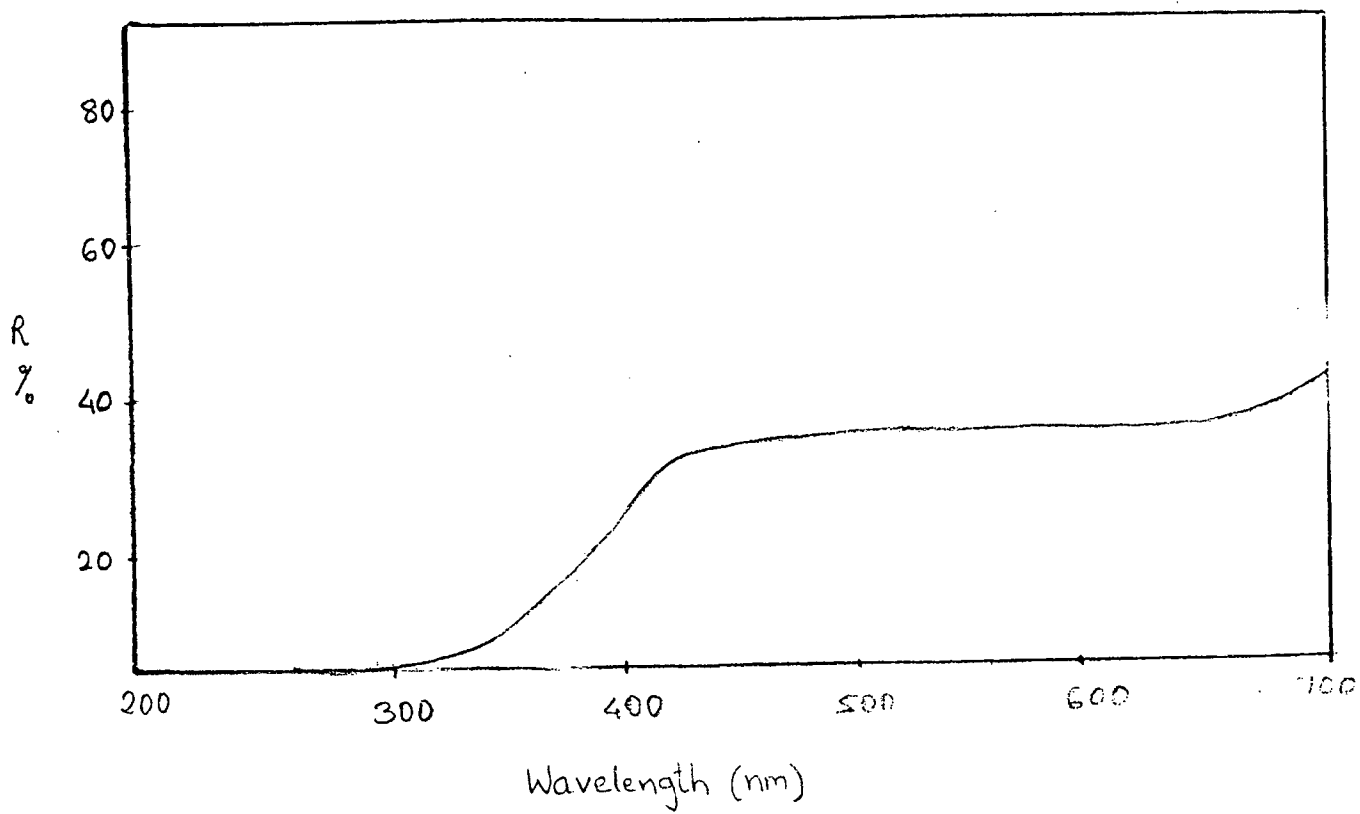


Fig. 5.2 UV-Visible diffuse reflectance spectra of $\text{Ce}_{0.9}\text{Fe}_{0.1}\text{O}_2$

band ascribed to a charge transfer process from oxide orbitals to Fe^{3+} orbitals, increases with the increase of Fe content. Similar observations have been reported for $\alpha\text{-Fe}_2\text{O}_3$ loaded ZnO ⁷. Fig. 5.3 shows the reflectance spectra of SnO_2 . The spectrum of SnO_2 consists of a single, broad intense absorption below 400 nm usually ascribed to a charge transfer process.

5.3 Surface area measurement

Surface areas of the prepared samples were measured using BET nitrogen adsorption method at liquid nitrogen temperature. The samples prepared by co-precipitation method possessed surface area as low as $2.7 \text{ m}^2/\text{g}$ and as high as $26.41 \text{ m}^2/\text{g}$. The surface area of the sample decreases due to sintering. Surface areas of the prepared samples are shown in table 5.4-5.5.

5.4 Photolysis study

Samples prepared were tested for two model photolysis reactions such as photodegradation of textile diazo dye Naphthol Blue Black (NBB) and basic yellow Auramine O using oxygen and sunlight. The progress of the photocatalytic degradation was monitored by UV-visible spectrophotometer by measuring the absorbance of the dye solution at λ_{max} .

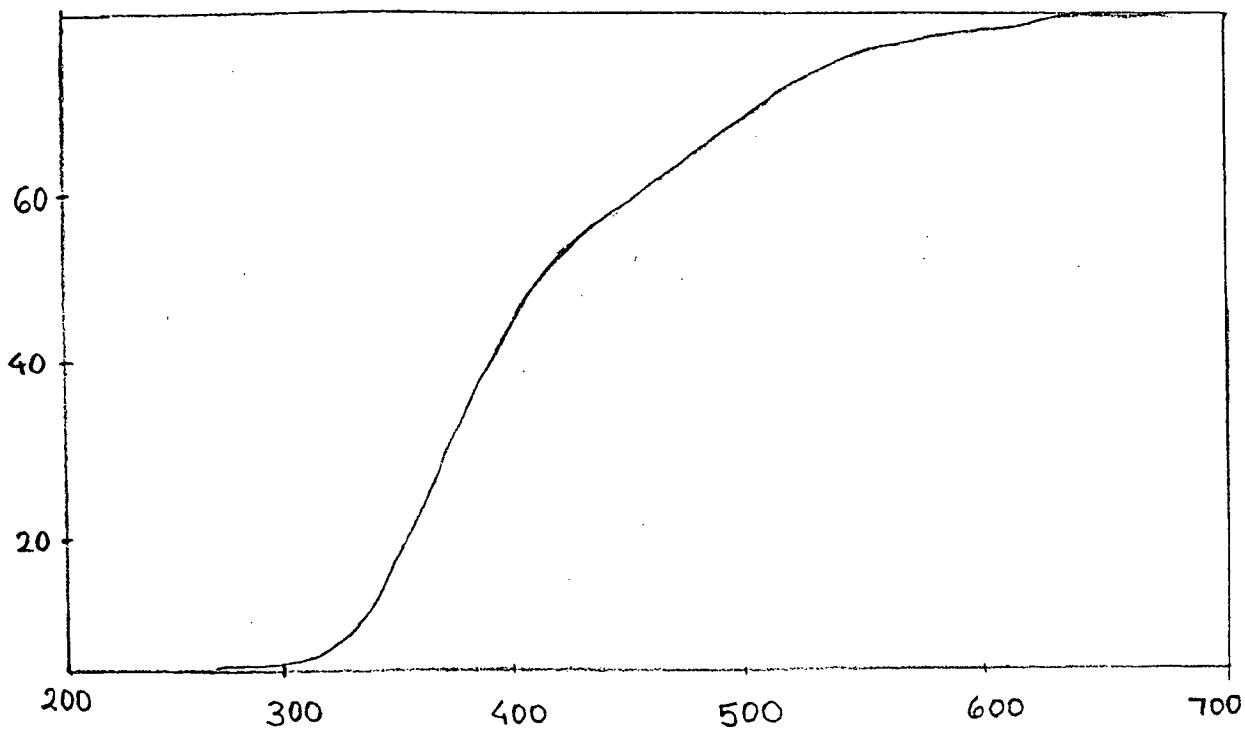


Fig. 5.3 UV-Visible diffuse reflectance spectra of SnO₂

Table 5.4 Surface area of $Ce_{1-x}Sn_xO_2$ and $Ce_{1-x}Fe_xO_2$ samples

Sr No	Sample	Surface area m^2/g
1	CeO_2	7.36
2	$Ce_{0.9}Sn_{0.1}O_2$	3.21
3	$Ce_{0.8}Sn_{0.2}O_2$	4.98
4	$Ce_{0.7}Sn_{0.3}O_2$	6.07
5	SnO_2	8.05
6	$Ce_{0.9}Fe_{0.1}O_2$	8.92
7	$Ce_{0.8}Fe_{0.2}O_2$	5.62
8	$Ce_{0.7}Fe_{0.3}O_2$	3.86
9	$\alpha-Fe_2O_3$	26.41

Table 5.5 Surface area of $Ce_{1-x}Mn_xO_2$ and $Sn_{1-x}Mn_xO_2$ samples

Sr No	Sample	Surface area m^2/g
1	CeO_2	7.36
2	$Ce_{0.9}Mn_{0.1}O_2$	2.7
3	$Ce_{0.8}Mn_{0.2}O_2$	6.5
4	$Ce_{0.7}Mn_{0.3}O_2$	8.34
5	MnO_2	16.07
6	SnO_2	8.05
7	$Sn_{0.9}Mn_{0.1}O_2$	3.91
8	$Sn_{0.8}Mn_{0.2}O_2$	5.8
9	$Sn_{0.7}Mn_{0.3}O_2$	7.73

Naphthol Blue Black as received without further purification was used in the present investigations. The stock solution 10^{-3} M was prepared by dissolving dye in distilled water. The photodegradation of the dye was observed taking 100 ml of the 10^{-5} M dye solution and 200 mg of the prepared photocatalyst sample. The dye solution was first aerated by bubbling oxygen for 5-10 min before adding the catalyst. The irradiation was carried out keeping the reaction mixture under sunlight during fixed period of time.

The desired pH of the solution was adjusted by the addition of previously standardized HCl and NaOH solution. The filtration was performed using Whatmann 41 filter paper to obtain the desired accuracy in measurement of absorbance (O.D.) of the dye solution. A UV-visible spectrophotometer was used for measuring absorbance at different time intervals. The λ_{\max} for the dye was determined by scanning the dye solution in the visible region from 400 – 700 nm range with the help of an UV-visible spectrophotometer.

The reaction was studied for various experimental conditions like using different amount of the catalyst, without aeration, without catalyst, without irradiation and changing the pH conditions from acidic to basic. The degradation products were analysed by HPLC analyzer for qualitative analysis of the dye sample for the representative sample.

The UV-visible spectrum of the Naphthol Blue Black is shown in Fig.

5.4 The NBB dye has absorption in visible region at λ_{max} 618 nm in water.

5.4.1 Optimisation of catalyst loading

The optimum amount of the catalyst for solar induced photocatalytic degradation of Naphthol Blue Black was found to be around 200 mg for 100 ml of the dye solution as shown in Fig.5.5. The dye degradation rate increases with the amount of photocatalyst. Which may be attributed to the increase in the exposed surface area of the semiconductor. But after a certain limit (200 mg) if the amount of photocatalyst is increased further, there will be a saturation point. According to O. E. Kartal et al⁶ the amount of photocatalyst affects both the number of active sites on photocatalyst and the penetration of light through the suspension. As the amount of photocatalyst increases, the number of active sites increases although the penetration of light into the suspension decreases due to a shielding effect. Neppolian et al³ reported that beyond the optimum dose of catalyst loading the solution becomes more opaque and the degradation rate decrease due to the retardation in the penetration of light. It has been also reported by S. Sakthivel et al¹⁴² that increasing the loading of photocatalyst increase the rate of deactivation of activated molecules by collision with ground state photocatalyst.

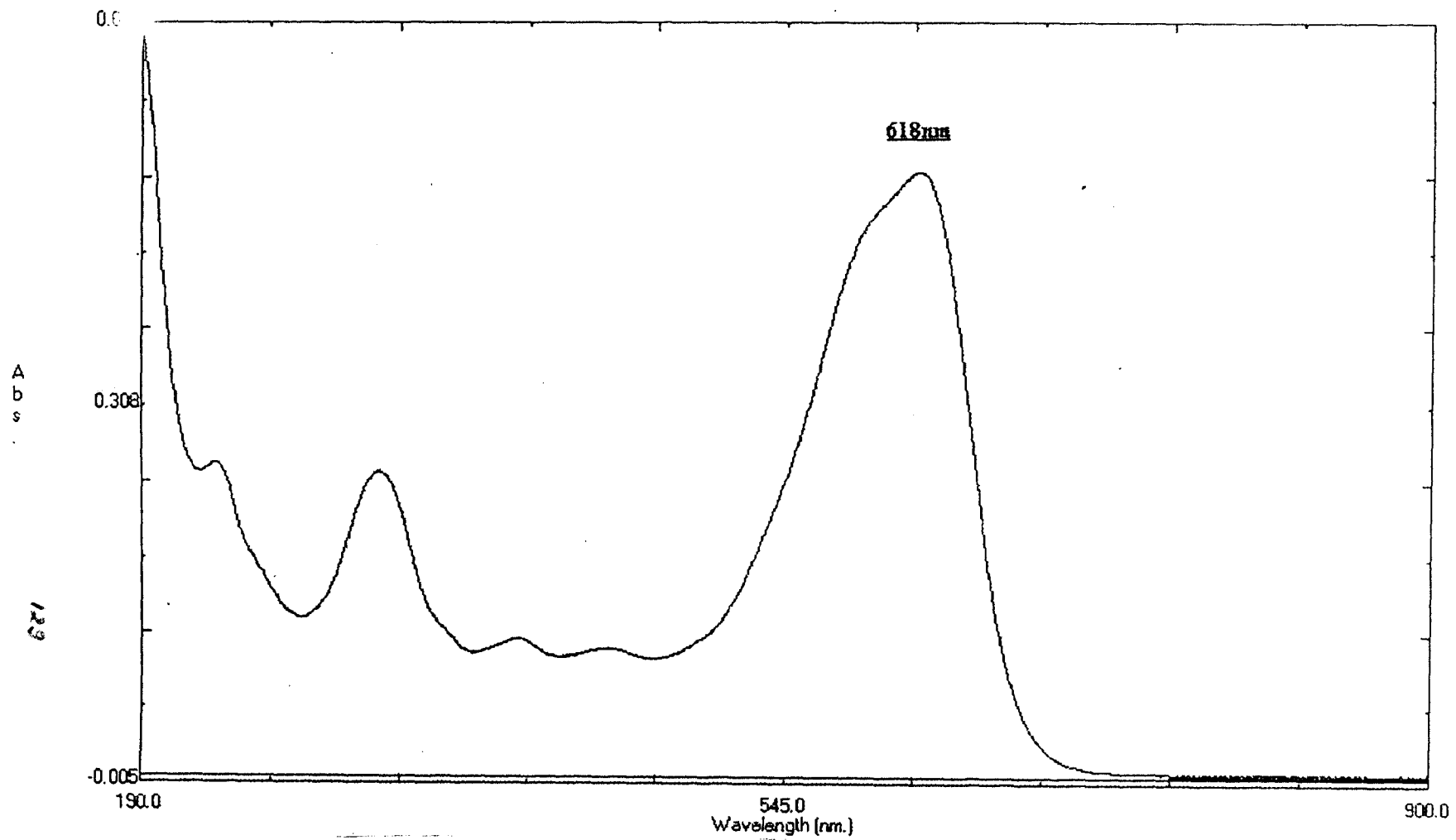


Fig. 5.4 UV-Visible spectra of Naphthol Blue Black

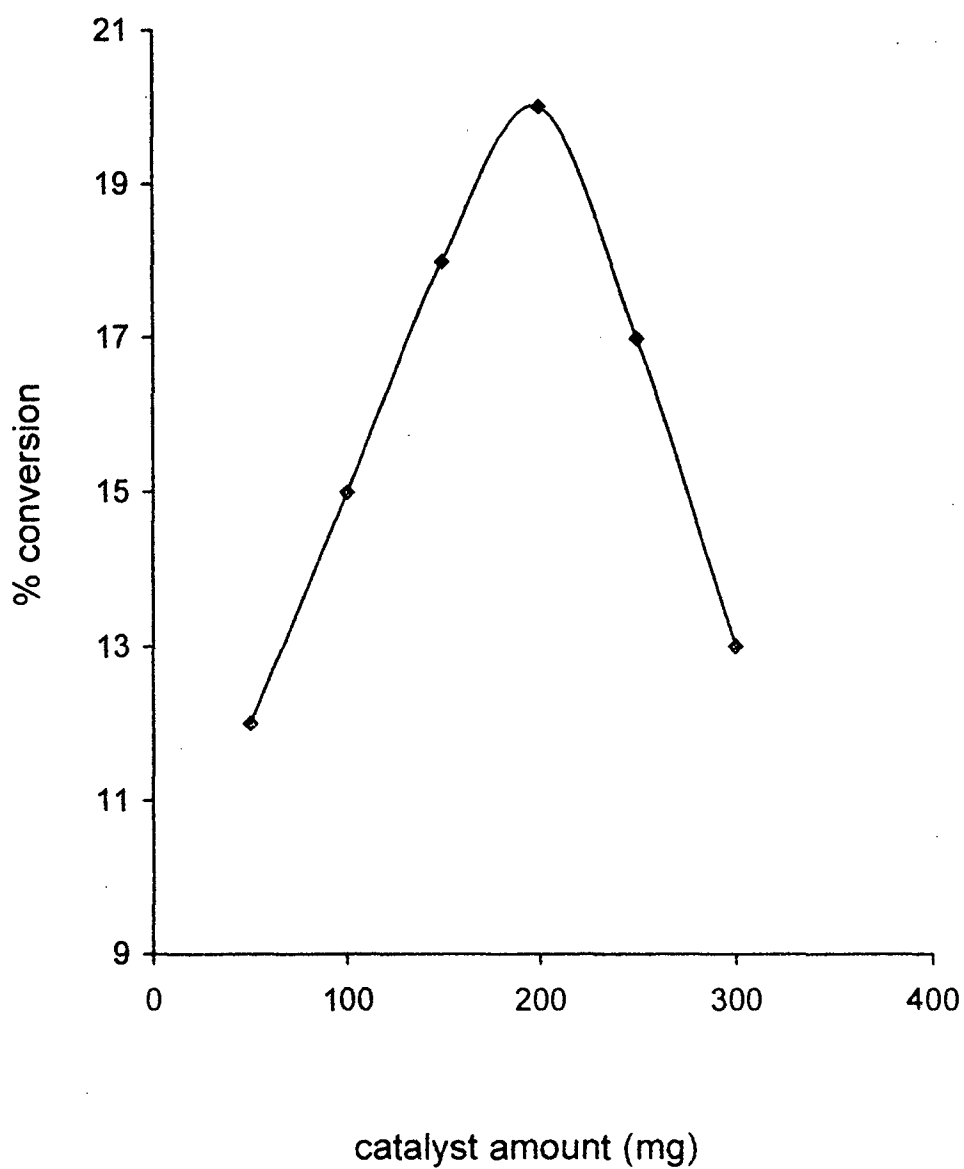


Fig.5.5 Optimisation of catalyst amount for NBB dye degradation

5.4.2 Effect of Oxygen

Oxygen is an electron scavenger and it traps the photogenerated electrons from the conduction band forming O_2^- ions and thus preventing the electron – hole recombination¹⁵³. In the absence of oxygen, electron – hole recombination occurs thus decreasing the rate of degradation. Similar results were observed by T. Zhang et al¹¹⁵ and others⁵ reported that dissolved O_2 in the reaction plays an important role by trapping the conduction band electrons forming super oxide ions (O_2^-) and thus delays the electron – hole recombination ($O_2 + e^- \rightarrow O_2^-$) and at the same time H_2O_2 is formed from O_2 .

5.4.3 Effect of pH

Dye degradation was studied at different pH conditions. pH of the medium is one of the important factor for the degradation because of the amphoteric nature of most of the semiconductors^{140.153}. It has been observed that degradation of dye is faster in alkaline pH ie at pH 10. In alkaline medium, there is a greater probability for the formation of hydroxyl radical (OH^\cdot), which can act as an oxidant, thus increasing the rate of photodegradation of the dye¹²¹.

According to J. Luo et al¹⁰² the photoelectrochemical degradation rate of NBB dye is almost constant in the pH range 1.0 – 4.5 and decreases for the pH values higher than 4.5. While at low pH the main radicals formed in the

reactions of the medium with surface holes $h_{\nu B}$ are most likely Cl_2^- and Cl^- , the increasing pH is favouring the formation of hydroxyl radicals OH^\cdot , a different main degradation path for NBB is expected at $pH > 4.5$. At higher pH, the absorption spectra does not change considerably, only less time is required for the dye degradation to complete.

Increase of pH of the dye solution from 4 to 10 increases the photocatalytic reaction from 20 to 90% at 240 min. The photocatalytic degradation was faster in alkaline pH than in acidic pH range. Similar observation has been reported earlier¹²¹. At acidic pH range the removal efficiency is minimum. This is because at low pH value the semiconductor particle agglomeration reduces the dye adsorption as well as photon absorption. In the azo dye, the azo linkage ($-N = N-$) is particularly susceptible to electrophilic attack by hydroxyl radical. But at low pH the concentration of H^+ is in excess and H^+ ions interact with azo linkage decreasing the electron densities at the azo group. Consequently, the reactivity of hydroxyl radical by electrophilic mechanism decreases.

At alkaline pH the negative surface of the semiconductor with OH^- ions act as an efficient trap for the photo-generated holes and produce hydroxyl radicals. At higher pH, the hydroxyl radical and O_2^- radical can easily diffuse

from the negative surface of semiconductor into the bulk of the reaction solution. Hence hydroxyl radical is responsible for dye degradation.

Fig. 5.6 shows the percentage conversion rate of NBB dye for various experimental conditions with time. In absence of O_2 and catalyst the dye is unable to degrade on irradiation with sunlight. Under solar irradiation, along with oxygen and catalyst the dye is degraded completely with a time of 240 min. Absorption spectra obtained after completion of the NBB dye degradation indicate that the degradation products are colourless. Thus, the photocatalytic degradation provides an efficient way to mineralize this textile diazo dye. The concentration of NBB dye in the solution was determined by measuring the absorbance (A) of the dye solution at $\lambda = 618$ nm. According to M. Muruganathan et al¹⁵⁴ decolourisation is due to destruction of chromophoric azo bond of the dye molecule. The calibration experiments show that the absorbance at 618 nm is proportional to NBB dye concentration. All the prepared samples were tested for their photocatalytic degradation efficiency with respect to time.

5.5 Photodegradation of NBB dye

5.5.1 Series I ($Ce_{1-x}Sn_xO_2$):

The photocatalytic degradation of Naphthol Blue Black with time over $Ce_{0.8}Sn_{0.2}O_2$ is shown in fig 5.7 a). It was observed that concentration of the dye

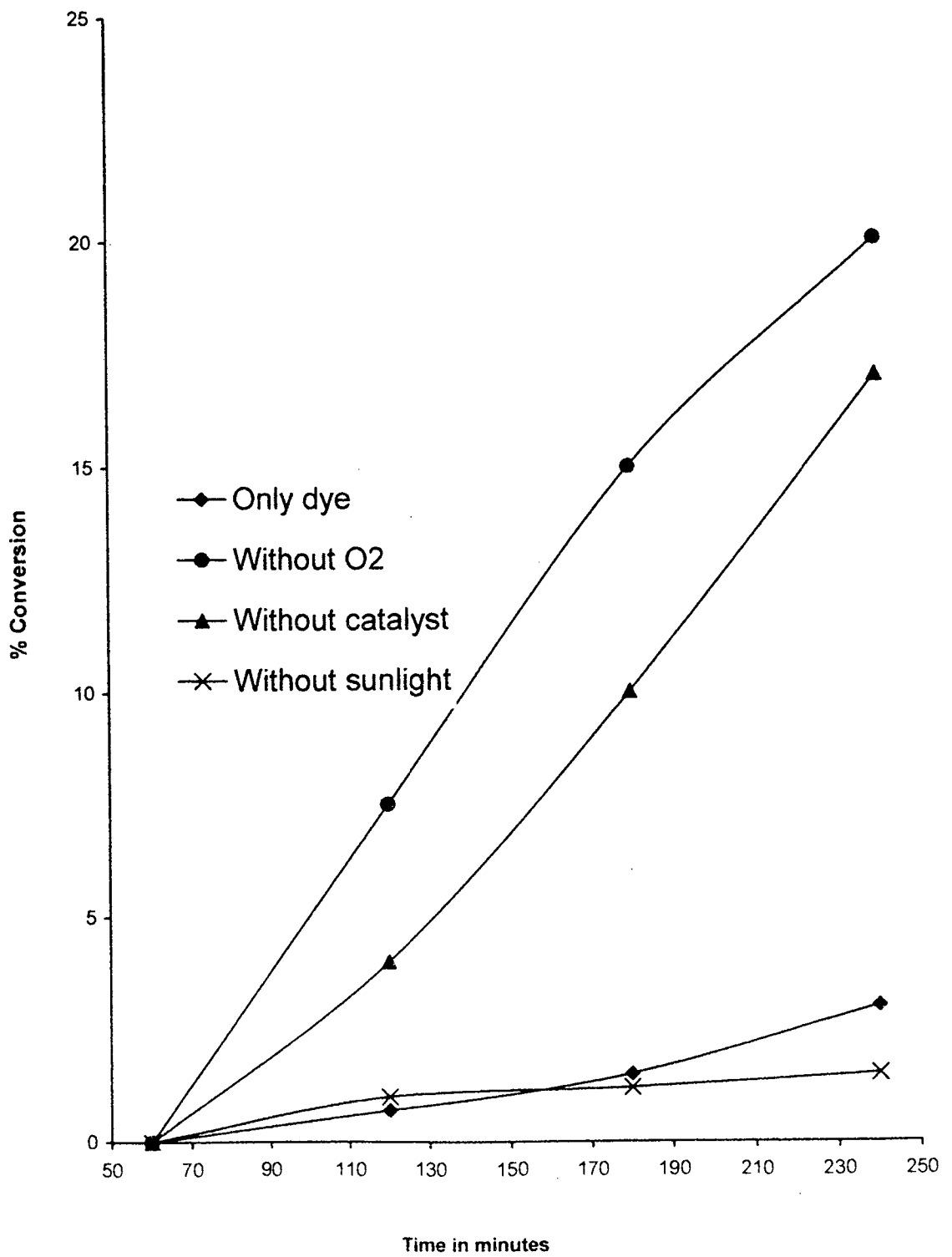


Fig. 5.6 Degradation of NBB dye for various experimental conditions

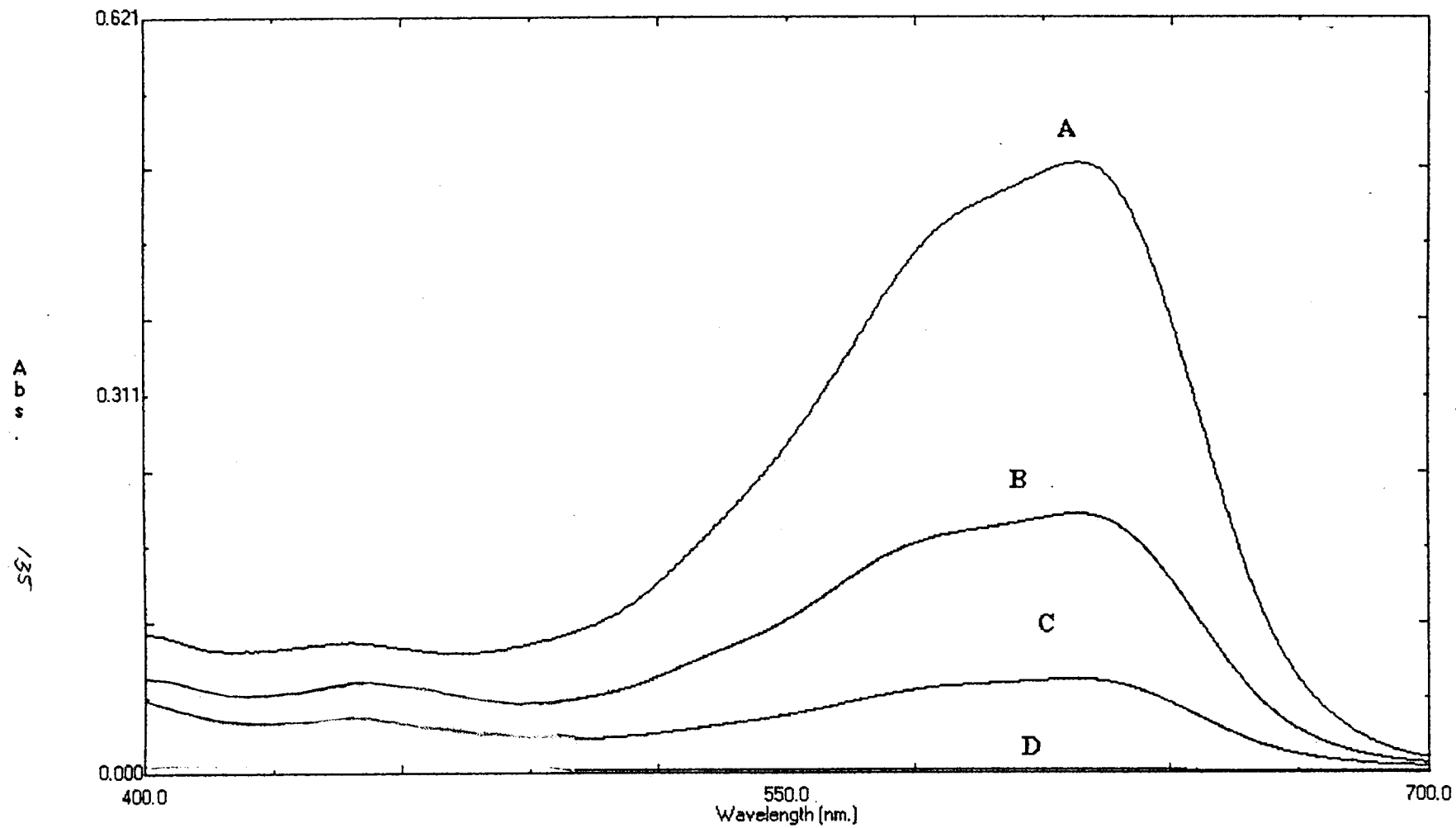


Fig. 5.7 a) Degradation of NBB dye over $\text{Ce}_{0.8}\text{Sn}_{0.2}\text{O}_2$ with time
A) 60 min B) 120 min C) 180 min and D) 240 min

solution decreases with irradiation time. CeO_2 has negligible activity for the degradation of NBB dye. When it is doped with Sn it shows higher photocatalytic activity. As the x increases, the photocatalytic activity increases and it is maximum for $\text{Ce}_{0.8}\text{Sn}_{0.2}\text{O}_2$. Again for $\text{Ce}_{0.7}\text{Sn}_{0.3}\text{O}_2$ photoactivity decreases. SnO_2 show photoactivity between $x = 0.2$ and $x = 0.3$. This is because Sn substitution for Ce in CeO_2 lattice results in a decrease in the rate of photogenerated electron-hole recombination which is attributed to increase in the band gap with Sn content in the $\text{Ce}_{1-x}\text{Sn}_x\text{O}_2$ system. When the system is illuminated by light of adequate wavelength, some electrons are promoted to the conduction band. Since the conduction band shifts toward higher potential, the energy of the electrons on the conduction band is enough to reduce oxygen in air. Thus, the photoexcited electrons and holes on the solid solution can be separated effectively and have a longer lifetime. Therefore, the increase in the photocatalytic oxidation-reduction potential of the semiconductor is inferred to be the origin of the enhanced photoactivity of $\text{Ce}_{1-x}\text{Sn}_x\text{O}_2$ system.

Degradation rate was faster in alkaline pH as observed by others¹²¹.

SnO_2 has higher conversion rate at pH 10 as shown in fig. 5.7.b.

5.5.2 Series –II $\text{Ce}_{1-x}\text{Fe}_x\text{O}_2$:

$\text{Ce}_{1-x}\text{Fe}_x\text{O}_2$ ($x = 0, 0.1, 0.2, 0.3$ and 1.0) show similar results for the photocatalytic degradation of NBB dye. As the x increases, the band gap

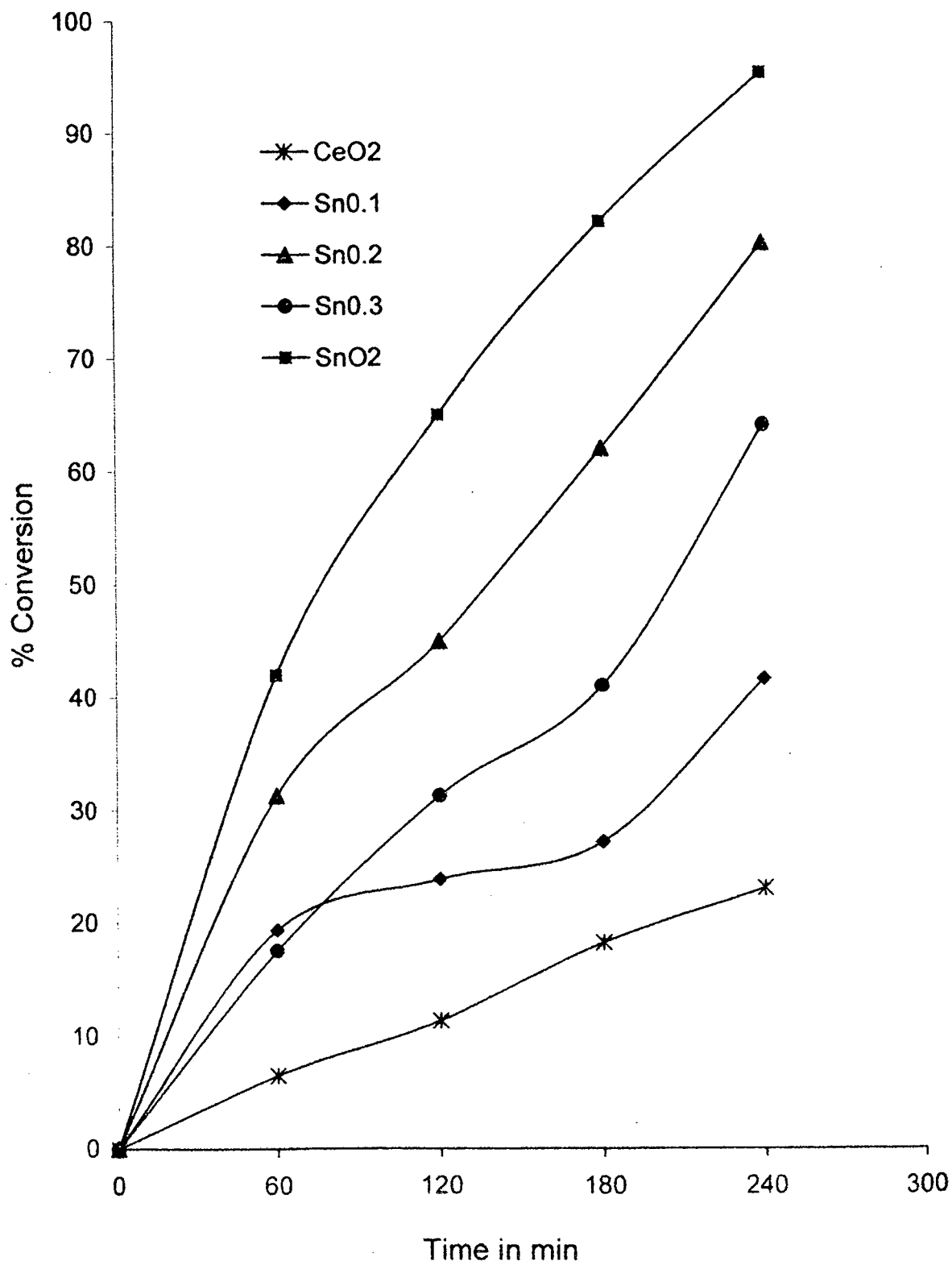


Fig. 5.7 b) % Conversion of NBB dye over $Ce_{1-x}Sn_xO_2$ at pH 10

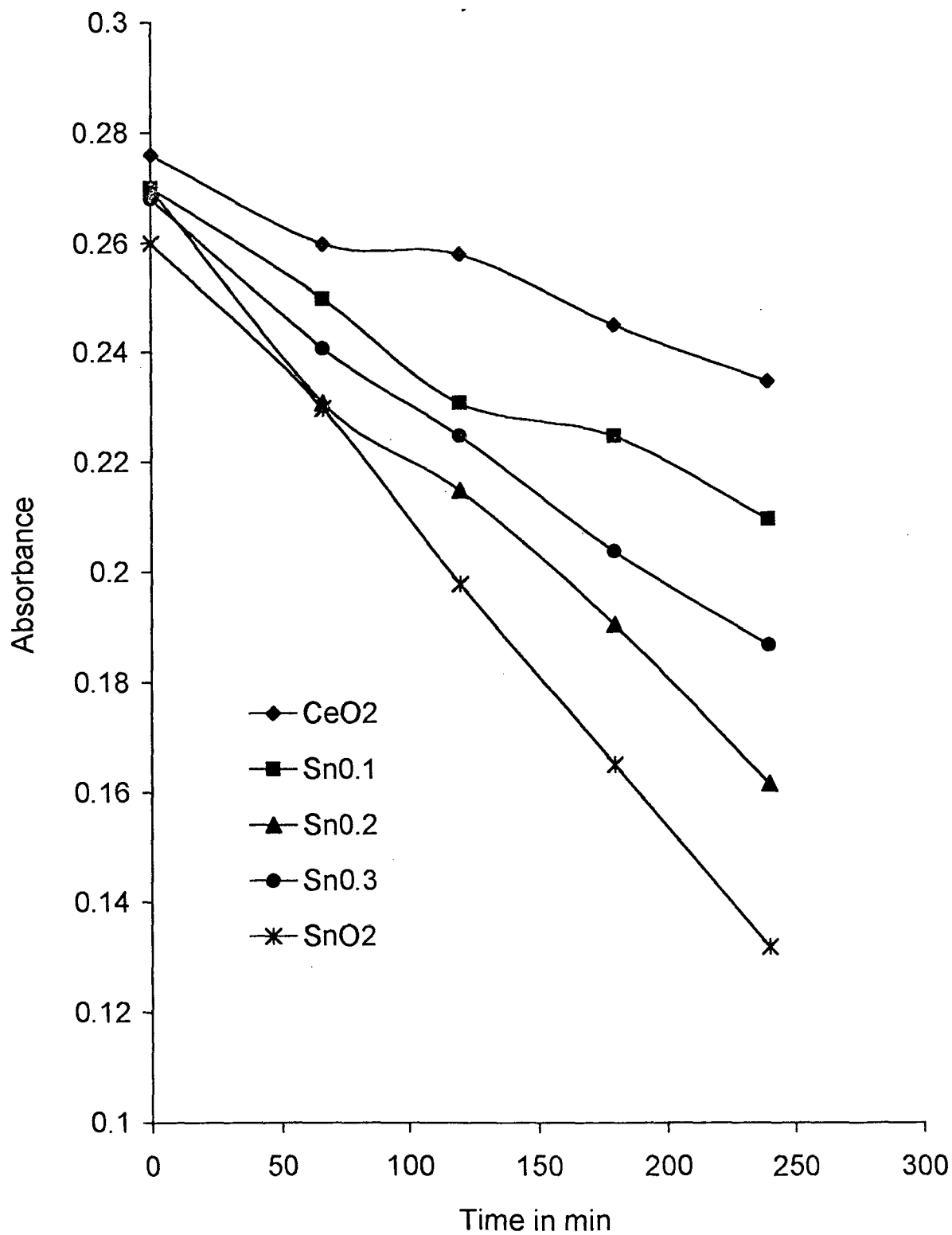


Fig. 5.7c) Degradation of NBB dye over $Ce_{1-x}Sn_xO_2$ at pH 4

becomes higher which helps in enhancing the photocatalytic activity. $\alpha\text{-Fe}_2\text{O}_3$ has higher activity than CeO_2 for the degradation of NBB dye. Photoactivity increases with Fe substitution due to increase in band gap. It is maximum for $\text{Ce}_{0.8}\text{Fe}_{0.2}\text{O}_2$ sample which is shown in fig 5.8. NBB dye is completely degraded with doped samples in sunlight. The higher photocatalytic activity is attributed to enhancement of redox couple of CeO_2 and change in band gap. Reaction was carried out at various pH conditions and alkaline pH show higher photocatalytic activity as shown in fig. 5.9. In alkaline medium, there is greater probability for the formation of hydroxyl radical ($\text{OH}\cdot$), which can act as an oxidant, thus increasing the rate of photodegradation of the dye.

5.5.3 Series III $\text{Ce}_{1-x}\text{Mn}_x\text{O}_2$:

Photocatalytic degradation of NBB dye over $\text{Ce}_{1-x}\text{Mn}_x\text{O}_2$ ($x = 0, 0.1, 0.2, 0.3$ and 1.0) samples was carried out under irradiation of sunlight. It was observed that MnO_2 shows very little activity for the degradation of NBB dye. Degradation rate increases with increase in exposure time. $\text{Ce}_{0.7}\text{Mn}_{0.3}\text{O}_2$ show maximum conversion rate. Mn doped samples show less activity as compared to other dopants which can be correlated with the increase in band gap energy. Larger band gap prevents the electron – hole recombination. Conversion rate for $\text{Ce}_{1-x}\text{Mn}_x\text{O}_2$ series is shown in fig. 5.10.

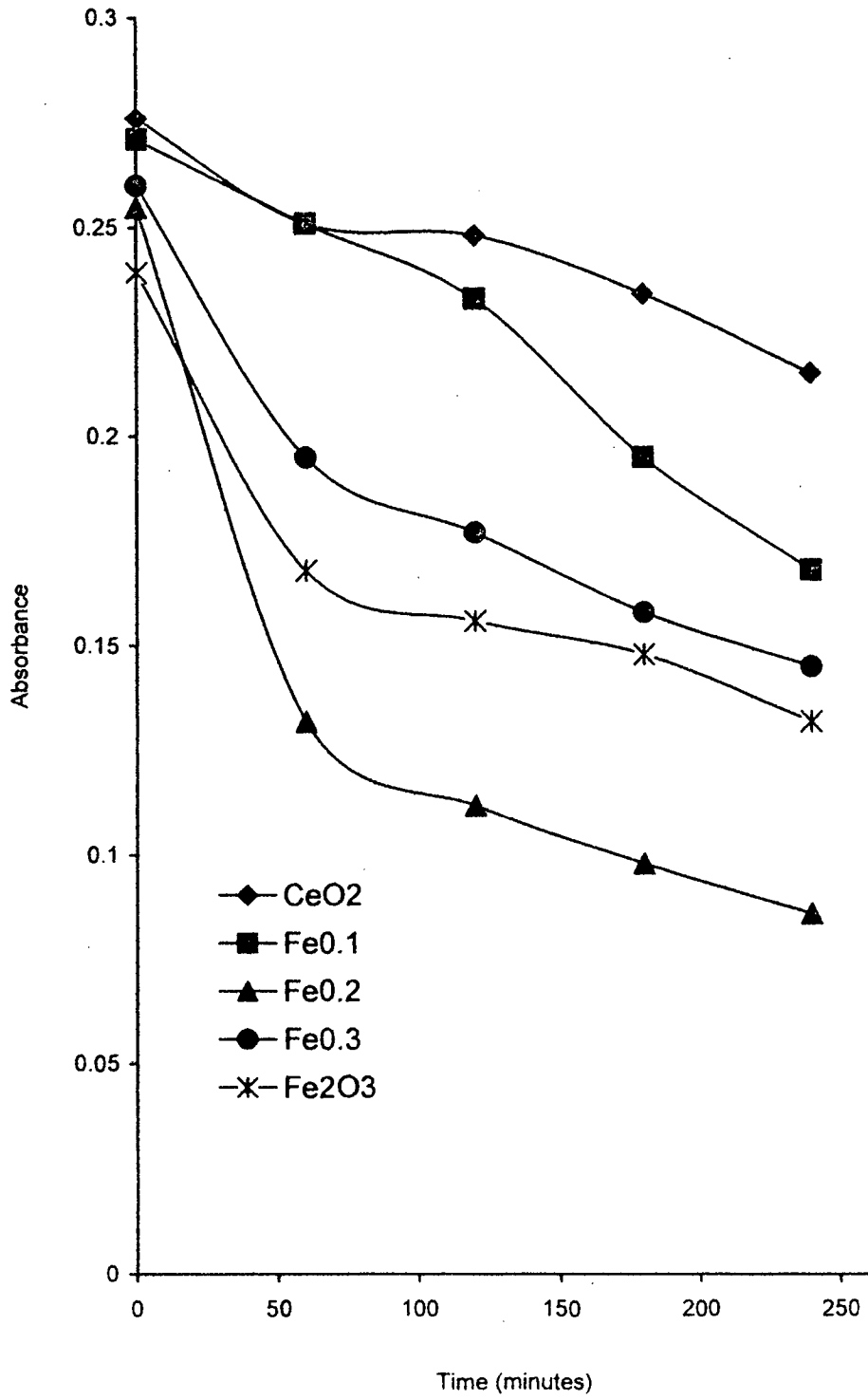


Fig. 5.8 Dgradation of NBB dye on $Ce_{1-x}Fe_xO_2$ with time at neutral pH

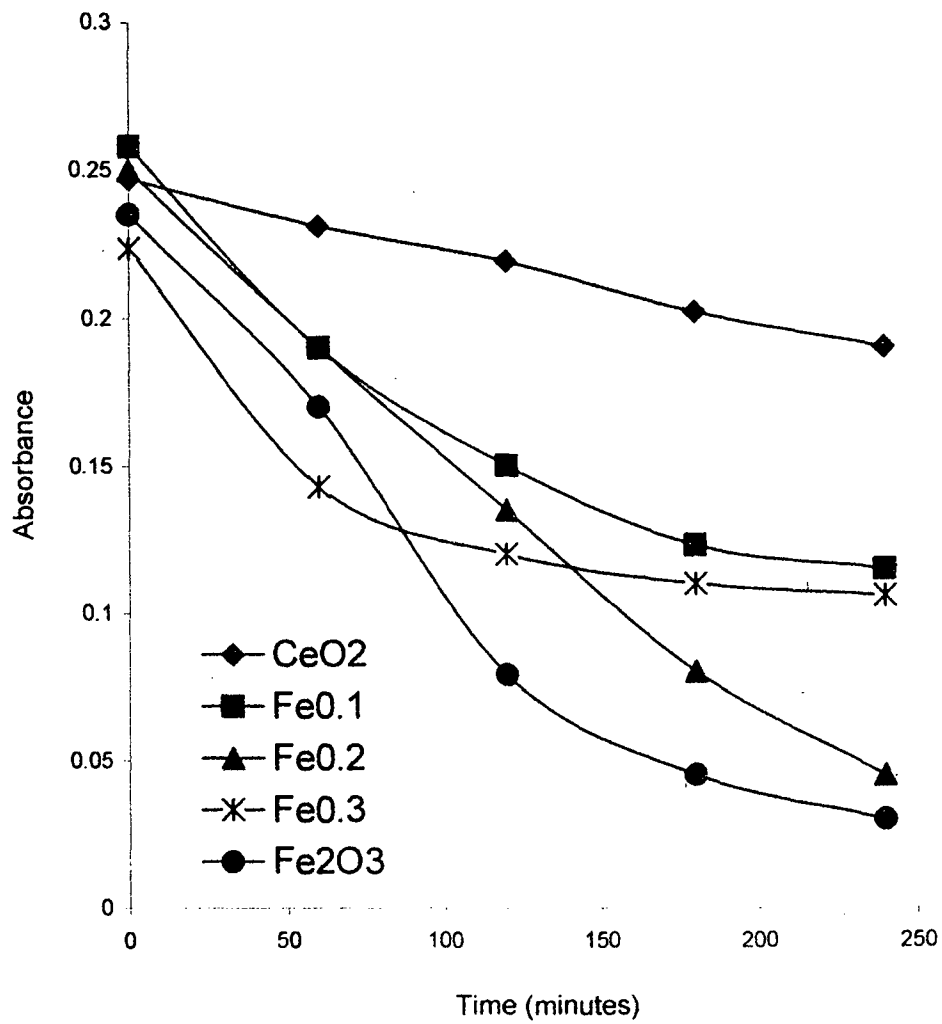


Fig.5.9 Degradation of NBB dye with time on $Ce_{1-x}Fe_xO_2$ at alkaline pH

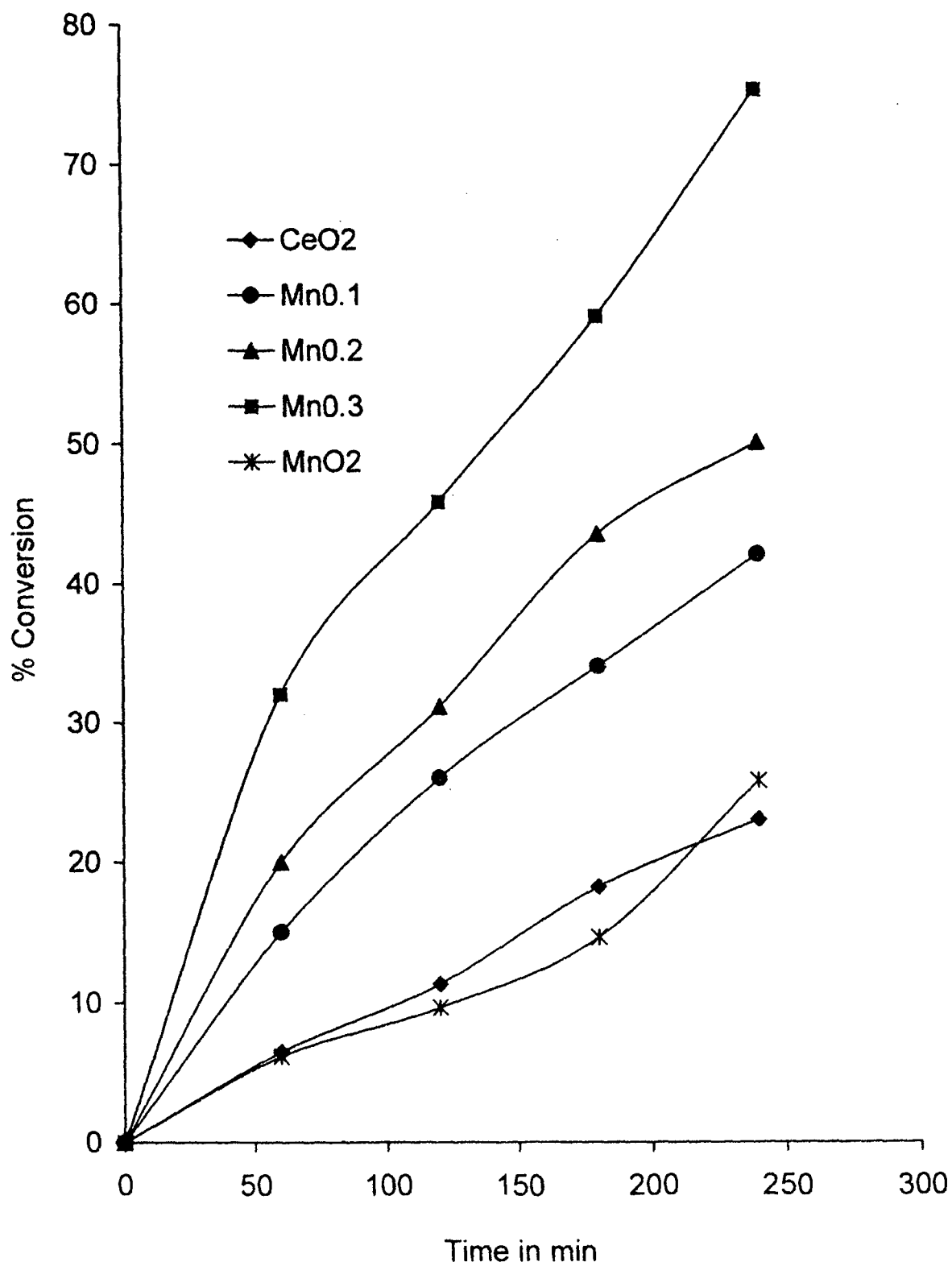


Fig. 5.10 % Conversion of NBB dye over $Ce_{1-x}Mn_xO_2$ at pH 7

5.5.4 Series IV; $\text{Sn}_{1-x}\text{Mn}_x\text{O}_2$

SnO_2 has been proved to be a good photocatalyst for the degradation of NBB dye using visible light which takes longer irradiation time. $\text{Sn}_{1-x}\text{Mn}_x\text{O}_2$ ($x = 0, 0.1, 0.2, 0.3$ and 1) samples show considerable photoactivity. Mn doped SnO_2 samples have large band gap which improves the photocatalytic activity for the degradation of NBB dye. Among all the samples $\text{Sn}_{0.7}\text{Mn}_{0.3}\text{O}_2$ show better activity. Photocatalytic degradation of dye is faster in alkaline medium as compared to neutral medium. Dye degrades completely with less time. Fig. 5.11 show degradation of NBB with time over $\text{Sn}_{1-x}\text{Mn}_x\text{O}_2$ samples.

It is not only the band gap responsible for photocatalytic activity, besides other factors such as surface morphology of the catalyst, active sites, valence states etc may be also responsible in photodegradation reaction.

5.5.5 Series V; MPc (M = Cu, Ni, Co, Fe)

Photodegradation of NBB was carried out on metal phthalocyanines under solar irradiation. Phthalocyanines are organic semiconductors and can be efficiently used as photosensitizers and photocatalysts. They show good photocatalytic activity for the degradation of NBB dye. Band gap energy of these phthalocyanines are shown in table 5.3. Iron phthalocyanine has large band gap than copper, cobalt and nickel phthalocyanine. Metal phthalocyanines

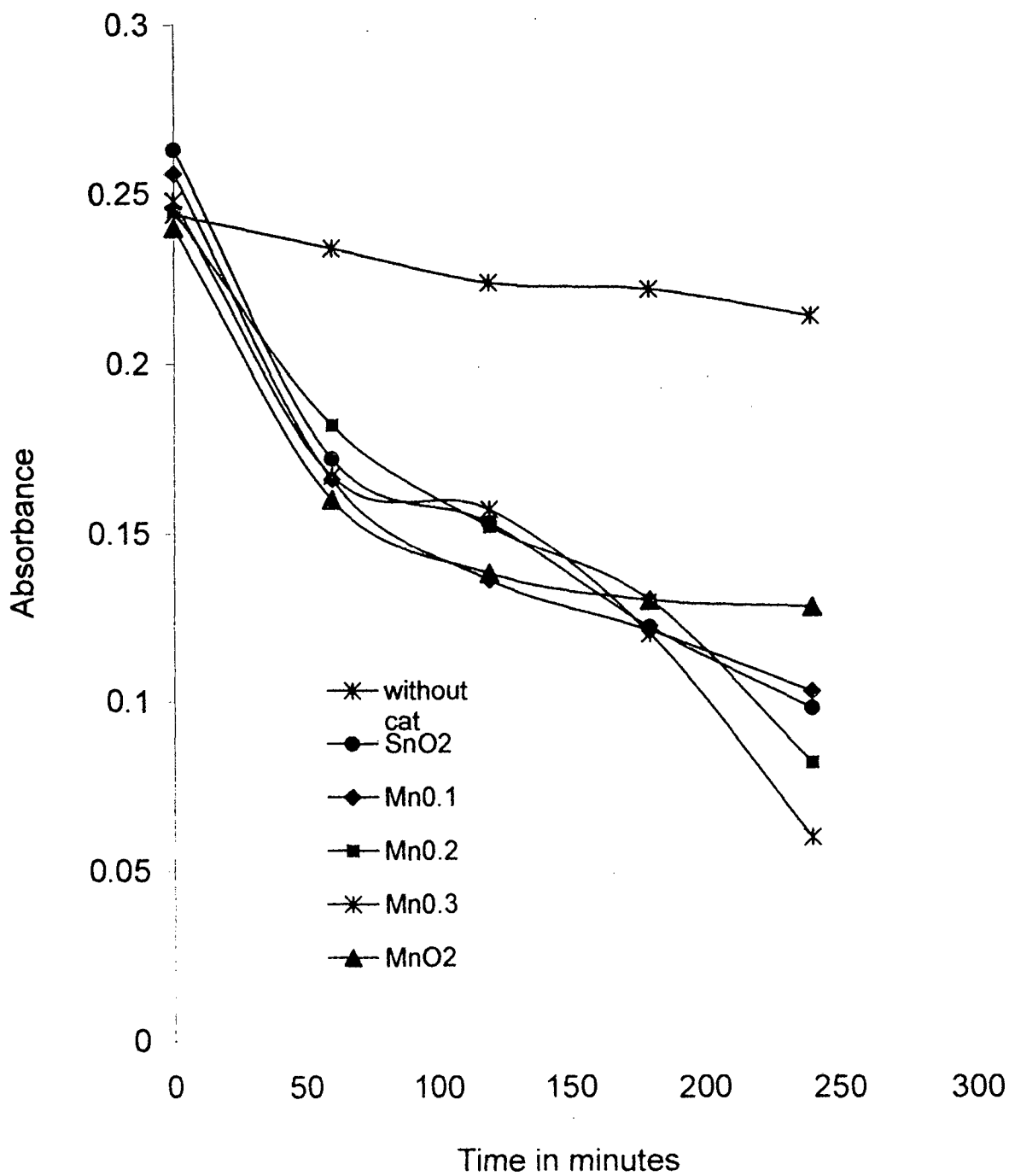


Fig. 5.11 Degradation of NBB dye over $\text{Sn}_{1-x}\text{Mn}_x\text{O}_2$ at neutral pH

degrades naphthol blue black dye when irradiated under solar light. CuPc show lowest conversion value. Absorption spectra obtained after completion of the NBB dye degradation indicate that the degradation products are colourless. Thus, the photocatalytic degradation provides an efficient way to mineralize this textile diazo dye. Fig 5.12 shows the % conversion of NBB dye with time on MPc.

5.6 comparative study of all the compositions

Comparison of photodegradation for different compositions was made. Fig.5.14 shows percentage conversion values for NBB dye degradation against composition (x) after 240 min photoirradiation for different series.

Among different compositions under investigation, $Ce_{1-x}Sn_xO_2$ series show highest photocatalytic activity for the degradation of NBB dye. Photoactivity increases with x and it is highest for $Ce_{0.8}Sn_{0.2}O_2$ and again decreases for $Ce_{0.7}Sn_{0.3}O_2$. After irradiation for 240 min under sunlight $Ce_{0.8}Sn_{0.2}O_2$ show almost 80% conversion at pH 7. $Ce_{1-x}Fe_xO_2$ also shows similar activity. In this series $Ce_{0.8}Fe_{0.2}O_2$ has same conversion value as that of $Ce_{0.8}Sn_{0.2}O_2$. This may be due to enhancement of $Ce^{3+} - Ce^{4+}$ redox couple and improvement of band gap energy.

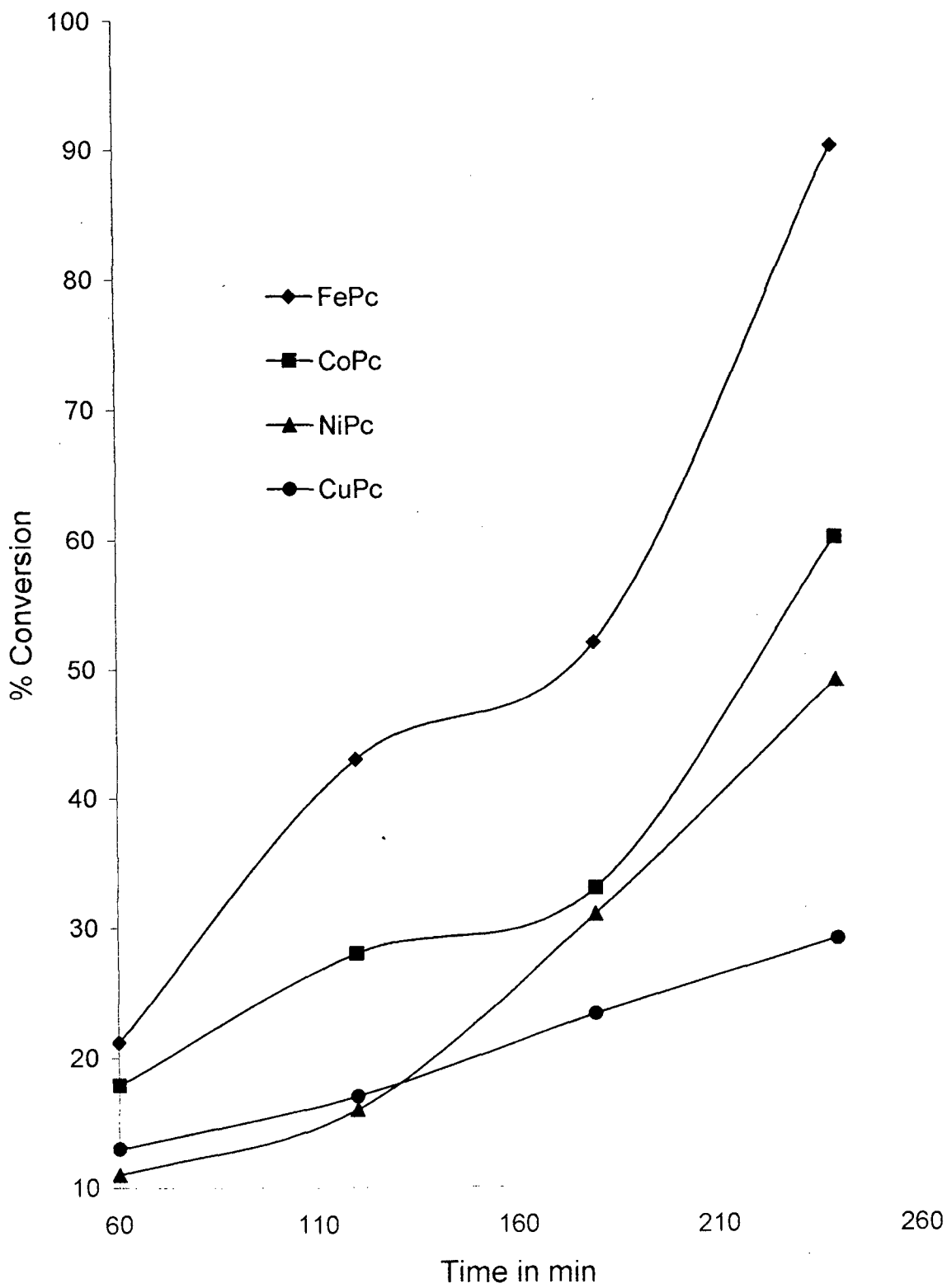


Fig. 5.12 Degradation of NBB dye on MPC

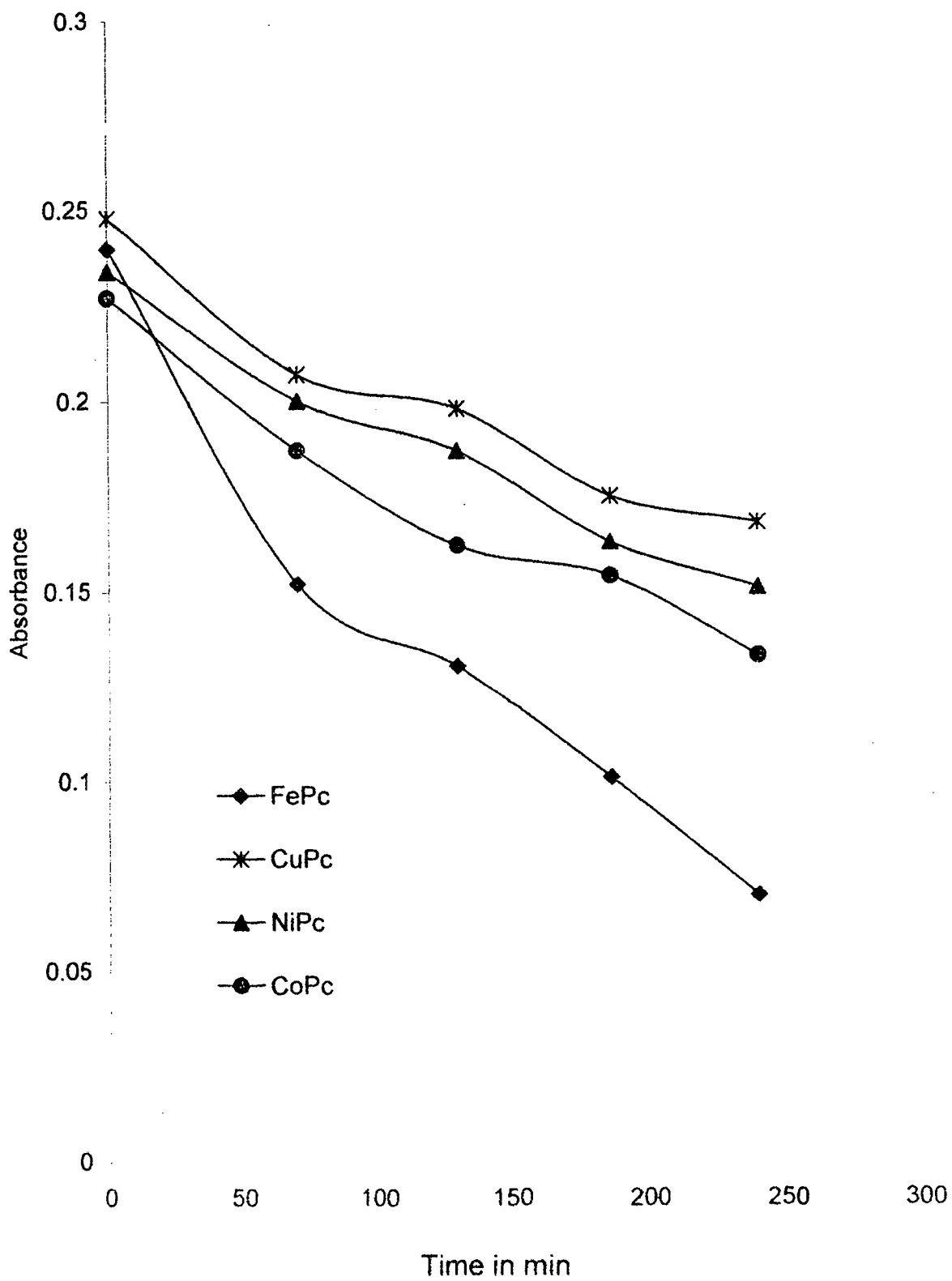


Fig. 5.13 Degradation of NBB over MPc at neutral pH

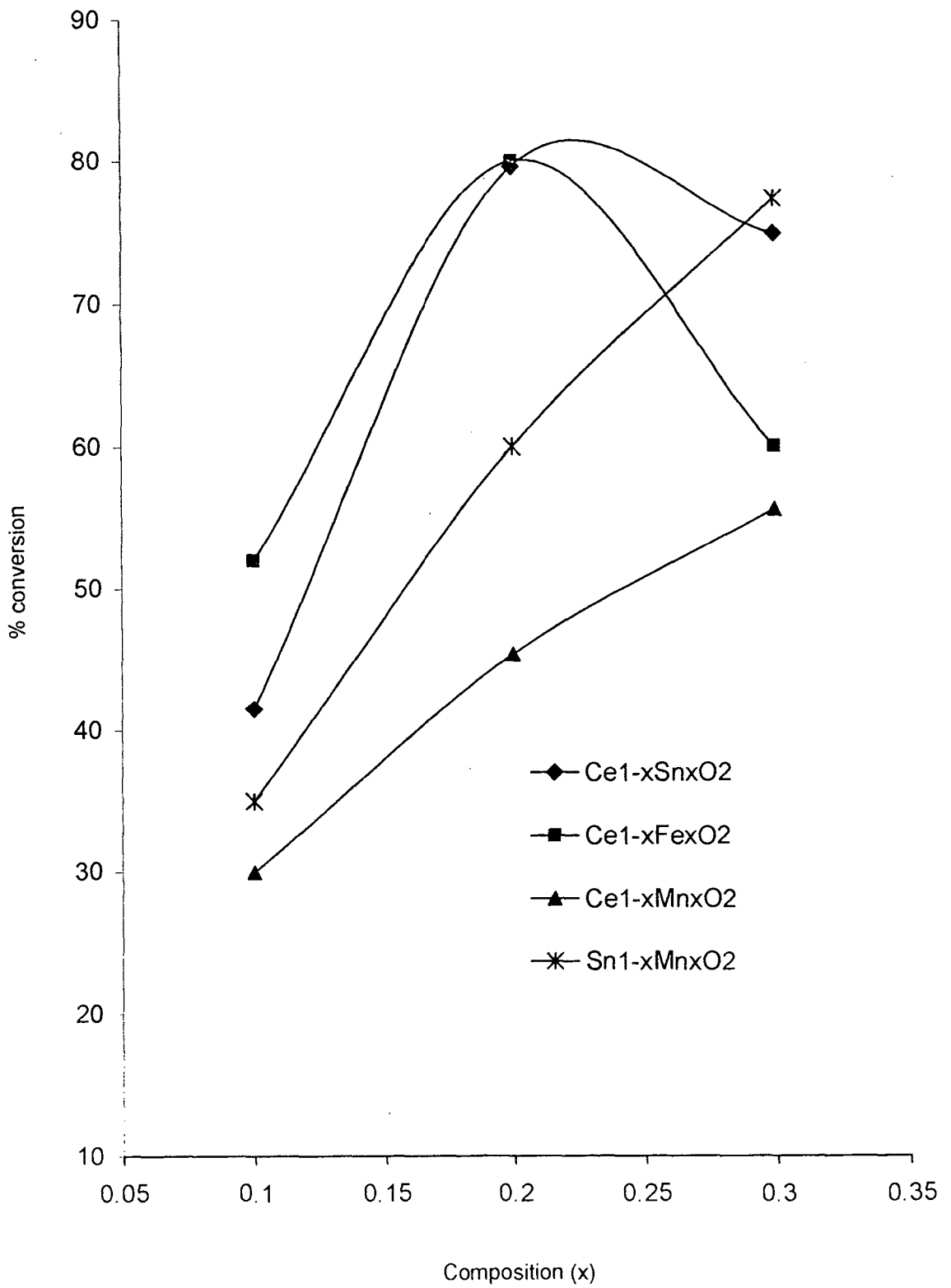


Fig. 5.14 % Conversion against composition (x) after 240 min irradiation

In this study, $Ce_{1-x}Mn_xO_2$ series show lowest activity for the degradation of NBB dye. The photocatalytic activity increases from $Ce_{0.9}Mn_{0.1}O_2$ to $Ce_{0.7}Mn_{0.3}O_2$. Also $Sn_{1-x}Mn_xO_2$ compositions show intermediate activity. It is higher than $Ce_{1-x}Mn_xO_2$ series but lower than $Ce_{1-x}Sn_xO_2$ and $Ce_{1-x}Fe_xO_2$ series. The photocatalytic activity increases from $Sn_{0.9}Mn_{0.1}O_2$ to $Sn_{0.7}Mn_{0.3}O_2$.

5.7 Analysis by HPLC method

The degradation products were analyzed by high performance liquid chromatography (HPLC) using Novapak C18 column. The mobile phase was composed of 70% methanol / 30% water at a flow rate of 1ml/min. In chromatogram A, before solar irradiation, sharp peak appeared with retention time equal to 2.711 min which is not observed in chromatograms B and C which are taken after 60 min and 240 min irradiation with solar light respectively. This indicates that chromatogram A is different from chromatograms B and C as shown in figure 5.15.

Small peaks in chromatogram B with the retention time 4.016 min and 4.669 min are not observed in chromatogram C but peak at retention time 4.669 min is observed in chromatogram A but of lesser intensity than B. Therefore chromatogram B is intermediate between A and C. The formation of

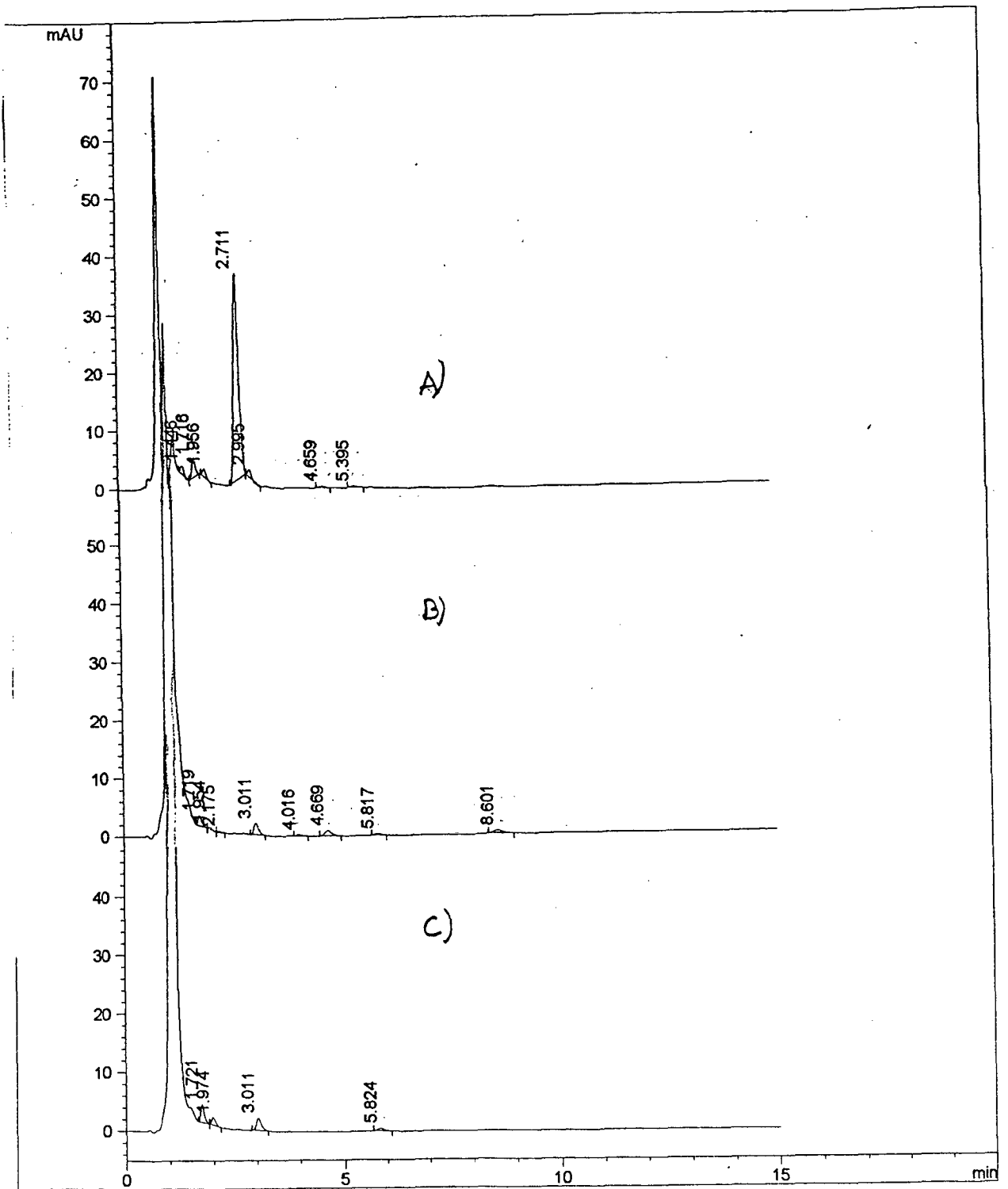
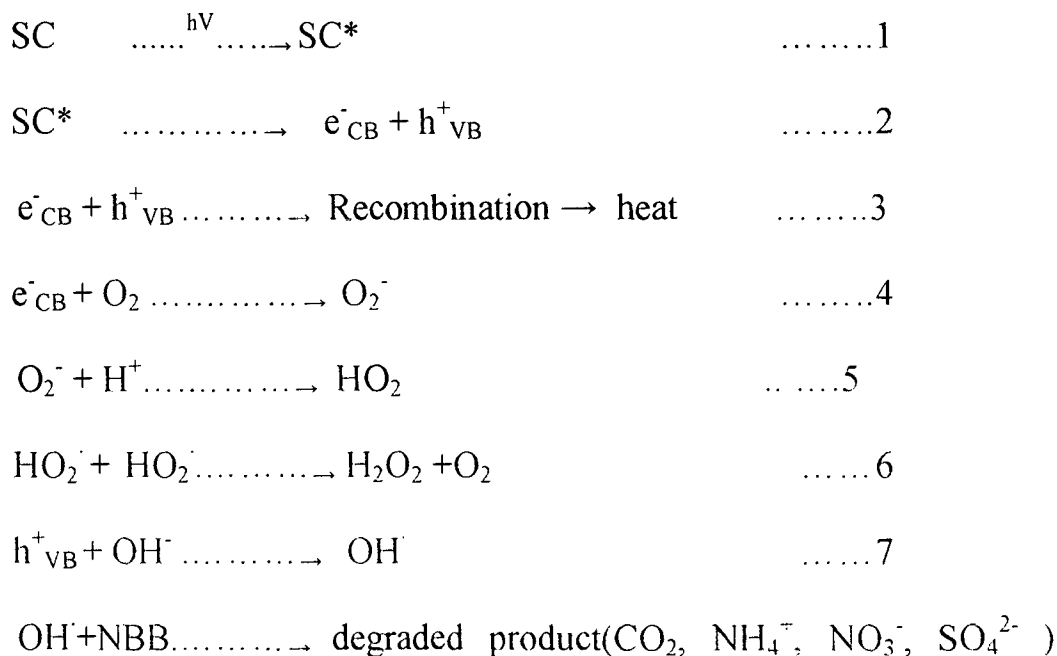


Fig 5.15 HPLC chromatograms of NBB dye degradation A) Before degradation B) Intermediate and C) After degradation

CO₂, SO₄²⁻, NO₃⁻ and NH₄⁺ was identified. This observation is similar to that reported earlier¹³⁸.

5.8 Mechanism

Many investigators have suggested various mechanisms for the degradation of dye pollutants^{121,155,156}. On exposure to solar radiation, the semiconductor (SC) will be excited to give SC*. This excited state will provide an electron (e⁻) in the conduction band leaving a hole in the valence band. This electron is then trapped by molecular O₂ forming O₂⁻ ions. The valence band hole generates hydroxyl radicals (OH[·]) from hydroxyl ions, which can easily attack the adsorbed dye, thus leading finally to their complete mineralization.



This observation is similar to that observed by^{14,4}.

5.9 Photocatalytic study of Auramine O dye

Photocatalytic degradation of Auramine O dye was carried out on selected samples. The stock solution was prepared by dissolving dye in distilled water. 100 ml of the 10^{-5} M dye solution was aerated by bubbling oxygen for 2-5 min. To this, 100 mg of the prepared photocatalyst was added which was found to be the optimum amount for the degradation of 100 ml dye solution. The reaction mixture was stirred and kept in the sunlight for irradiation. After every hour small quantity of the reaction mixture was taken out, filtered and absorbance was noted down. The λ_{max} of the dye solution was determined by scanning the dye solution in the visible region from 400 – 700 nm using UV-visible spectrophotometer. Auramine O dye absorbs at wavelength 432 nm. The pH of the solution was adjusted by addition of previously standardized HCl and NaOH solution. Fig 5.16 shows UV-visible spectrum of Auramine O dye.

The reaction was studied for various experimental conditions like optimization of catalyst amount, with O_2 and without O_2 , without using catalyst and with catalyst, only dye etc. The optimum amount of catalyst was found to be 100 mg for the degradation of 100 ml of 10^{-5} M Auramine O dye solution as shown in fig 5.17. It was found that dye is unable to degrade in dark. Also degradation is not possible without catalyst and without O_2 . Since oxygen is an electron scavenger it prevents electron – hole recombination.

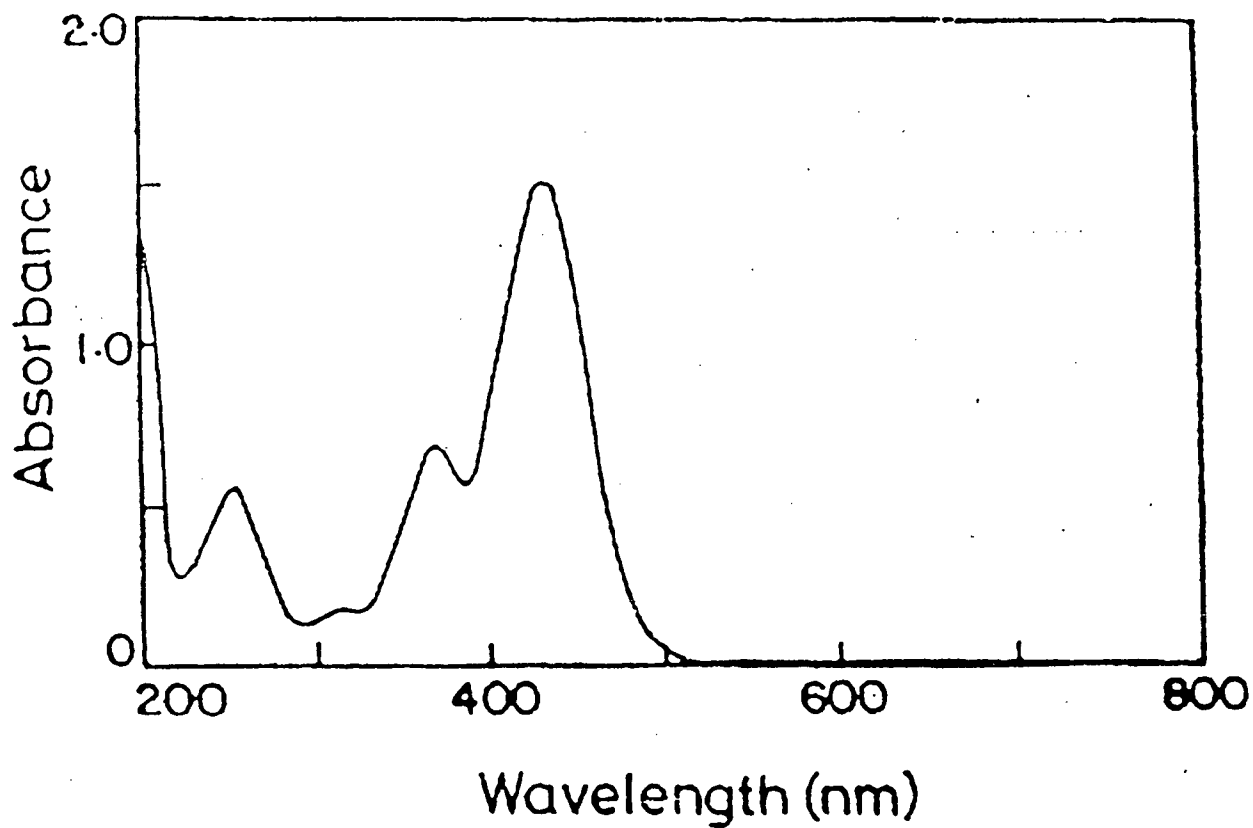


Fig 516—UV- Visible spectrum of Basic Yellow Auramine O

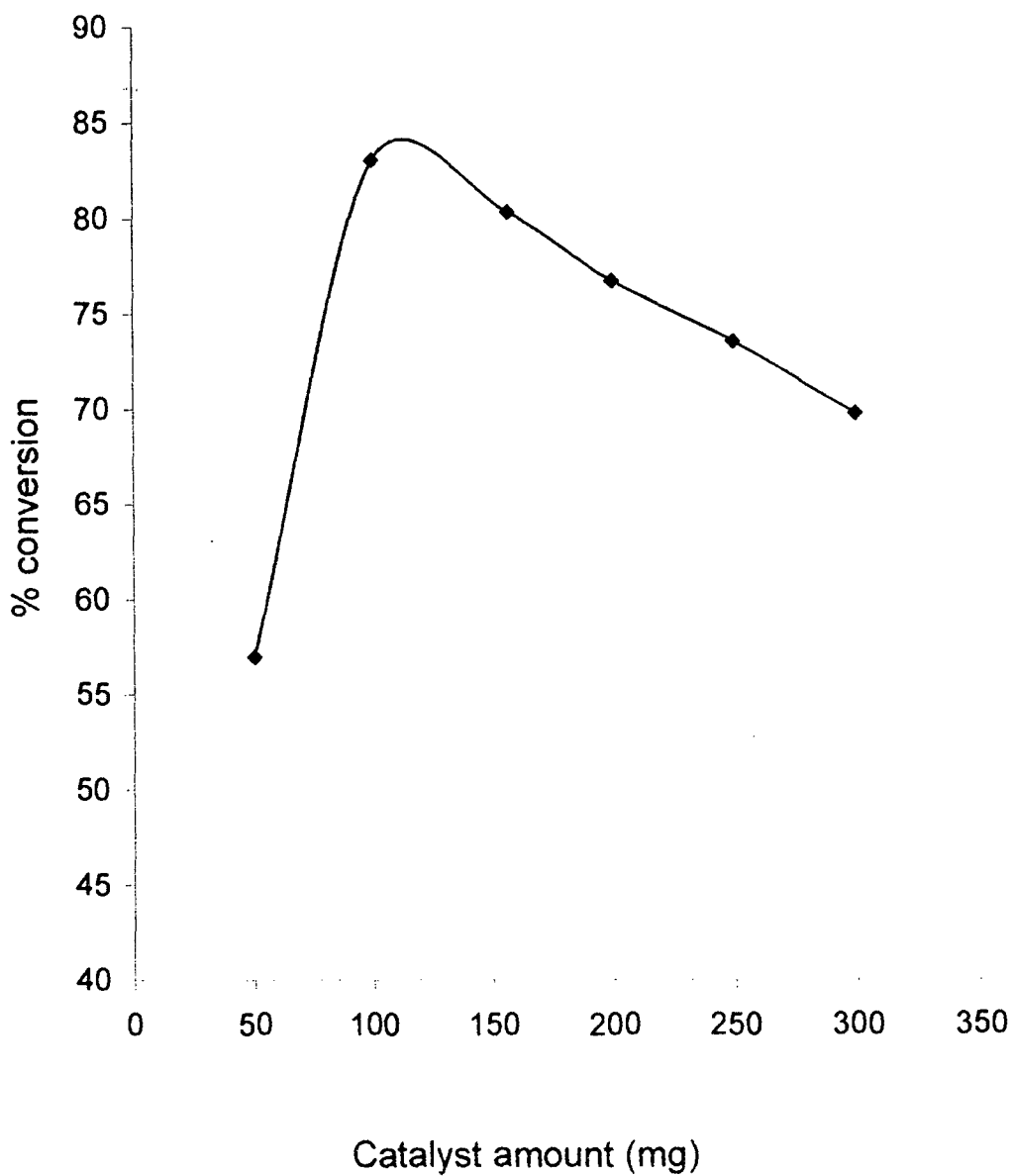


Fig. 5.17 Optimisation of catalyst amount for Auramine dye degradation

5.9.1 Series I ; $Ce_{1-x}Sn_xO_2$

$Ce_{1-x}Sn_xO_2$ samples were tested for the photocatalytic degradation of Auramine O dye. It was found that Sn doped samples efficiently degrades Auramine O dye when irradiated under sunlight. CeO_2 is not a good photocatalyst for the degradation of dye under solar light. It has low band gap energy which does not prevent electron – hole recombination. When it is doped with Sn, band gap is increased due to which doped samples show better activity for the degradation of Auramine O dye. As the x increase the band gap increases and it is higher for $Ce_{0.8}Sn_{0.2}O_2$ which shows highest activity. Fig. 5.18-5.19 shows degradation of Auramine O dye on $Ce_{1-x}Sn_xO_2$.

5.9. 2 Series V; MPc

Photocatalytic degradation of Auramine O dye was carried out on metal phthalocyanines. Among phthalocyanines Iron phthalocyanine show highest activity for the degradation of dye and copper phthalocyanine has lowest activity. This is because of variation in band gap energy. FePc has band gap of 5.67 eV whereas CuPc has band gap 2.87 eV. NiPC and CoPc shows intermediate photoactivity. Auramine O dye is decolourised within 5 hours time after irradiation in sunlight in presence of photocatalyst and oxygen. Fig. 5.20 shows conversion of Auramine O on MPc.

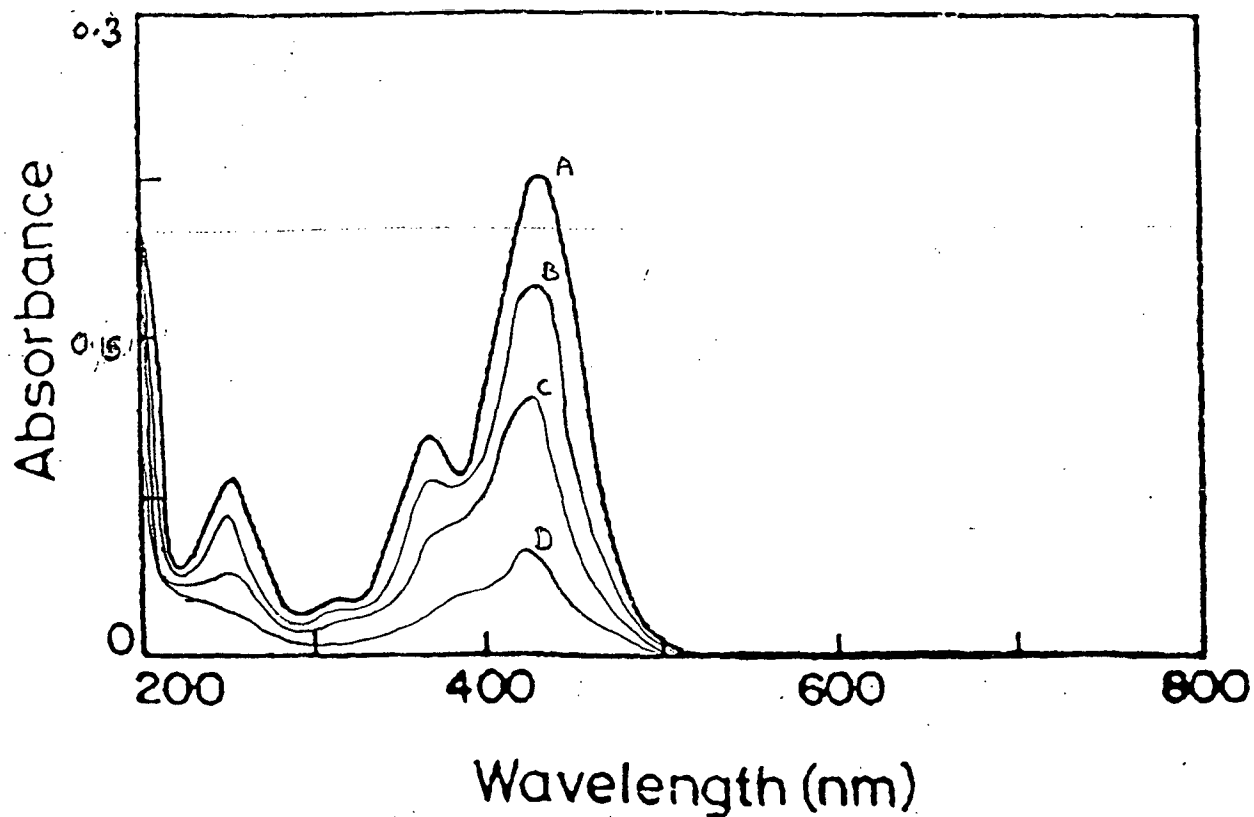


Fig 5.18 Auramine dye degradation over $Ce_{0.8}Sn_{0.2}O_2$ with time
A) 60 min B) 120 min C) 180 min and D) 360 min

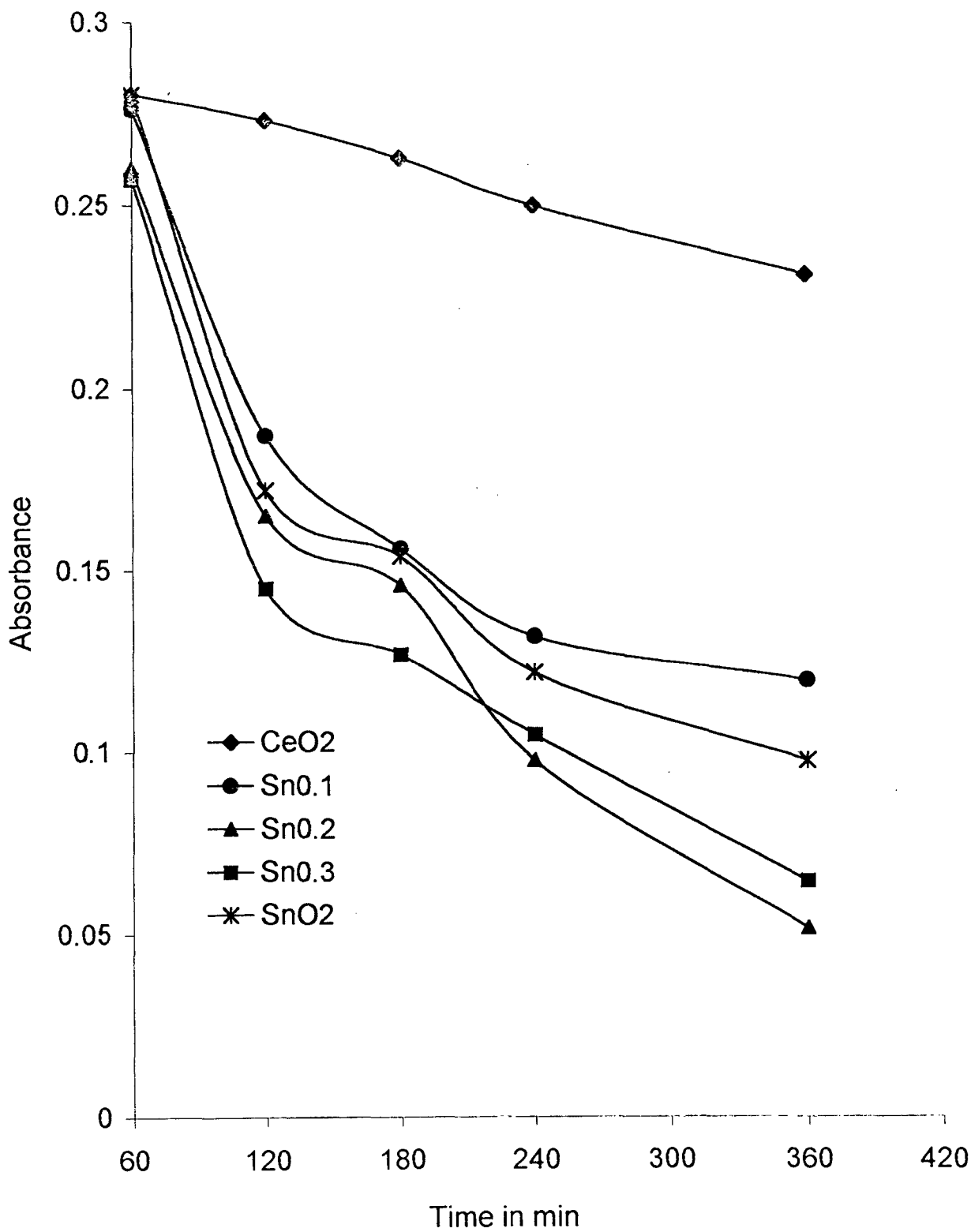


Fig. 5.19 Degradation of Auramine O dye over $Ce_{1-x}Sn_xO_2$ at neutral pH

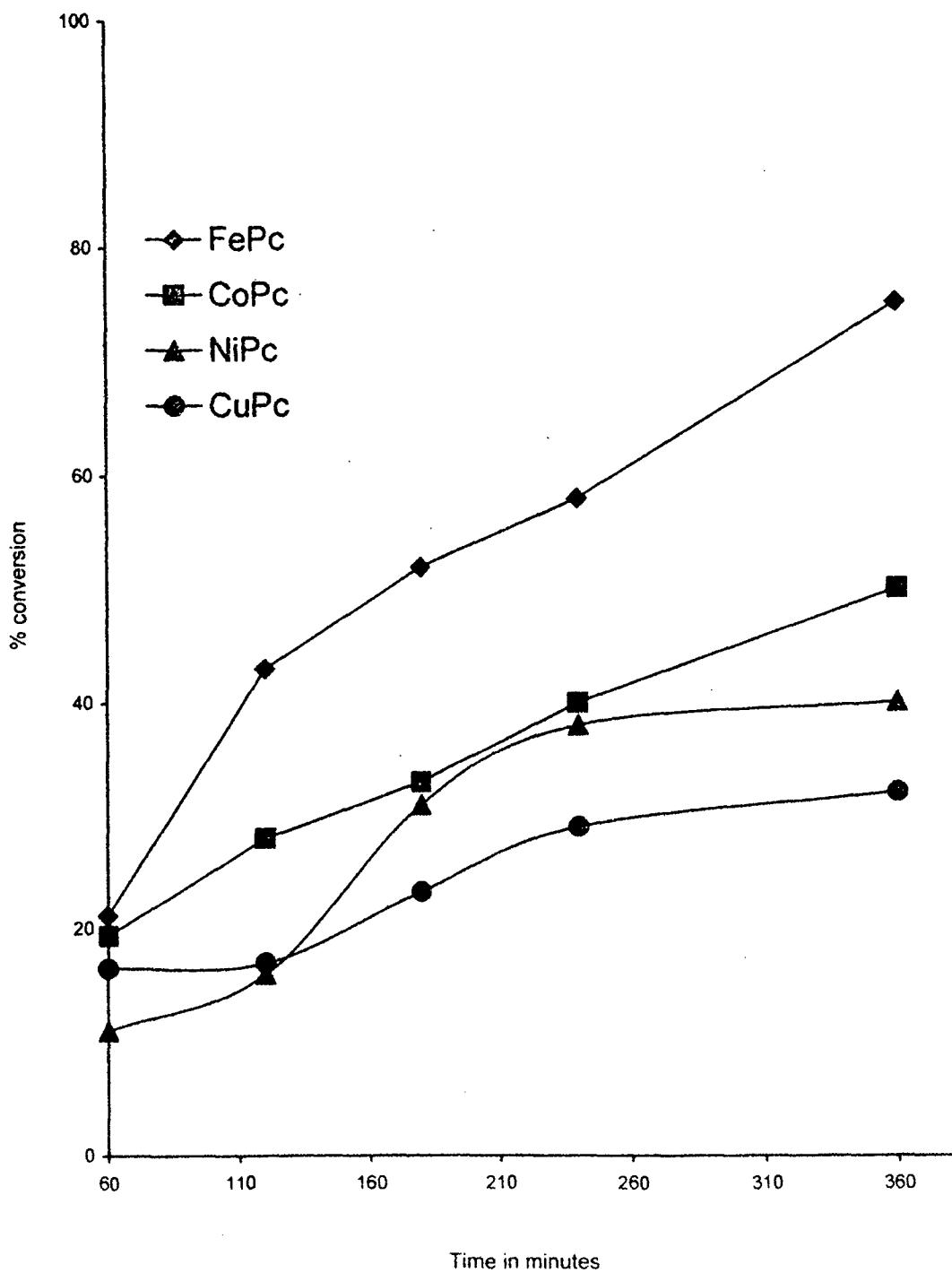


Fig.5.20 % conversion of Auramine dye with time on metal phthalocyanines at neutral pH

CHAPTER 6

CONCLUSION

CONCLUSION

Heterogeneous semiconductor photocatalysis is an advanced oxidation or degradation process to eliminate organic and dye pollutants in water. Photocatalytic reactions have received special attention in the decomposition of hazardous organic compounds because of their complete mineralization ability and possible application to pollution control using solar energy that is freely available almost throughout the year.

In the present investigation, studies were carried out on semiconductor oxides, mixed oxide solid solutions and phthalocyanines with an aim to correlate their solid state and photocatalytic properties with the substitution of different metals. The oxide samples investigated were prepared by co-precipitation method, which on sintering gave solid solutions.

X-ray studies confirmed that the prepared samples are monophasic and in well crystalline form. Ceria can form solid solution with other elements up to 30% mole maintaining cubic fluorite structure. CeO_2 is having cubic fluorite structure and SnO_2 is in tetragonal phase. All $\text{Ce}_{1-x}\text{Sn}_x\text{O}_2$ samples from $x = 0.1$ to 0.3 are having cubic structure with decrease in lattice parameter due to introduction of small size Sn atom into the CeO_2 crystal lattice. $\text{Ce}_{1-x}\text{Fe}_x\text{O}_2$ from $x = 0.1$ to 0.3 also show similar cubic fluorite structure with decrease in lattice parameter whereas Fe_2O_3 has α hexagonal structure. From $\text{Ce}_{0.9}\text{Mn}_{0.1}\text{O}_2$

to $\text{Ce}_{0.7}\text{Mn}_{0.3}\text{O}_2$ show cubic fluorite structure with increase in lattice parameter due to large ionic size of Mn atoms. Similarly $\text{Sn}_{1-x}\text{Mn}_x\text{O}_2$, from $x = 0.1$ to $x = 0.3$ show tetragonal structure. Phthalocyanines have stable β phase with square planar structures.

The FTIR is an important tool to see gradual changes taking place in the metal oxygen bonding on substitution of metal ion in the oxides. In the IR spectra of doped compounds evolution of new bands can be observed with metal substitution. The frequency of these bands has been related to the strength of metal – oxygen covalency.

In $\text{Ce}_{1-x}\text{Sn}_x\text{O}_2$ ($x = 0, 0.1, 0.2, 0.3$ and 1.0) samples, it is observed that with the substitution of Sn^{4+} in CeO_2 the absorption peak observed at 852cm^{-1} gets reduced. And there is appearance of peaks at 620 and 670cm^{-1} due to Sn-O vibrational modes. For $\text{Ce}_{1-x}\text{Fe}_x\text{O}_2$ samples, $x = 0.3$ show two sharp absorption peaks at 600 and 652cm^{-1} which are of Fe – O bond and peak at 852cm^{-1} gets reduced which is of Ce-O stretching vibrational mode. The $\alpha\text{-Fe}_2\text{O}_3$ shows intense bands.

In the IR spectra of $\text{Ce}_{1-x}\text{Mn}_x\text{O}_2$ series, it is observed that as x increases the Ce-O vibrational modes starts disappearing and there is evolution of Mn-O bands at 510 and 580cm^{-1} . These bands are of strong intensity in $\text{Ce}_{0.7}\text{Mn}_{0.3}\text{O}_2$ than MnO_2 . Similar observations were made regarding the IR

spectra of $\text{Sn}_{1-x}\text{Mn}_x\text{O}_2$ samples. IR spectra of phthalocyanine show absorption peaks around 1121-1123, 1090- 1092, 1067 - 1070, 947- 949, 872 - 885 and 754 cm^{-1} due to phthalocyanine skeletal vibration. In NiPc, FePc and CoPc complexes similar bands can be observed.

Thermal studies were carried out on the co-precipitated hydroxides to study their decomposition behaviour and revealed that overall decomposition pattern is similar with three distinct steps. The loss of moisture in the range of $100 - 150^\circ\text{C}$, followed by hydroxide decomposition between $150 - 350^\circ\text{C}$ and initiation of a solid state diffusion leading to solid solution between $400 - 700^\circ\text{C}$. The solid solution formation appears to take place over a large range of temperature after decomposition. Phthalocyanines do not have a sharp melting point they decompose at elevated temperature. Among all the phthalocyanines under study Cobalt phthalocyanine has higher stability.

Electrical resistivity measurement with temperature showed that the resistivity pattern of all the compositions decreases exhibiting the semiconductor behaviour. CeO_2 and SnO_2 are n-type semiconductors. On doping CeO_2 with Sn^{4+} electrical resistivity increases with x and it is maximum for $\text{Ce}_{0.8}\text{Sn}_{0.2}\text{O}_2$. Similarly on substituting Ce^{4+} with Fe^{3+} and Mn^{4+} electrical resistivity increases due to formation of oxygen vacancies. Phthalocyanines also show typical semiconductor behaviour.

Magnetic susceptibility studies showed that CeO_2 is paramagnetic and SnO_2 is diamagnetic. The intermediate compositions are paramagnetic and the susceptibility value decreases with the substitution of Sn. Also μ_{eff} values decreases with Sn substitution. Similarly for $\text{Ce}_{1-x}\text{Fe}_x\text{O}_2$, $\text{Ce}_{1-x}\text{Mn}_x\text{O}_2$ and $\text{Sn}_{1-x}\text{Mn}_x\text{O}_2$, the intermediate compositions are paramagnetic and the gram susceptibility value increases with x. Also μ_{eff} values found to increase with substitution of Fe and Mn metals. Among phthalocyanines, Cobalt phthalocyanine and copper phthalocyanine are paramagnetic and contains one unpaired electron. The μ_{eff} values are slightly lower than the expected values due to contribution of direct or super exchange intermolecular interactions. Nickel phthalocyanine is diamagnetic due to planar symmetry. The saturation magnetization values showed that Fe_2O_3 exhibit ferromagnetic behaviour.

ESR spectra recorded at room temperature showed broad line width for some of the recorded compositions. This may be due to the paramagnetic ions with a nuclear moment having a short lifetime of excited state because of larger size rare earth ions in the samples. ESR data are in agreement with the magnetic susceptibility data regarding the paramagnetic nature of the samples.

UV-Visible Diffuse Reflectance of the semiconductor photocatalysts was carried out to find out the band gap energies. These band gap energies were attempted to correlate with the photocatalytic activity in the

dye degradation process. Large band gap help in inhibiting electron – hole recombination.

A significant increase in the photocatalytic activity for the degradation of Naphthol Blue Black dye was observed by substitution of Sn^{4+} and Fe^{3+} in CeO_2 crystal lattice. This may be due to the enhancement of Ce^{4+} - Ce^{3+} redox couple and improvement of band gap energy. As the x increases in the series band gap is increased. However slight increase in the photocatalytic activity was observed for Mn substitution in CeO_2 lattice. SnO_2 is a good photocatalyst for the degradation of dye. Slight increase in the photocatalytic activity was observed for Mn substitution in SnO_2 crystal lattice. Also metal phthalocyanines show better photocatalytic activity. Among all the phthalocyanines, iron phthalocyanine has higher activity than others due to large band gap energy. The pH of the solution is an important factor in determining the photocatalytic activity.

It was found that textile diazo dye NBB can be degraded efficiently using semiconductor photocatalysts with solar light. The NBB dye degrades to a colourless solution after 240 min irradiation time. The formation of CO_2 , NH_4^+ , NO_3^- and SO_4^{2-} was evidence for the complete mineralization of the NBB dye. The mechanism involves formation of OH^\cdot radical which is an active

oxidizing agent for the degradation of NBB dye. O_2 prevents recombination of electron – hole pairs thus enhancing the reaction rate.

Also photocatalytic degradation of Auramine-O dye over selected samples showed good results. Metal phthalocyanines are good photocatalysts for the degradation of Auramine dye. Among all FePc show higher photoactivity than others due to large band gap energy which prevents electron hole recombination. For $Ce_{1-x}Sn_xO_2$ series, $Ce_{0.8}Sn_{0.2}O_2$ show better activity than other doped samples. CeO_2 show very little activity.

It is concluded that the photocatalytic degradation of hazardous chemical wastes and dye pollutants with semiconductor photocatalysts are economical, thermally stable and equally efficient but still the following strategies need to be considered for better performance:

1. Selection of the dopants that principally determine the photocatalytic activity.
2. Valency and vacancy control by the selection of dopants.
3. Enhancement of surface area by forming fine particles such as nano particles or dispersing on supports.
4. Improving favourable band gap either by using coupled semiconductors or by doping.
5. May be also by addition of precious metals with their appropriate regeneration to realize a high performance of the catalyst.

REFERENCES

1. R. Jain, N. Sharma, M. Bhargava, *J. Sci. Ind. Res.* **62** (2003) 1138
2. R. Jain, N. Sharma, M. Bhargava, *J. Sci. Ind. Res.* **62** (2003) 813
3. B. Neppolian, S. Sakthivel, B. Arabindoo, M. Palanichamy, V. Murugesan, in "Recent Trends in Catalysis" by V. Murugesan, B. Arabindoo, M. Palanichamy, Narosa Publishing House, New Delhi, 1999, pp. 78
4. M. Zhang, T. An, X. Hu, C. Wang, G. Sheng, J. Fu, *Appl. Catal. A Gen.* **260** (2004) 215
5. M. R. Hoffmann, S. T. Martin, W. Choi, D. W. Bahnemann, *Chem. Rev.* **95** (1995) 69
6. O. E. Kartal, M. Erol, H. Oguz, *Chem. Eng. Technol.* **24** (2001) 645
7. S. Sakthivel, S. U. Geissen, D. W. Bahnemann, V. Murugesan, A. Vogelpohl, *J. Photochem. Photobiol. A Chem.* **148** (2002) 283
8. M. Sokmen, D. W. Allen, A. T. Hewson, M. R. Clench, *J. Photochem. Photobiol. A Chem.* **141** (2001) 63
9. J. S. Hariprasad, T. Sivakumar, K. Shanthi, P. Kandasamy and P. S. Suresh in "Recent Trends in Catalysis" Narosa Publishing House, 1999 pp. 236
10. J. Cunningham, P. Sedlak, *Catal. Today* **29** (1996) 309
11. A. Assabane, Y. A. Ichou, H. Tahiri, C. Guillard, J. M. Harmann, *Appl. Catal. B Environ.* **24** (2000) 71

12. H. M. Coleman, B. R. Eggins, J. A. Byrne, F. L.M Palmer, E. King, *Appl. Catal.* **24** (2000) 11
13. L. Shi, C. Li, H. Gu, D. Fang, *Mater. Chem. Phys.* **62** (2000) 62
14. C. Galindo, P. Jacques, A. Kalt, *J. Photochem. Photobiol. A Chem.* **141** (2001) 47
15. A. Pandurangan, P. Kamala, S. Uma, M. Palanichamy, V. Murugesan, *Ind J. Chem. Technol.* **8** (2001) 496
16. M. Lundberg, B. Skarman, L. R. Wallenberg, *Micro. Meso. Mater.* **69** (2004) 187
17. J. M. Coronado, A. J. Maira, A. M. Arias, J. C. Conesa, J. Soria, *J. Photochem. Photobiol. A Chem.* **150** (2002) 213
18. A. L. Linsenbigler, G. Lu, J. T. Yates, *Chem. Rev.* **95** (1995) 735
19. B. G. Mishra, G. R. Rao, B. Poongodi, *Proc. Ind. Acad. Sci (Chem Sci)* **115** (2003) 561
20. M. D. H-Alonso, A. B. Hungria, A. M-Arias, M. F. Garcia, J. M. Coronado, J. C. Conesa, J. Soria, *Appl. Cat. B Environ.* **50** (2004) 167
21. R. Lin, Y. J. Zhong, M-F. Luo, W. P. Liu, *Ind. J Chem.* **40A** (2001) 36
22. G. R. Bamwenda, H. Arakawa *J. Mol. Catal. A Chem.* **161** (2000) 105
23. K. Vinodgopal, P. V. Kamat, *Sol. Energy Mater. Sol. Cell* **38** (1995) 401

24. W. Cun, Z. Jincai, W. Xinming, M. Bixian, S. Guoying, P. Ping'an, F. Jiamo, *Appl. Cat. B Environ.* **39** (2002) 269
25. D. D. Lee, D. S. Lee, *IEEE Sensor J.*, **1** (2001) 214
26. J. A. T. Antonio, R. G. Baez, P. J. Sebastian, A. Vazquez, *J. Solid State Chem.* **174** (2003) 241
27. V. Iliev, D. Tomova, L. Bilyarska, L. Prahov, L. Petrov, *J. Photochem. Photobiol. A Chem.* **159** (2003) 281
28. K. Pirkanniemi, M. Sillanpaa, A. Sorokin, *The Sci. of the Total Environ.* **307** (2003) 11
29. S. R. Kim, S. A. Choi, J. D. Kim, K. H. Choi, S. K. Park, Y. H. Change, *Synthetic Metals* **71** (1995) 2293
30. B. D. Berezin "Coordination Compounds of Porphyrins and Phthalocyanines" John Wiley and Sons, 1981
31. J. Metz, O. Schneider, M. Hanack, *Inorg. Chem.* **23** (1984) 1065
32. D. K. Macfarland, C. M. Hardin, M. J. Lowe, *J. Chem. Ed.* **77** (2000) 1484
33. K. Gurunathan, *Int. J. Hyd. Ener.* **29** (2004) 933
34. B. R. Bamwenda, T. Uesigi, Y. Abe, K. Sayama, H. Arakawa, *Appl. Catal. A Gen.* **205** (2001) 117
35. O. T. Sorensen "Non-stoichiometric Oxides" Academic Press , 1981

36. T. Ohashi, S. Yamazaki, T. Tokunaga, Y. Arita, T. Matsui, T. Harami, K. Kobayashi, *Solid State Ionics*. **113-115** (1998) 559
37. T. Zhang, P. Hing, H. Huang, J. Kilner, *J. Eurp. Ceram. Soc.* **21** (2001) 2221
38. Hj Matzke in "Non- stoichiometric Oxides" by O. T. Sorensen pp. 159 , 1981
39. S. Mihaiu, G. Postole, M. Carata, M. Culdaru, D. Crisan, N. Dragan, M. Zaharescu, *J. Eur. Cer. Soc.* **24** (2004) 963
40. M.M. B-Mohagheghi, M. S. Saremi, *Thin Solid Films* **441** (2003) 238
41. Mercy Iype, Ph. D. Thesis, Thiruvulla University, 2003
42. F. H. Moser, A. L. Thomas, *J. Chem. Ed.* **41** (1964) 245
43. P. Kofstad "Nonstoichiometry, Diffusion and Electrical Conductivity in Binary Metal Oxides" Norway 1972
44. G. Ranga Rao, H. R. Sahu, *Proc. Ind. Acad. Sci (Chem. Sci)* **113** (2001) 651
45. C. M. Freeman, C. R. A. Catlow, *J. Solid State Chem.* **85** (1990) 65
46. A. V. Salker, D. K. Chakrabarty, H. V. Keer, *Ind. J. Chem., A* **28** (1989) 458
47. B. Zhu, C. Xia, X. Luo, G. Niklasson, *Thin Solid Films* **385** (2001) 209
48. C. R. A. Catlow " Non-stoichiometric Oxides" edited by O. T. Sorensen , 1981
49. M. Kamruddin, P. K. Ajitkumar, R. Nithya, A. K. Tyagi, B. Raj, *Scripta Mater.* **50** (2004) 417
50. N. Audebrand, N. Guillov, J. P. Auffredic, D. Louer, *Thermochimica Acta* **286** (1996) 83

51. A. Turkovie, P. Dubeek, Z. C. Orel, S. Bernstorff, *Nanostr. Mater.* **11** (1999) 909
52. W. Huang, P. Shuk, M. Greenblatt, *Solid State Ionics* **113-115** (1998) 305
53. G. Ranga Rao, H. R. Sahu 15th Ind. National Symp. On Catal. & IPCAT 2 (2001) Vol. II
54. V. S. Escribano, E. F. Lopez, M. Panizza, C. Resini, J. M. G. Amores, G. Busca, *Solid State Sci.* **5** (2003) 1369
55. M. Ozawa, C. K. Loong, *Catal. Today* **50** (1999) 329
56. T. S. Zhang, J. Ma, L. B. Kong, Z. Zeng, P. Hing, J. A. Kilner, *Mater. Sci. Eng. B* **103** (2003) 177
57. Z. Tianshu, P. Hing, H. Huang, J. Kilner, *Mater. Sci. Eng. B* **83** (2001) 235
58. W. Huang, P. Shuk, M. Greenblatt, *Solid State Ionics* **100** (1997) 23
59. M. F. Wilkes, P. Hayden, A. K. Bhattacharya, *J. Catal.* **219** (2003) 305
60. S. Dikmen, P. Shuk, M. Greenblatt, *Solid Stat. Ionic.* **112** (1998) 299
61. R. S. de Biasi, M. L. N. Grillo, *J. Phys. Chem. Solid.* **64** (2003) 1365
62. G. S. Hermann, *Surface Sci.* **437** (1999) 207
63. Y. Kamimura, S. Sato, R. Takahashi, T. Sodesawa, T. Akashi, *Appl. Catal. A*, **252** (2003) 399
64. J-S. Lee, S-C Choi, *Mater. Lett.* **58** (2004) 390
65. Y. Nagai, T. Nonaka, A. Suda, M. Sugiura, *R & D Rev. Toyota CDRL* **37**

66. J. Kaspar, P. Fornasiero, M. Graziani, *Catal. Today* **50** (1999) 285
67. A. Martorana, G. Deganello, A. Longo, A. Prestianni, L. Liotta, A. Macaluso, G. Pantaleo, A. Balerna, S. Mobilio, *J. Solid State Chem.* **177** (2004) 1268
68. T. Akashi, S. Sato, R. Takahashi, T. Sodesawa, K. Inui, *Catal. Comm.* **4** (2003) 411
69. A. Khodadadi, S. S. Mohajezadeh, Y. Mortazavi, A. M. Miri, *Sens. Act. B* **80** (2001) 267
70. G. Fang, Z. Liu, C. Liu, K. L. Yao, *Sens. Act. B* **66** (2000) 46
71. R. Lin, M-F. Luo, Y. J. Zhong, Z-L. Yan, G-Y. Liu, W. P. Liu, *Appl. Catal. A Gen.* **255** (2003) 331
72. J. W. Jang, H. K. Kim, D. Y. Lee, *Mater. Lett.* **58** (2004) 1160
73. J. J. Zhu, J. M. Zhu, X-H Liao, J-L Fang, M. G. Zhou, H-Y Chen, *Mater. Lett.* **53** (2002) 12
74. S. Mishra, C. Ghanashyam, N. Ram, S. Singh, R. P. Bajpai, K. K. Bhasin, R. K. Bedi, *J. Sci. Ind. Res.* **62** (2003) 1063
75. N. Yamazoe, J. Fuchigami, M. Kishikawa, T. Seiyama, *Surf. Sci.* **86** (1979) 335
76. G. Korotcenkov, V. Macsanov, V. Brinzari, V. Tolstoy, J. Schwank, A. Cornet, J. Morante, *Thin Solid Films* (2004) 1

77. S. Davison, R. Kershaw, K. Dwight, A. Wold, J. Solid State Chem. **73** (1988) 47
78. R. Stola, G. Dyrda, W. Waclawek, Polyhedron **21** (2002) 677
79. S. Ambily, C. S. Menon, Mater. Lett. **36** (1998) 61
80. B. N. Achar, G. M. Fohlen, K. S. Lokesh, Poly. Deg. Stab. **80** (2003) 427
S. R. Kim et. al.
81. Synthetic Metals **71** (1995) 2299
82. K. R. V. Reddy, J. Keshavayya, J. Seetharamappa, Dyes and Pigments **59** (2003) 237
83. M. Wang, H. Z. Chen, J. L. Shen, S. L. Yang, J. Photochem. Photobiol. A Chem. **94** (1996) 249
84. N. Sehlotho, T. Nyokong, J. Mol. Cat. A Chem. **209** (2004) 51
85. J. G. Guan, W. Wang, R. Z. Gong, R. Z. Yuan, L-H Gan, K. C. Tam, Langmuir **18** (2002) 4198
86. C. Boscornea, St. Tomas, L. G. Hinescu, C. T-Mihaila, J. Mater. Process. Technol. **119** (2001) 344
87. Q. Wang, L. Wang, J. Yu, L. Yu, Advanced Mater. **12** (2000) 974
88. J. L. Boudelande, M. Karzazi, L. E. Dicoelio, M. I. Litter, G. M. Tura, E. San Roman, J. Photochem. Photobiol. A **108** (1997) 273
89. D. S. Lawrence, D. G. Whitten, J. Photochem. Photobiol. **64** (1996) 923

90. O. L. Kaliya, E. A. Lukyanets, G. N. Vorozhtsov J. Porp. Phthalo. **3** (1999) 592
91. S. Seelan, D. Srinivas, S. Sivasanker, 15th Ind. Nat. Symp. On Catal. & IPCAT-2 (2001) Vol. II P. 57.
92. S. L. Jain, B. Sain, V. K. Bhatia, 15th Ind. Nat. Symp. On Catal. & IPCAT-2 (2001) Vol. II
93. K. Kasuga, S. Takahashi, K. Tsukahara, T. Ohno, Inorg. Chem. **29** (1990) 354
94. H. L. Tuller, "Nonstoichiometric Oxides" by O. T. Sorenson Academic Press, (1981)
95. A. V. Salker, React. Kinet. Catal. Lett. **73** (2001) 209
96. J-H Lee, J. Kim, S-W. Kim, H-W. Lee, H-S. Song, Solid State Ionics **166** (2004) 45
97. V. B. Tare, Proc. Ind. Acad. Sci. (Chem. Sci.) **96** (1986) 549
98. a) T. Suzuki, I. Kosacki, H. U. Anderson, Solid State Ionics **151** (2002) 111
b) E. A. Morais, L. V. A. Scalvi, V. Geraldo, R. M. F. Scalvi, S. J. L. Ribero, C. V. Santilli, S. H. Pulcinelli, J. Eurp. Cer. Soc. **24** (2004) 1857
99. E. R. Leite, M. B. Bernardi, E. Longo, J. A. Varela, C. A. Paskocimas, Thin Solid Films **449** (2004) 67
100. J. Tan, L. Shen, X. Fu, W. Hou, X. Chen, Dyes and Pigments **61** (2004) 31

101. J. M. Hermann, F. Villain, L. G. Appel, *Appl. Catal. A Gen.* **240** (2003) 177
102. S. I. Shihub, R. D. Gould, *Thin Solid Films* **254** (1995) 187
103. K. D. Gould, A. K. Hassan, *Thin Solid Films* **223** (1993)
104. A. Vidadi, *Phys. Solid State* **11** (1969) 173
105. A. S. Riad, A. E. El-samahy, S. M. Khalil, *Physica B* **215** (1995) 217
106. Achar and Lokesh, *J. Solid State Chem.* **177** (2004) 1987
107. R. L. Dutta, A. Syamal, Ed. "Elements of Magnetochemistry" 2nd Ed. East-West press, 1993.
108. Z. Janczak, R. Kubiak, *Inorg. Chim. Acta* **342** (2003) 64
109. Y. Hinatsu, T. Fujino, *J. Solid State Chem.* **76** (1988) 124
110. R. El-Mallawany, A. H. El-Sayed, M. M. H. A. El-Gawad, *Mater. Chem. Phys.* **41** (1995) 87
111. K. R. V. Reddy, J. Keshavayya, *Dyes and Pigments* **53** (2002) 187
112. M. Szybowicz, T. Runka, M. Drozdowski, W. Bala, A. Grodzicki, P. Piszczek, A. Bratkowski, *J. Mol. Struct.* (2004)
113. B. M. Weckhuysan, R. A. Schoonhedt, *Catal. Today* **49** (1999) 441
114. N. Sergent, P. Gelin, L. P. Camby, H. Praliand, G. Thomas, *Sens. Act. B* **84** (2002) 176
115. T. Zhang, *Solar Energy Mater. Solar Cells* **73** (2002) 287

116. J. C. Kuriacose, "Advances in Catalysis Science & Technology" by T. S. R. Prasada Rao (1985) p.17.
117. <http://www.chem.boun.edu.tr/TiO2.html>.
118. Hisao Hidaka, Proc. Ind. Acad. Sci. (Chem. Sci.) **110** (1998) 215
119. M. V. Shankar, B. Neppolian, S. Sakthivel, B. Arabindoo, M. Palanichamy, V. Murugesan in "CATSYMP -15 and IPCAT-2 (2001) Vol. II p.114
120. S. Sakthivel, M. V. Shankar, M. Palanichamy, B. Arabindoo, V. Murugesan, J. Photochem. Photobiol. A. Chem **148** (2002) 153
121. A. Sharma, R. Sharma, S. S. Rathore, S. C. Ameta, J. Indian Chem. Soc. **79** (2002) 929
122. G. R. Rajarajeshwari, L. S. Roselin, B. Sivasankar, V. Sadasivam, K. Rengaraj, 15th Indian National Symp. On Catal. and IPCAT 2 (2001) Vol. II
123. L. S. Roselin, G. R. Rajarajeshwari, B. Sivasankar, V. Sadasivam, K. Rengraj, 15th Indian National Symp. On Catal. & IPCAT 2 (2001) Vol. II , p. 113
124. V. Pareek, A. A. Adesina, M. P. Brungs 15th Indian National Symp. On Catal. & IPCAT 2 (2001) Vol. II , p - 55.
125. S. N. Paleocrassas, Solar Energy **16** (1974) 45
126. H. Chun, W. Yizhong, T. Hongxiao, Appl. Catal. B **35** (2001) 95
127. M. A. Fox, Acc. Chem. Res. **16** (1983) 321

128. S. Yabe, M. Yamashita, S. Momose, K. Tahira, S. Yoshida, R. Li, S. Yin, T. Sato, *Inter. J. Inorg. Mater.* **3** (2001) 1003
129. M. Miyauchi, *Chem. Mater.* **14** (2002) 2812
130. F. R. Sensato, R. Custodio, E. Longo, A. Beltran, J. Andres, *Catal. Today* **85** (2003) 145
131. K. Ozoemena, N. Kuznetsova, T. Nyokong, *J. Photochem. Photobiol. A: Chem.* **139** (2001) 217
132. C. Nasr, K. Vinodgopal, L. Fisher, S. Hotchandani, A. K. Chattopadhyay, P. V. Kamat, *J. Phys. Chem.* **100** , 8436 (1996)
133. K. Vinodgopal, I. Bedja, P. V. Kamat, *Mater. Res. Bull.* **8** (1996) 2180
134. C. Nasr, K. Vinodgopal, Surat Hotchandani, A. K. Chattopadhyay, and P. V. Kamat, *Res. Chem. Inter.* **23** (1997) 219
135. C. Nasr, K. Vinodgopal, S. Hotchandani, A. K. Chattopadhyay, and P. V. Kamat. *Phys. Chem.* **49** (1996) 159
136. J. Luo, M. Hepel, *Electrochimica Acta* **46** (2001) 2913
137. M. Hepel, J. Luo, *Electrochimica Acta* **47** (2001) 729
138. C. Jiang, Y. Guo, C. Hu, C. Wang, D. Li, *Mater. Res. Bull.* **39** (2004) 251
139. D. Cordischi, N. Burriesci, F. D'Alba, M. Petrerà, G. Polizzotti, M. Schiavello, *J. Solid State Chem.* **56** (1985) 182

140. M. A. Hasnat, I. A. Siddiquey, I. S. M. Saiful, *Ind. J. of Chem.* **42A** (2003) 1865
141. J. Li, C. Chen, J. Zhao, H. Zhu, J. Orthman, *Appl. Catal. B Environ.* **37** (2002) 331
142. S. Sakthivel, B. Neppolian, B. Arabindoo, M. Palanichamy, V. Murugesan "Recent Trends in Catalysis" Narosa Publishing House, New Delhi, (1999), p. 778.
143. I. Spiewak, R. Benmair, R. Messalem, O. Radchenko, *Proc. Ind. Acad. Sci. (Chem. Sci.)* **110** (1998) 229
144. T. S. Srivastava, S. Shukla, *Proc. Ind. Acad. Sci. (Chem. Sci.)* **102** (1990) 329
145. R. Venkatesan, N. Periasamy, T. S. Srivastava, *Proc. Ind. Acad. Sci. (Chem. Sci.)* **104** (1992) 713
146. T. B. Nauyen, J. P. Deloume, V. Perrichon, *Appl. Catal.* **249** (2003) 273
147. Robinson, Klein, *J. Amer. Chem. Soc.* **74** (1952) 4716
148. *Bull. Mater. Sci.* **26** (2003) 41
149. C. N. R. Rao in "Chemical Applications of IR Spectroscopy" New York, 1963, pp. 597
150. A. Keshavaraja, *Thermans* -1993 , p. 283
151. P. Borker, A. V. Salker, *Thermans* 2004, pp. 329

152. D. C. Schmelling, K. A. Gray, P. V. Kamat, Environ. Sci. Technol. **30** (1996) 2547
153. A. Piscopo, D. Robert, J. V. Weber, Appl. Catal. B Environ. **35** (2001) 117
154. M. Muruganandham, M. Swaminathan, Sol. Ener. Mater. Sol. Cells, **81** (2004) 439
155. U. Stafford, K. A. Gray, P. V. Kamat, Heter. Chem. Rev. **3** (1996) 77
156. R. K. Khandewal, V. K. Vaidya, J. Ind. Chem. Soc. **79** (2002) 185



Appendix- I

Publications

1. Thermogravimetric analysis of Cobalt phthalocyanine

Pritam Borker and A. V. Salker

Thermans 2004 – M. S. University, Baroda, 329

2. Solid state and photocatalytic studies of $Ce_{1-x}Fe_xO_2$

Pritam Borker and A. V. Salker

Indian Journal of Chemistry A (communicated)

3. Synthesis, Characterization and photocatalytic studies of $Ce_{1-x}Sn_xO_2$

Pritam Borker and A. V. Salker

Environmental Science and Technology (communicated)

4. Synthesis, Characterization and photocatalytic studies of metal phthalocyanines

Pritam Borker and A. V. Salker

Indian Journal of Chemical Technology (communicated)